Polarization Effects in a Recirculating Loop System and Emulation of a Straight-line System Using a Recirculating Loop

by
Yu Sun

Dissertation submitted to the Faculty of the Graduate School
of the University of Maryland in partial fulfillment
of the requirements for the degree of
Doctor of Philosophy
2003

APPROVAL SHEET

Title of Thesis: Polarization effects in a recirculating loop system and emulation of a straight-line system using a recirculating loop

Name of Candidate: Yu Sun
Doctor of Philosophy, 2003

Dissertation and Abstract Approved: _____

Professor Gary M. Carter
Department of Computer Science and Electrical Engineering

Date Approved: _____

ABSTRACT

Polarization Effects in a Recirculating Loop System and Emulation of a Straight-line System Using a Recirculating Loop

Yu Sun, Doctor of Philosophy, 2003

Dissertation directed by: Gary M. Carter, Professor
Department of Computer Science and Electrical Engineering

Recirculating loops have proven to be an inexpensive and effective test bed in transmission studies. However, without appropriate controls, recirculating loops cannot accurately emulate polarization effects, such as polarization dependent loss/gain (PDL/PDG) and polarization mode dispersion (PMD), in straight-line systems. In this dissertation, I systematically investigated the polarization evolution and the system performance of a single channel dispersion-managed recirculating loop. I showed that due to the periodic optical path, the system performance in such a loop system was different from that of a straight-line system. I also adapted the reduced Stokes model to simulate the polarization behavior and the system performance. The excellent agreement of the experimental results and the numerical simulations provided the first experimental validation of the reduced Stokes model. In addition, I derived a *Q*-factor formula to take into account the effect of partially polarized noise and an analytical probability density function of the *Q*-factor distribution. I validated the *Q*-factor formula and the probability density function of the *Q*-factor distribution by the excellent comparison of the experimental results, the numerical simulations, and the analytical results. I showed that partially polarized noise

could cause large system variation. Finally, I overcame the limitation of the recirculating loop system by developing a loop-synchronous scrambling technique to break up the periodicity of the loop system. The system performance of a scrambled loop system closely resembles that of a straight-line system. Besides the loop-synchronous scrambling technique, I also addressed several other critical issues in loop experiments. I investigated the system performance of a scrambled loop system by measuring the *Q*-factor distribution with different PDL levels in the system, with and without the input scrambler. I showed that by carefully choosing the input-scrambling rate, one can improve the system performance and reduce the variation and the *Q*-factor distribution is asymmetric with a significant PDL in the system.

Dedication

To my parents, husband and daughter

Acknowledgement

On a personal note, I wish to extend my deepest gratitude to my advisor, Professor Gary M. Carter for giving me the opportunity to carry out this state-of-the art project and for his consistent trust, support and encouragement. I also want to express my heartfelt appreciation to Professor Curtis R. Menyuk for his generous help and support. I am also indebted to all my committee members, Professor Gary M. Carter, Professor Curtis R. Menyuk, Professor Li Yan, Professor Fow-Sen Choa, Professor Terrance L. Worchesky, and Dr. Shuxian Song, for their comments and advice, as well as in sharing the vast wisdom in technical writings. I want to thank all my colleagues in the Optical Fiber Communications Laboratory in UMBC for their supports and collaborations.

Contents

List of Figures

Chapter 1

Introduction

In order to increase the capacity of optical communication systems, scientists and engineers are constantly seeking new approaches to put more channels in systems and to increase the data rate, as well as to extend the propagation distance. To directly evaluate the system performance from straight-line transmission experiments or field tests is extremely expensive, especially for long-haul systems consisting thousands of kilometers of fiber. Even in metro systems, which are less than a couple of hundred kilometers in length, field tests are limited by the already installed fiber and the inability to change the components. An inexpensive and flexible experimental model is very important in studying optical communication systems. Optical recirculating loops have proven to be efficient tools for experimental simulations of long distance communication systems at greatly reduced cost and with significant flexibility [1] – [3].

Since the early nineties, recirculating loop systems have been widely used in the study of long-haul time division multiplexing (TDM) systems [1] and [2], the WDM net-

work systems [3], [4] and [5], as well as applications of newly developed system components [6] and [7]. In fact, transmission distances have been achieved in loops that are unimaginable in any other transmission medium. However, the difference between a recirculating loop system and a realistic straight-line system is not well studied until recently. With the increase of the data rate in telecommunication systems, the polarization effects, such as the polarization dependent loss (PDL), the polarization dependent gain (PDG) and the polarization mode dispersion (PMD) have drawn increasing attention. Studies have shown that these polarization effects impair the system performance. The combined PDL and PDG effects cause the variation of the system performance [8] – [11] and in general with propagation, PMD distorts the pulse, increasing the BER [12].

It is known that recirculating loop systems are sensitive to the polarization states of the light in the system, so that for many systems, polarization controllers are used to achieve increased transmission distance [13], [14] and [15]. Studies of these polarization effects performed in recirculating loop systems have shown that without appropriate controls, the recirculating loop systems can not correctly emulate the polarization effects of straight-line systems [16] and [17]. Therefore it is important to understand the polarization behaviors in recirculating loop systems and to overcome the limitation of recirculating loops in order to accurately emulate the system performance of a realistic system.

Simulating the polarization effects in the system is as challenging as studying them experimentally. It is common to study fiber system impairment using the coupled nonlinear Schrödinger equation that has been modified to include loss, amplification, spontaneous emission noise and other effects [18] – [20]. However, solving this equation is computationally time consuming, especially in a WDM system involving large number of

channels. Furthermore, since the polarization effects are random in nature, one must simulate multiple fiber realizations, so that it is not realistic to study the impairments introduced by polarization effects using complete numerical simulations. An effective reduced model that separates the impairments due to polarization effects from other effects, such as dispersion and nonlinearity is needed. Dr. Ding Wang and Dr. Curtis Menyuk [21], [22] have introduced a reduced Stokes model that follows the Stokes parameters of the signal and the noise, rather than simulating the detailed time domain evolution of individual pulses. This model separates the polarization effects from the effects of dispersion and nonlinearity based on the consideration that the polarization effects evolve a much slower time scale than the other effects. In Chapter 2, I review the reduced Stokes model and discuss the application of this model to a loop system.

An accurate receiver model is as important as the transmission model in the comparison of system performance. The system performance is often evaluated by the *Q*-factor, which is defined as $Q = (I_1 - I_0)/(\sigma_1 + \sigma_0)$, where I_1 and I_0 are the mean currents on the marks and the spaces respectively and σ_1 and σ_0 are the corresponding standard deviations. The commonly used *Q*-factor formula [23], [24] is based on several simplified assumptions: (1) It assumes a rectangular optical filter; (2) it assumes an integrate-and-dump electrical filter; (3) it only considers two extreme cases of the noise polarization: the noise is either unpolarized or completely copolarized in the direction of the signal. Under the third assumption, the *Q*-factor has a unique relationship with the SNR. However, the third assumption is not generally valid in today's long-haul transmission systems, where the noise is often partially polarized due to PDL in the system, and the direction of the polarized part of the noise can be arbitrary. A generalized *Q* formula, which

can accurately take into account the partially polarized noise, is essential in the receiver model.

In my study, I have derived a generalized *Q*-factor formula that accounts for the partially polarized noise in the receiver, as well as the pulse shape in front of the receiver and the shape of both the electrical filter and the optical filter. I validate this formula by the comparison to back-to-back experimental results, numerical simulations and theoretical calculations. In addition, I derive the probability density function (pdf) of the *Q*-factor when the SNR is fixed. I validate the pdf of the *Q*-factor by numerical simulation and experimental measurement. In Chapter 3, I discuss in detail the derivation of the *Q*-factor formula, the derivation of the pdf of the *Q*-factor when SNR is fixed and the experimental and simulated results.

Although the distribution of the PMD statistics has been studied in a short recirculating fiber loop [17], there have been relatively few published studies on the effects of PDL and PDG in such loops and on the differences between recirculating loops and straight-line systems. In my study, I have focused on the investigation of the polarization evolution in a recirculating loop as well as the loop performance due to these polarization effects. In Chapter 4, I systematically investigate the polarization evolution and the system performance in a loop system through numerical simulations using the reduced Stokes model and experiments. I focus on the evolution of the degree of polarization (DOP) of the signal and the noise in the loop, which provides the first experimental validation of the reduced Stokes model and leads to an approach to determine the amount of PDL in the system, the *Q*-factor distribution, and the polarization state evolution yielding *Q*-factors in the high *Q*, medium *Q* and low *Q* portions of the *Q*-factor distribution, respec-

tively. In addition, I numerically compare the polarization behavior of a loop system to a straight-line system.

The ultimate goal of my study is to overcome the limitation of recirculating loop systems and to accurately emulate the system performance of a straight-line system. In this study, I suggest an experimental procedure — the loop-synchronous scrambling technique, to obtain a more realistic *Q* factor distribution, which I also implement experimentally. With this approach, I introduce a random rotation each round trip, so that I am able to emulate the *Q*-factor distribution of a straight-line system and to investigate the PDL effect in such a system. I also employ an input scrambler to reduce the PDG effect in the single channel system used in experiments. Employing the *Q* formula in the reduced Stokes model, I obtain excellent agreement between experimental results and the numerical simulations after transmitting the signal over 10,000 km.

In Chapter 5, I discuss in detail the system performance of a scrambled loop system with different PDL levels, with and without the input scrambling. In this chapter, I describe several important techniques that used to carry out experiments. Besides the loop-synchronous scrambling technique, I discuss the control and monitoring of the magnitude of PDL in the system, as well as the EDFA dynamic response and its impact to the amplitude modulation induced by input scrambling, where the residual PDL in the system converts the polarization state modulation to the undesired amplitude modulation. I also discuss the technique to minimize the undesired amplitude modulation.

In conclusion, I show that the PDL plays a major role in the system performance, and, along with the periodic optical path, leads to polarization behaviors that are far from those in a realistic straight-line system. My work suggests that to truly reproduce the

straight-line behavior in a loop system, one needs to scramble the polarization state in the loop randomly. Finally, I summarize my work in Chapter 6.

Chapter 2

Application of the Reduced Stokes Model in a Loop System

2.1 Introduction

It is now commonplace to study fiber system impairments using the coupled nonlinear Schrödinger equation that has been modified to include loss, amplification, spontaneous emission noise and other effects [20] and [25]. When polarization effects, including PMD, can be neglected and the signal is launched in a single state of polarization, it is possible to study optical fiber impairments using the scalar nonlinear Schrödinger equation and its modifications. In fact, this scalar approach is more commonly used than the complete vector equation. However, as the bit rate of the optical system increases, the polarization effects have become more important. Polarization effects can impair the system performance severely. As a matter of fact, even using modern fibers, PMD is a significant issue in systems with a 40 Gb/s and higher data rate [26].

Furthermore, in order to reduce the effect of PDG, modern systems also employ polarization scrambling [27] or orthogonal polarization when launching the input signal

[28]. In these cases, the scalar nonlinear Schrödinger, which deals with a single input polarization state, is no longer valid. In these systems, the Manakov-PMD equation is the correct formulation to study the nonlinearity and dispersion in the systems [18]. Solving either the scalar nonlinear Schrödinger equation or the Manakov-PMD equation can be very computationally time consuming, especially for the WDM system involving large number of channels. To appropriately study polarization effects, one must additionally simulate many different fiber realizations of the random varying polarization orientations in the system, so that it is not realistic to study the impairments introduced by polarization effects in modern DWDM systems that may have tens of channels using complete numerical simulations to solve the nonlinear Schrödinger equation or the Manakov-PMD equation.

In a system, if the fiber's PMD is too small to distort a single pulse, PMD, PDL and PDG are treated as slow time effects that will raise and lower the signal and noise power levels and will change the polarization state of the entire channel in the same way. In contrast, nonlinearity and chromatic dispersion are fast effects that affect each bit separately. Since the polarization effects and the effects of nonlinearity and dispersion exist on different time scales, an effective reduced model that separates the impairments due to polarization effects from other effects is highly desirable.

The reduced model introduced by Dr. Ding Wang and Dr. Curtis Menyuk [21] is based on following the Stokes parameters for the signal and the noise for every channel, neglecting intersymbol interference due to the Kerr nonlinearity and chromatic dispersion. Although this model was developed to simulate the polarization effects in a WDM system, it is possible to apply it to a single-channel system. Before the loop experiments

that I accomplished, this model was only validated theoretically by comparing the results with a full simulation solving the Manakov-PMD equation [22]. The experiments, which will be discussed in Chapter 4, provide the first experimental validation of this model.

The dispersion-managed soliton (DMS) recirculating system, in which I used to carry out experiments, is a well-studied system [20], which has a threefold benefit for validation of the reduced model. First, in this loop, we were able to propagate dispersion-managed solitons over 18,000 km error-free, so that it is possible to study the accumulated polarization effects even though these effects are small in one round trip. Second, although the local dispersion in the system is large, the average dispersion is low and balances the nonlinearity of the system, so the pulses maintain their shape after each one round trip. Thus, pulse distortion due to nonlinearity and dispersion is eliminated. Third, the limitation of the propagation in this system is the build-up of the ASE noise and the change of the polarization orientation only varies the optical signal-to-noise ratio, rather than introducing extra pulse distortion. Moreover, since the system employs new fibers, the PMD is not significant enough to induce pulse distortion in the system. Consequently, it is reasonable to expect that this reduced model will work well in the study. In the reduced model, besides the polarization effects—PDL, PDG and PMD—I also took into account gain saturation of the EDFAs and the fiber loss.

The Jones vector of an electrical field, $\mathbf{U}(z,t)$, in the time domain is defined as

$$\mathbf{U}(z,t) = \mathbf{U}_0 \exp(ikz - i\omega t), \tag{2.1}$$

where ω is the center frequency of the channel and k is corresponding wave-number. The variable $\mathbf{U}_0$ is the wave envelope, which contains two orthogonal components u_1 and u_2. The drawback of the Jones notation is that it only describes completely polarized light. In

the reduced model, I use the Müller representation, which is more general and describes the unpolarized and partially polarized light. The polarization state of the light is described by four Stokes parameters, defined as

$$S_0 = \lim_{T\to\infty} \frac{1}{2T} \int_{-T}^{T} \left(|u_1|^2 + |u_2|^2 \right) \mathrm{d}t , \tag{2.2}$$

$$S_1 = \lim_{T\to\infty} \frac{1}{2T} \int_{-T}^{T} \left(|u_1|^2 - |u_2|^2 \right) \mathrm{d}t , \tag{2.3}$$

$$S_2 + iS_3 = \lim_{T\to\infty} \frac{1}{T} \int_{-T}^{T} u_1 u_2^* \, \mathrm{d}t . \tag{2.4}$$

In order to make this definition meaningful, the time constant T is long compared to a single bit period, and I assume that the channel is statistically stationary.

How polarized the light is is measured by DOP, which is defined as the power ratio of the polarized light and the total light. It can be written as

$$\mathrm{DOP} = \frac{\sqrt{S_1^2 + S_2^2 + S_3^2}}{S_0} . \tag{2.5}$$

2.2 Effect of PMD

Despite the name, there exist two mutually orthogonal polarization modes in a “single-mode” fiber. In a perfectly isotropic, circularly symmetric fiber the two polarization modes travel with the same phase and group velocity [17]. However, due to the stress applied to the fiber and the geometric asymmetry, this polarization degeneracy is broken, leading to fiber birefringence. Because of birefringence in the fiber, the two polarization modes travel at different group velocities, and random change of the birefringence along the fiber causes random mode coupling between these two modes [29]. The resulting

PMD leads to pulse distortion and system impairment that can limit the transmission distance of practical optical transmission systems.

In a system, where the PMD is too small to cause pulse distortion, such as the systems employed modern fiber, the polarization states in a single channel all evolve uniformly. This approximation is reasonable as long as the accumulated differential group delay (DGD) in the channel is not significant compared to the bit duration [25]. Therefore, the effect of the randomly varying birefringence in this system is to rotate the polarization state of the entire channel. This rotation occurs rapidly, typically on a scale of tens to hundreds of meters. Residual PMD can lead to a differential rotation of the polarization state of different channels in a WDM system that occurs over a much longer length scale. In the simulations, I apply the coarse step method in an optical fiber with randomly varying birefringence [18]. The simulation approach uses step sizes that are large compared to the fiber correlation length — typically several kilometers — and randomly rotate the polarization states on the Poincaré sphere after each step. In one step, the PMD is assumed to be a constant, so that the rotation induced by PMD is the same for each step, but it depends on wavelength. Then, the polarization state is rotated randomly on the Poincaré sphere after each step. The random rotations are chosen in such a way that for a fixed input polarization state, the output polarization state after the rotations cover the Poincaré sphere uniformly. This approach unnaturally increases fiber correlation length, while it artificially reduces the strength of the birefringence so that one can still obtain the same magnitude of the linear PMD and reduce the computation time dramatically. Marcuse, *et al*. [18] showed that this approach leads to the same statistical behavior as a

fine-step method that follows all the details of the birefringence evolution in an optical fiber.

The fiber loss is always compensated by the EDFAs along the transmission, so that one may ignore the spatially varying gain and loss when we consider the rotation due to PMD effect [22]. Since the PMD does not affect the total power of the channel, we can write the evolution of the total power, indicated as one of the Stokes parameters S_0, as a function of the propagation distance z as $S_0(z+\zeta)=S_0(z)$, where the parameter ζ is the step size used in the simulation. In the model, I follow the evolution due to PMD of the other three Stokes parameters. These three Stokes parameters form a Stokes vector $\mathbf{S}=(S_1,S_2,S_3)^t$. The *j*-th step of the Stokes vector is

$$\mathbf{S}(z+\zeta)=\mathbf{R}_j(z)\mathbf{M}_j(z)\mathbf{S}(z), \tag{2.6}$$

where the subscript *j* indicates the *j*-th step in the algorithm. The matrix,

$$\mathbf{M}j=\begin{pmatrix}1 & 0 & 0\\ 0 & \cos(\Delta\beta'\omega\zeta) & -\sin(\Delta\beta'\omega\zeta)\\ 0 & \sin(\Delta\beta'\omega\zeta) & \cos(\Delta\beta'\omega\zeta)\end{pmatrix}, \tag{2.7}$$

accounts for the wavelength-dependent rotation due to the fiber birefringence. The angular frequency ω is for the center wavelength of the channel. For the single channel that I studied, it is the same on each step. The quantity of $\Delta\beta'$ in (2.7) is related to the measured PMD or average differential group delay (DGD) as:

$$\Delta\beta'=\left(\sqrt{3\pi}/8\right)\ (2/\zeta)^{1/2}\ \text{PMD}\,. \tag{2.8}$$

The matrix

$$\mathbf{R}_j = \begin{pmatrix} \cos\theta_j & \sin\theta_j \cos\psi_j & -\sin\theta_j \sin\psi_j \\ -\sin\theta_j \cos\phi_j & \cos\theta_j \cos\phi_j \cos\psi_j - \sin\phi_j \sin\psi_j & -\cos\theta_j \cos\phi_j \sin\psi_j - \sin\phi_j \cos\psi_j \\ -\sin\theta_j \sin\phi_j & \cos\theta_j \sin\phi_j \cos\psi_j + \cos\phi_j \sin\psi_j & -\cos\theta_j \sin\phi_j \sin\psi_j + \cos\phi_j \cos\psi_j \end{pmatrix} \tag{2.9}$$

induces the random rotation at the end of each step that is required by the coarse step method. It is the same for each wavelength but differs on each step. On each step, $\cos\theta_j$ has a uniform distribution between –1 and 1, while ϕ_j and ψ_j are uniform distributed from 0 to 2π. Therefore, this rotation has a uniform probability distribution on the Poincaré sphere.

2.3 Effect of PDL

The PDL effect is due to the polarization dependence of the transmission of some devices. Physical effects, such as polarization-dependent absorption, fiber bending, and angled optical interfaces can cause PDL. In optical systems, polarization-sensitive elements such as isolators and WDM couplers in amplifiers are the main source of polarization-dependent loss. The effect of PDL is to cause excess loss in one of the two orthogonal polarizations. There are several methods to determine the PDL in a device. The most straightforward method is called the maximum-minimum power method. Using this approach, one needs to scan all the possible polarization states at the input of the device and trace the power variation at the output. From the ratio of the maximum power $P_{\max}$ and minimum power $P_{\min}$, one can obtain the PDL value in dB as

$$\mathrm{PDL} = 10\log_{10}\left(\frac{P_{\max}}{P_{\min}}\right). \tag{2.10}$$

Typically, for a single device the PDL level can vary from a few tenths of a dB to less than a tenth of dB. In long-haul transmission systems, the PDL will accumulate along the transmission distance. In transoceanic systems, the requirement for the PDL in each EDFA is very strigent. It must be below 0.1 dB. However, in terrestrial systems, the PDL for each EDFA is higher and can be a few tenths of a dB. Although, the PDL in the system does not significantly degrade the average signal-to-noise ratio (SNR), it may cause large variation of the SNR. In addition, in modern systems, polarization scrambling techniques are employed to improve the average SNR by eliminating the effect of PDG [27]. However, significant PDL in the system will repolarize the initially depolarized signal, so that the system performance can be degraded again by the effects of PDG and PMD [30].

Since PMD in the DMS system that I performed experiments is very low and I need only consider the polarization rotation due to the random varying birefringence, the entire channel has the same evolution. In addition, the effect of PDG can be eliminated if the signal is scrambled faster than the response time of EDFAs at the input. Thus, PDL plays a larger role than PMD or PDG in the system performance. Although the PDL can in principle be compensated with commercial devices, it is very expensive to compensate each EDFA in a realistic long-haul system. For system modeling and performance prediction, it is essential to understand the effect of the PDL in long-haul systems.

In the notation, I used “in” and “out” to indicate the light that inputs to the element having PDL and the light that passes the PDL element. Using the Jones vector notation, one can write

$$\begin{pmatrix} u_1 \\ u_2 \end{pmatrix}_{\text{out}} = \begin{pmatrix} 1 & 0 \\ 0 & \alpha \end{pmatrix} \begin{pmatrix} u_1 \\ u_2 \end{pmatrix}_{\text{in}}, \tag{2.11}$$

where the second component of the matrix is in the direction of maximum loss, and α is the PDL of the element in the linear scale and one can obtain the PDL in dB through the relationship $\mathrm{PDL} = -20\log_{10}\alpha$. The vector $\mathbf{U} = (u_1, u_2)^t$ is the wave envelope of the channel. Converting to the Stokes representation using (2.2), (2.3) and (2.4), we obtain

$$S_{0,\mathrm{out}} = \frac{1+\alpha^2}{2} S_{0,\mathrm{in}} + \frac{1-\alpha^2}{2} S_{1,\mathrm{in}}, \tag{2.12}$$

$$S_{1,\mathrm{out}} = \frac{1-\alpha^2}{2} S_{0,\mathrm{in}} + \frac{1+\alpha^2}{2} S_{1,\mathrm{in}}, \tag{2.13}$$

$$S_{2,\mathrm{out}} = \alpha \;\; S_{2,\mathrm{in}}, \tag{2.14}$$

$$S_{3,\mathrm{out}} = \alpha \;\; S_{3,\mathrm{in}}. \tag{2.15}$$

From (2.12) – (2.15), I observe that the PDL in the system not only causes power fluctuations, which is indicated by the parameter $S_{0,\mathrm{out}}$, but also causes a rotation of the polarization state of the signal towards the low-loss axis of the PDL device.

2.4 Effect of PDG

The polarization-dependent gain will cause excess gain in the direction orthogonal to the signal [8], [9]. This effect will cause significant degradation of the SNR in a long-haul transmission system. There are two sources of polarization dependent gain [31]. One is polarization hole burning (PHB) and the other is the pump contribution of polarization. PHB arises when randomly orientated erbium ions in the glass media are selectively de-excited by a polarized incoming signal. The pump dependence comes from the selective excitation of erbium ions by absorption of the polarized pump. The effects of the pump-induced PDG, like those of conventional PDL, accumulate stochastically because the as-

sociated axes in different components are independent from each other. By contrast, the effect of PHB, which tracks the polarization state of the signal, accumulates deterministically. The amount of PDG induced by the PHB effect is closely related to the gain compression of an EDFA. For a single EDFA, the PDG level in dB can be estimated by an empirical relation [32]

$$\mathrm{PDG} \approx 0.027C - 0.001C^2, \tag{2.16}$$

where C is the gain compression in dB, defined relative to an input signal of –30 dBm. This approximation is accurate when the gain compression is less than 8 dB. In the model I only take into account the PDG induced by PHB.

The PDG is the largest for linearly polarized light. Although the local PDG depends on the axis of the ellipse, due to the EDFA's birefringence, the SOP of the light rotates randomly alone the erbium fiber in the EDFA, so that the dependence of PDG on the local ellipticity is averaged out. Therefore, the total PDG of an EDFA is independent of the ellipse. The net gain of the power for the orthogonal noise mode due to PDG is given by

$$g_{\mathrm{net}} = 10^{\frac{d_{\mathrm{pol}} PDG}{10}}, \tag{2.17}$$

where PDG is the maximum differential gain in decibels and the parameter d_{pol} is the degree of polarization of the entire channel [31].

The effect of PDG is modeled in a manner similar to that used to model PDL; however the direction of maximum gain must be chosen self-consistently with the existing signal in a given system. In Jones space, assuming a normalized unity gain for the electrical field along the major axis of the polarization ellipse, the gain for the electrical field along the minor axis is $g = g_{\mathrm{net}}^{1/2}$. Thus, we write

$$\begin{pmatrix} u_1 \\ u_2 \end{pmatrix}_{\text{out}} = \mathbf{R}\begin{pmatrix} 1 & 0 \\ 0 & g \end{pmatrix}\mathbf{R}^{-1}\begin{pmatrix} u_1 \\ u_2 \end{pmatrix}_{\text{in}} . \tag{2.18}$$

The rotation matrix **R** is determined by the overall polarization state of the incoming light since it is the polarization state that determines the orientation of the PDG, while $\mathbf{R}^{-1}$ is the inverse of **R**. The rotation matrix **R** is written as

$$\mathbf{R} = \begin{pmatrix} \cos(\varphi/2)\exp[-i(\phi+\psi)/2] & -\sin(\varphi/2)\exp[i(\phi-\psi)/2] \\ \sin(\varphi/2)\exp[-i(\phi-\psi)/2] & \cos(\varphi/2)\exp[i(\phi+\psi)/2] \end{pmatrix}. \tag{2.19}$$

I use Stokes vectors $\mathbf{S}_{\text{in}} = (S_{1,\text{in}}, S_{2,\text{in}}, S_{3,\text{in}})^t$ and $\mathbf{S}_{\text{out}} = (S_{1,\text{out}}, S_{2,\text{out}}, S_{3,\text{out}})^t$ to indicate the SOP of the input light and the output light of an EDFA, respectively. I introduce a unitary vector $\mathbf{s} = (s_1, s_2, s_3)^t$ to denote the direction of the input light in Stokes space. The three components of this vector is related to the input SOP as

$$s_1 = S_{1,\text{in}} \Big/ \sqrt{S_{1,\text{in}}^2 + S_{2,\text{in}}^2 + S_{3,\text{in}}^2} , \tag{2.20}$$

$$s_2 = S_{2,\text{in}} \Big/ \sqrt{S_{1,\text{in}}^2 + S_{2,\text{in}}^2 + S_{3,\text{in}}^2} , \tag{2.21}$$

$$s_3 = S_{3,\text{in}} \Big/ \sqrt{S_{1,\text{in}}^2 + S_{2,\text{in}}^2 + S_{3,\text{in}}^2} . \tag{2.22}$$

The elements of **R** are related to the Stokes vector of incoming signal, **s**, through the relationship $s_1 = |r_{11}|^2 - |r_{12}|^2$ and $s_2 + is_3 = 2r_{11}r_{12}^*$. Transforming from the Jones representation to the Stokes representation, I obtain

$$\mathbf{S}_{\text{out}} = -\frac{g^2-1}{2}S_{0,\text{in}}\mathbf{s} + \frac{g^2+1}{2}\mathbf{S}_{\text{in}} + \frac{(g-1)^2}{2}\mathbf{s}\times(\mathbf{s}\times\mathbf{S}_{\text{in}}), \tag{2.23}$$

$$S_{0,\text{out}} = \frac{g^2+1}{2}S_{0,\text{in}} - \frac{g^2-1}{2}\mathbf{s}\cdot\mathbf{S}_{\text{in}} . \tag{2.24}$$

Studies have shown that in modern terrestrial WDM systems, the PDG is effectively reduced by a large number of channels [10], [32]. Since PMD leads to a random walk-off of the channels with different center frequencies, the total degree of the polarization of all the channels is reduced dramatically. In a single-channel system, an effective way to reduce the PDG is to scramble the polarization state of the input signal faster than the response time of the EDFA. However, the polarization scrambling may cause undesired amplitude modulation if the system has residual PDL. The undesired amplitude modulation will cancel out the improvement due to reduction of the PDG. In Chapter 5, I will discuss in detail how to choose a scrambling rate to eliminate the undesired amplitude modulation.

2.5 EDFA model and gain saturation

In addition to compensating the fiber loss in the model, the EDFA is modeled as a PDG device followed by an ASE noise generator. In communication systems, EDFAs usually operate in the saturation regime in order to keep the output power nearly constant, so that in the model the output power of each EDFA is kept constant.

In the simulations, I follow the Stokes parameters of the signal $\left(S_0, S_1, S_2, S_3\right)$ and that of the noise $\left(S_{0,\text{noise}}, S_{1,\text{noise}}, S_{2,\text{noise}}, S_{3,\text{noise}}\right)$ separately. The Stokes parameters of the signal and those of the noise are initialized as $\left(P_{\text{in}}, P_{\text{in}}, 0, 0\right)$ and (0, 0, 0, 0) at the input of the system, respectively. When the signal and the noise propagate in the fiber and pass a PDL element, they experience the identical evolutions that are described as (2.6) and (2.12) – (2.15), respectively. The evolutions in the fiber include the rotation induced by the PMD

effect, which is described by (2.7), and the random rotations required by the coarse step method, described by (2.9).

In order to determine the direction of the PDG effect and the magnitude of the PHB, the knowledge of overall polarization state and the DOP of the entire system are required. In a WDM system [22], these two pieces of information are obtained by accumulating the Stokes parameters of the signal and the noise for all channels. For a single channel system, the overall Stokes parameters of the system are given by the sum of the Stokes parameters of the signal and the noise, which are written as

$$S_{0,\text{total}} = S_0 + S_{0,\text{noise}}, \tag{2.25}$$

$$\mathbf{S}_{\text{total}} = \mathbf{S} + \mathbf{S}_{\text{noise}}. \tag{2.26}$$

Therefore the degree of polarization is given by $d_{\text{pol}} = \left|\mathbf{S}_{\text{total}}\right| / S_{0,\text{total}}$. The evolution of SOP due to the PDG effect for both the signal and the noise is determined by (2.23) and (2.24), where the direction of the overall Stokes Vector, the vector **s,** is calculated from $\mathbf{S}_{\text{total}}$ by using (2.20), (2.21) and (2.22).

As an ASE noise generator, each EDFA adds the noise that is equally distributed in the directions parallel and orthogonal to the signal. These two noise modes are uncorrelated to each other. The noise is treated as a depolarized signal, so that the noise added by the EDFA changes the total power of the noise rather than the SOP of the noise. Accounting the two polarization modes of the noise, the noise power is given by

$$P_{\text{n}} = 2n_{\text{sp}}h\nu\left(G-1\right)\Delta f, \tag{2.27}$$

where n_{sp} is the spontaneous emission coefficient, G is the linear gain of the EDFA and Δf is the optical bandwidth. The Stokes parameters of the noise are

$$S_{0,\text{noise,out}} = S_{0,\text{noise,in}} + P_{\text{n}}, \tag{2.28}$$

$$\mathbf{S}_{\text{noise,out}} = \mathbf{S}_{\text{noise,in}}. \tag{2.29}$$

In order to take into account the saturation of EDFA, the gain of the EDFA, G, is adjusted so that the total output power of the EDFA is constant and equal to P_{in}, denoted as

$$\frac{S_{0,\text{total}}}{\alpha_{\text{fiber}}} G + P_{\text{n}} = P_{\text{in}}. \tag{2.30}$$

Then using (2.27), the gain of the EDFA can be written as

$$G = \frac{2n_{\text{sp}}h\nu\Delta f + P_{\text{in}}}{2n_{\text{sp}}h\nu\Delta f + \dfrac{S_{0,\text{total}}}{\alpha_{\text{fiber}}}}, \tag{2.31}$$

where the parameter α_{fiber} is the linear loss of the fiber span. The optical signal to noise ratio (OSNR) at the distance we are interested is calculated by $\text{OSNR} = S_0 / S_{0,\text{noise}}$.

2.6 Simulation of a recirculating loop

The fundamental difference between a recirculating loop system in a laboratory and a realistic straight-line system is that the fiber realization in a recirculating loop changes slowly. The optical path of the loop may remain the same polarization configuration for hours, so that the light circulating in the system experiences a periodic birefringence. However, in a realistic straight-line system, the fiber realization changes randomly along the entire length of the fiber.

In the simulation, I use the coarse step method discussed previously. The step size of the simulation is 1 km. In order to simulate the periodicity of the optical path in a recirculating loop system, I first generate a set of rotations, which are chosen in such a way that

the output SOPs cover the Poincaré sphere uniformly, for the first round trip. For the following round trips, this set of rotations is repeated. Therefore, as the signal propagates in the system, it experiences the same rotation at the same point of the system. In order to study polarization effects, multiple fiber realizations are necessary. This is realized by choosing different sets of random rotations independently, so that each set of the rotations corresponds to one fiber realization.

In a straight-line system, the PDL elements are considered distributed and the accumulated PDL in the system has a Maxwellian distribution [34]. However, in a recirculating loop system, due to the steady nature of the system, the relative axes of PDL elements are fixed. Consequently, it is possible to lump all the PDL elements in one round trip together to obtain one effective PDL element. Taking into account the periodicity of the optical path, every following round trip has the same effective PDL element.

Chapter 3

The receiver model

3.1 Introduction

An accurate receiver model is as critical as an accurate and efficient model of the transmission line in the design and performance evaluation of optical fiber communication systems. Two commonly used parameters to evaluate the system performance are the bit-error rate (BER) and the *Q*-factor. By assuming that the probability density functions of the currents on the logical ones (the marks) and on the logical zeroes (the spaces) are Gaussian distributed, the *Q*-factor gives a reasonable estimation of the BER in certain range ($>10^{-6}$) [35] and [36]. The BER and the *Q*-factor also depend on the characteristics of the receiver, the polarization state of the noise, and on the shape of the optical pulses after the transmission.

Another commonly used performance indicator is the optical signal-to-noise ratio (OSNR), which is easier to measure in experiments. Unlike the BER or the *Q*-factor, this parameter does not rely on the detailed characteristics of the receiver. However, the rela-

tionship between the *Q*-factor and OSNR is not straightforward. Lightwave systems with optical amplifiers are especially vulnerable to the degradation due to PDL and PDG, which can cause a polarized signal to be attenuated or amplified differently from unpolarized noise [37]. Therefore OSNR changes accordingly. These effects make it complicated to evaluate the system performance, especially since the polarization effects are random in nature. In addition to assuming an integrate-and-dump receiver, the commonly used *Q* formula [23], [24] only considers two extreme cases, in which the noise is unpolarized or copolarized with the signal. Partially polarized noise occurs in many optical systems with significant PDL [37], [38]. How the partially polarized noise affects the system performance remains unclear.

When a system has pattern-dependent effects, the relationship of the *Q*-factor and the OSNR becomes more complicated, but this issue is not the focus of my study. In my study, I concentrate on the systematic investigation of effects of partially polarized noise in a receiver and compute the *Q*-factor using an accurate formula that takes into account the effect of partially polarized noise. This formula provides an analytical approach to calculate the *Q*-factor, so that it is not necessary to carry out Monte Carlo simulations in the time domain, if the optical pulse formats immediately prior to the receiver, as well as the shapes of the optical and electrical filters are known. The cost of computing the *Q*-factor is significant reduced by using this formula. Furthermore, this formula does not need the information about each bit during the propagation, so that it can be associated with the reduced Stokes model to study polarization effects [38].

I validate this formula by comparison of the experimental and simulated results. I show that, even with a fixed SNR, the performance of the system can vary widely, de-

pending on the relation between the polarization states of the signal and of the polarized part of the noise as well as on the DOP of the noise. I also derive an analytical formula for the *Q*-factor distribution when the SNR and DOP of the noise are fixed.

3.2 *Q*-factor definition and measurements

3.2.1 *Q*-factor definition

A fundamental problem in the design of optical fiber systems is to achieve the desired BER after the signal propagates through the system. Typically, the acceptable BER limit, which one considers error free is 10^{-9} or even lower. This limit can be extended up to 10^{-4} by using forward-error correcting codes [39], [40]. However, the BER may be difficult to measure due to the long measurement time required to accumulate enough errors to determine the error rate correctly. For instance, if a BER of 10^{-15} is measured in a 10 Gbit/s system, at least 10^{16} bits must be collected during the measurement, which will take more than ten days to finish. So system designers often use the *Q*-factor to evaluate the system performance. While the exact probability density function for the optical noise is not Gaussian, the Gaussian approximation is close to the actual BER in a certain BER range [35], [36]. Under this assumption the probability density function of the marks and spaces are described as

$$f_1(i) = \frac{1}{\sqrt{2\pi}\sigma_1} e^{-\frac{(i-I_1)^2}{2\sigma_1^2}}, \tag{3.1}$$

$$f_0(i) = \frac{1}{\sqrt{2\pi}\sigma_0} e^{-\frac{(i-I_0)^2}{2\sigma_0^2}}, \tag{3.2}$$

where I_1 and I_0 are the mean values of electrical current in the marks and spaces at the sampling time, and σ_1 and σ_0 are the corresponding standard deviations, respectively. For a given threshold i_d, the error probability for mistaking a mark for a space is given by the expression

$$P_1(i_d) = \int_{-\infty}^{i_d} f_1(i)\,\mathrm{d}i\,. \tag{3.3}$$

Similarly, the error probability for mistaking a space for a mark is given by

$$P_0(i_d) = \int_{i_d}^{\infty} f_0(i)\,\mathrm{d}i\,. \tag{3.4}$$

If marks and spaces are sent with equal probability, the total probability of an error in detecting either a space or a mark is defined as the BER:

$$\mathrm{BER} = \frac{1}{2}\left[P_1(i_d) + P_0(i_d)\right]. \tag{3.5}$$

The BER at the decision level i_d is given by

$$\mathrm{BER}(i_d) = \frac{1}{2}\left[\mathrm{erfc}\left(\frac{I_1 - i_d}{\sigma_1}\right) + \mathrm{erfc}\left(\frac{i_d - I_0}{\sigma_0}\right)\right]. \tag{3.6}$$

The complementary error function erfc(x) is defined as

$$\mathrm{erfc}(x) = \frac{1}{\sqrt{2\pi}}\int_x^{\infty} e^{-\beta^2/2}d\beta \approx \frac{1}{x\sqrt{2\pi}}e^{-x^2/2}\,. \tag{3.7}$$

The minimum BER is obtained with an optimized decision level i_d. Setting the derivative of (3.5) with respect to i_d equal to zero, and considering (3.3) and (3.4), we have

$$f_1(i_d) = f_0(i_d)\,. \tag{3.8}$$

The exponents of $f_1(i_d)$ and $f_0(i_d)$ yield the definition of the Q-factor,

$$Q = \frac{i_d - I_0}{\sigma_0} = \frac{I_1 - i_d}{\sigma_1} = \frac{I_1 - I_0}{\sigma_1 + \sigma_0}. \tag{3.9}$$

Then the *Q*-factor is directly related to the BER by

$$\text{BER} = \text{erfc}(Q), \tag{3.10}$$

For $Q \gg 1$, the expression for BER becomes

$$\text{BER} \approx \frac{1}{\sqrt{2\pi}Q} e^{-\frac{Q^2}{2}}. \tag{3.11}$$

3.2.2 *Q*-factor measurements

In general, there are two methods that are commonly used in the *Q*-factor measurement. One is to use the eye diagram displayed on an oscilloscope to obtain the statistics of the marks and the spaces; the other is to extract the value of *Q*-factor from the BER margin measurements.

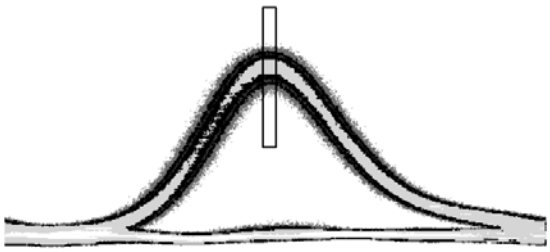

Fig. 3.1. Histogram window at logic ones for RZ pulses.

The first method is straightforward. During the measurement, as the eye diagram is been displaying on the oscilloscope, one needs to define the sampling window by using a narrow histogram window. As an example, Fig. 3.1 shows a histogram window at logic ones for return-to-zero (RZ) pulses. After collecting enough waveform trails on the oscil-

loscope, one is able to obtain the statistics in the histogram window of the waveforms, i.e. the mean and the standard deviation. The *Q*-factor is calculated by (3.9). In order to obtain a good measurement one must keep the histogram window narrow enough so that the effect of the phase jitter is eliminated. In the meantime, one also needs to collect enough samples in the histogram window to obtain good statistics. As a consequence, this procedure is time-consuming.

In a loop system, this procedure is even slower, because to measure any parameter corresponding to certain distance, the instrument is gated, which only measures the incoming signal in certain data window, usually a time period less than one round trip time (about 0.4 ms in the DMS loop). Additionally, the duty cycle of the gate signal depends on the maximum propagation distance in the loop system. The time period of the cycle can be more than a hundred milliseconds. Practically, it is almost impossible to collect enough sampling point when the system has very good performance. So, in these cases, the tails of the probability distribution of the marks and the spaces are missing.

The second method is to extract the *Q*-factor from the BER margin measurements [36]. The measured BER via the decision level i_{d} is separated into two sections at the point that yields the minimum BER or any point that yields error-free performance during the specified time-period. When the decision level is close to the marks, the errors are dominated by the logical ones that are sent by the transmitter and are detected as logical zeros at the decision circuit. Then BER(i_{d}) is dominated by the first erfc(x) function and the contribution from the second erfc(x) function is negligible. Similarly, if the decision level is set close to the spaces, BER(i_{d}) is dominated by the second erfc(x) function. Therefore, for each section, the BER is given by a single $\mathrm{erfc}(x)/2$ function written as

$$\mathrm{BER}(x) = \frac{1}{2}\mathrm{erfc}(x), \tag{3.12}$$

$$x = \frac{\left|I_{1,0} - i_{\mathrm{d}}\right|}{\sigma_{1,0}}. \tag{3.13}$$

In order to simplify the calculation, I first take the logarithm of both sides of (3.12). Since $\log[\mathrm{erfc}(x)/2]$ is a smooth, monotonic function that can be inverted by many numerical methods. To ease the computation, I use a polynomial fit to obtain

$$x = -0.0009 \times y^4 - 0.0265 \times y^3 - 0.3032 \times y^2 - 1.9674 \times y - 0.9002, \tag{3.14}$$

$$y = \log(\mathrm{BER}). \tag{3.15}$$

Compared to the polynomial fit used in [36], which is accurate to ±0.2% over the range of BER's from 10^{-5} to 10^{-10}, this approximation gives an accuracy of ±0.1% over the range of BER's from 10^{-1} to 10^{-12}. Given the decision level i_{d}, one can obtain the parameter *x* from the measured BER by using (3.14) and (3.15). Using (3.13), one can find that the parameter *x* is a linear function of the decision level i_{d}. When *x* via the decision level i_{d} is plotted for each rail, the equivalent I_1, I_0, σ_1 and σ_0 are the corresponding intercepts and slops, respectively. In all the experiments described in the following sections, the *Q*-factor is obtained from the BER margin measurements, unless otherwise indicated.

3.3 Enhancement factor

In practice, the *Q*-factor is often computed from the signal-to-noise ratio of the electrical current at the sampling time, which is defined as SNR = $(I_1 - I_0)/ I_0$ [23]. The elec-

trical SNR depends on the pulse shape and the receiver characteristics. In contrast, in the reduced model, one can directly compute the OSNR, which is independent of the pulse shape and the receiver characteristics. The OSNR is defined as the ratio of the average optical power of the signal to that of the noise. In order to correlate the electrical SNR to the OSNR, I introduce an enhancement factor ξ, which is defined as the ratio of the SNR to the OSNR,

$$\xi = \frac{\mathrm{SNR}}{\mathrm{OSNR}} = \frac{\left(I_1 - I_0\right) P_{\mathrm{n}}}{I_0 \; P_{\mathrm{s}}}, \tag{3.16}$$

where the parameters P_{s} and P_{n} are the average optical power of the signal and the noise, respectively. These two parameters can be measured by an optical spectrum analyzer. In the reduced Stokes model these two quantities are expressed as the Stokes parameters S_0 and $S_{0,\mathrm{noise}}$.

The enhancement factor quantifies how efficiently the combination of the pulse shape and receiver translates the OSNR into the SNR of the electric current of the marks and the spaces at the sampling time of the receiver. When the pulse shape and the receiver are known, the enhancement factor is a deterministic parameter. With the enhancement factor, it is appropriate to express the *Q*-factor using the OSNR. Thus, to obtain an accurate *Q*-factor from the numerical simulations using the reduced Stokes model becomes feasible. In the simulation, based on the pulse shape and the receiver in experiments, the enhancement factor is set to be 3.4 and $\mathrm{SNR} = \xi\ \mathrm{OSNR}$. The detailed experimental setup will be discussed in Section 3.6.

3.4 Effect of partially polarized noise in a receiver

In this study, I compute the *Q*-factor using an accurate receiver model that takes into account the effect of partially polarized noise, the optical pulse shape immediately prior to the receiver as well as the shapes of the optical and electrical filters. I also derive an analytical formula for the *Q*-factor distribution when the SNR and DOP of the noise are fixed.

In [23] and [24], by assuming that the noise is unpolarized or copolarized with the signal, a given SNR corresponds to a specific *Q*-factor. However, in real systems, the relationship between the SNR and the *Q*-factor is not unique, especially when the noise is partially polarized or totally polarized but not copolarized with the signal. In a system that has an infinite extinction ratio, the variances σ_0^2 and σ_1^2 are related to the variances due to the noise-noise beating, denoted as $\sigma_{\text{ASE-ASE}}^2$, and the variance due to the signal-noise beating, denoted as $\sigma_{\text{S-ASE}}^2$. The relationships can be written as

$$\sigma_0^2 = \sigma_{\text{ASE-ASE}}^2, \tag{3.17}$$

and

$$\sigma_1^2 = \sigma_{\text{ASE-ASE}}^2 + \sigma_{\text{S-ASE}}^2. \tag{3.18}$$

Although the mean value of the currents I_0 and I_1 are polarization-independent, the variances $\sigma_{\text{ASE-ASE}}^2$ and $\sigma_{\text{S-ASE}}^2$ depend on the SOP of both the signal and the noise, and so do σ_0 and σ_1. The variance due to the noise-noise beating, $\sigma_{\text{ASE-ASE}}^2$, depends on the DOP of the noise. The variance due to the signal noise beating, $\sigma_{\text{S-ASE}}^2$, depends both on the DOP of the noise and on the angle between the Stokes vectors of the signal and the polarized

part of the noise. When the noise is unpolarized, half of the noise beats with the signal. When the noise is completely co-polarized with the signal, all of the noise beats with the signal and the signal-to-noise beating is the strongest. On the other hand, if the completely polarized noise is antiparallel to the signal in Stokes space, then no noise beats with signal so that the signal-noise beating is the weakest.

Born and Wolf [41] show that any partially polarized light may be regarded as the sum of completely unpolarized light and completely polarized light. The Stokes vector **S** gives the direction of the polarization state and the length of this vector, $|\mathbf{S}| = \sqrt{S_1^2 + S_2^2 + S_3^2}$, gives the power of the polarized part of the light. If the light is unpolarized, these elements of the vector are equal to zero.

In the following derivations, the signal is assumed to be polarized, and it is denoted by the Stokes vector $\mathbf{S} = (S_1, S_2, S_3)^t$. The normalized Stokes vector, $\mathbf{s} = \mathbf{S}/|\mathbf{S}|$, gives the direction of the SOP of the signal on the Poincaré sphere. The noise is arbitrary polarized and is represented by $(S_{0,\text{noise}}, S_{1,\text{noise}}, S_{2,\text{noise}}, S_{3,\text{noise}})$, where $S_{0,\text{noise}}$ is the total noise power. The polarized part of the noise is given by $(|\mathbf{S}^{\text{P}}_{\text{noise}}|, S_{1,\text{noise}}, S_{2,\text{noise}}, S_{3,\text{noise}})$, where $|\mathbf{S}^{\text{P}}_{\text{noise}}|$ is the power of the polarized noise, given by $|\mathbf{S}^{\text{P}}_{\text{noise}}| = \sqrt{S_{1,\text{noise}}^2 + S_{2,\text{noise}}^2 + S_{3,\text{noise}}^2}$. Then the power of the unpolarized part of the noise is given by $S_{0,\text{noise}} - |\mathbf{S}^{\text{P}}_{\text{noise}}|$ and the Stokes vector of the unpolarized part of the noise is $\mathbf{S}^{\text{unP}}_{\text{noise}} = (0,0,0)^t$. One notes that the unpolarized noise influences the total power of the noise rather than the direction of the Stokes vector of the noise. The direction of the SOP of the noise, denoted as a unit vector

$\mathbf{p} = \mathbf{S}^{\mathrm{P}}_{\mathrm{noise}} \big/ \left|\mathbf{S}^{\mathrm{P}}_{\mathrm{noise}}\right|$, is determined by the polarized part of the noise. The DOP of the noise, denoted by $\mathrm{DOP}_{\mathrm{n}}$, is given by

$$\mathrm{DOP}_{\mathrm{n}} = \frac{\left|\mathbf{S}^{\mathrm{P}}_{\mathrm{noise}}\right|}{S_{0,\mathrm{noise}}}. \tag{3.19}$$

For unpolarized noise, the choice of coordinates is not critical to calculate the noise-noise beating, since for any orthogonal directions in Jones space, the noise in these two directions are uncorrelated to each other. Then the total variance of the noise-noise beating is simply the sum of the variances of the noise-noise beating in these directions. Also only the noise in the direction parallel to the signal contributes to the signal-noise beating. Therefore, in Jones space, it is common to choose the direction parallel to the signal and the direction orthogonal to the signal as the coordinates. The signal-noise beating is calculated in Jones space by projecting the noise power to the direction parallel to the signal [42] and the total noise-noise beating is the sum of the noise-noise beating in the directions that are either parallel or orthogonal to that of the signal in Jones space.

However, when part of the noise is polarized, the noise powers in the direction of the signal and the direction orthogonal to the signal can be correlated with each other [43]. To calculate the noise-noise beating, one must consider the covariance of the variances due to the noise-noise beating in each direction. In order to carry out the derivation, I choose a coordinates based on a direction parallel to the polarized part of the noise and a direction orthogonal to the polarized noise. The noise powers projected on these two directions are statistically independent of each other. Converting the coordinates to Stokes space, the noise power is divided to the direction of $\mathbf{p}$ and the direction antiparallel to $\mathbf{p}$.

The two projected noise powers are denoted as $N_{\mathbf{p}}$ and $N_{-\mathbf{p}}$, respectively. As a consequence, in Stokes space, the variance due to the noise-noise beating is written as

$$\sigma^2_{\text{ASE-ASE}} = B\left(N^2_{\mathbf{p}} + N^2_{-\mathbf{p}}\right)$$

$$= \frac{BS^2_{0,\text{noise}}}{2}\frac{2(N^2_{\text{p}} + N^2_{-\text{p}})}{S^2_{0,\text{noise}}}. \tag{3.20}$$

the variance due to the signal-noise beating is written as

$$\sigma^2_{\text{S-ASE}} = AS_0N_{\mathbf{p}}\left[\frac{1}{2}\left(1+\mathbf{s}\cdot\mathbf{p}\right)\right] + AS_0N_{-\mathbf{p}}\left[\frac{1}{2}\left(1-\mathbf{s}\cdot\mathbf{p}\right)\right]$$

$$= \frac{AS_0S_{0,\text{noise}}}{2}\left[1+\frac{N_{\text{p}} - N_{-\text{p}}}{S_{0,\text{noise}}}\mathbf{s}\cdot\mathbf{p}\right], \tag{3.21}$$

where the parameter S_0 is the total power of the signal. The constant *A* depends on the pulse shape, the detailed characteristics of the optical filer and the electrical filer. The constant *B* depends on the detailed characteristics of the optical filter and the electrical filter. The total noise power $S_{0,\text{noise}}$ is the sum of $N_{\mathbf{p}}$ and $N_{-\mathbf{p}}$.

If the noise is unpolarized, the unit vector $\mathbf{p}$ is in arbitrary direction in the Stokes space and $N_{\mathbf{p}} = N_{-\mathbf{p}} = S_{0,\text{noise}}/2$, so that the variance due to noise-noise beating is $\sigma^{2\,\text{unp}}_{\text{ASE-ASE}} = BS^2_{0,\text{noise}}/2$ and the variance due to the signal to noise besting is $\sigma^{2\,\text{unp}}_{\text{S-ASE}} = AS_{0,\text{noise}}S_0/2$. I introduce two parameters $\Gamma_{\text{ASE-ASE}}$ and $\Gamma_{\text{S-ASE}}$ to account the effect of partially polarized noise in the receiver. These two parameters are defined by

$$\Gamma_{\text{ASE-ASE}} = \frac{S^2_{0,\text{noise}}}{2\left(N^2_{\mathbf{p}} + N^2_{-\mathbf{p}}\right)}; \tag{3.22}$$

$$\Gamma_{\text{S-ASE}} = \frac{N_{\mathbf{p}}\left(1+\mathbf{s}\cdot\mathbf{p}\right)+N_{-\mathbf{p}}\left(1-\mathbf{s}\cdot\mathbf{p}\right)}{2S_{0,\text{noise}}}. \tag{3.23}$$

Then the parameter $\Gamma_{\text{ASE-ASE}}$, which has the range from 0.5 to 1, is the ratio of the variance due to the noise-noise beating, assumed that the noise is unpolarized to the noise-noise beating variance of an arbitrary polarized noise. The parameter $\Gamma_{\text{S-ASE}}$, which has a range from 0 to 1, gives the proportion of the noise that contributes to the signal-noise beating. In the special cases discussed in [23], with unpolarized noise, $\Gamma_{\text{ASE-ASE}} = 1$ and $\Gamma_{\text{S-ASE}} = 0.5$. While when the noise is copolarized with the signal, $\Gamma_{\text{ASE-ASE}} = 0.5$ and $\Gamma_{\text{S-ASE}} = 1$.

If the noise is partially polarized, the power in the direction parallel to the polarized part of the noise $N_{\mathbf{p}}$ contains all the polarized part of the noise $\left|\mathbf{S}^{\text{P}}_{\text{noise}}\right|$ and half of the unpolarized part of the noise $\left(S_{0,\text{noise}} - \left|\mathbf{S}^{\text{P}}_{\text{noise}}\right|\right)\big/2$ and the noise power $N_{-\mathbf{p}}$ contents half of the unpolarized part of the noise $\left(S_{0,\text{noise}} - \left|\mathbf{S}^{\text{P}}_{\text{noise}}\right|\right)\big/2$, so that I have that

$$N_{\mathbf{p}} = \frac{S_{0,\text{noise}} + \left|\mathbf{S}^{\text{P}}_{\text{noise}}\right|}{2}; \tag{3.24}$$

$$N_{-\mathbf{p}} = \frac{S_{0,\text{noise}} - \left|\mathbf{S}^{\text{P}}_{\text{noise}}\right|}{2}. \tag{3.25}$$

The DOP of the noise can be written as

$$\text{DOP}_{\text{n}} = \frac{\left|\mathbf{S}^{\text{P}}_{\text{noise}}\right|}{S_{0,\text{noise}}} = \frac{N_{\mathbf{p}} - N_{-\mathbf{p}}}{N_{\mathbf{p}} + N_{-\mathbf{p}}}. \tag{3.26}$$

Using (3.26), I also can write these two parameters $\Gamma_{\text{ASE-ASE}}$ and $\Gamma_{\text{S-ASE}}$ as a function of the DOP of the noise as

$$\Gamma_{\text{ASE-ASE}} = \frac{1}{1+\text{DOP}_{\text{n}}{}^{2}} \quad , \tag{3.27}$$

$$\Gamma_{\text{S-ASE}} = \frac{1}{2}\left(1+\text{DOP}_{\text{n}}\mathbf{s}\cdot\mathbf{p}\right). \tag{3.28}$$

These two parameters, which are coordinate-independent, depend on the DOP of the noise as well as the angle of the signal and polarized part of the noise in Stokes space.

The formula for the *Q*-factor is given by

$$Q = \frac{\text{SNR}}{1+\sqrt{1+2\Gamma_{\text{S-ASE}}\Gamma_{\text{ASE-ASE}}\kappa\text{SNR}}}\sqrt{\Gamma_{\text{ASE-ASE}}\mu}\,. \tag{3.29}$$

The parameters κ and μ in (3.29), which are independent of the polarization states of the signal and noise, depend on the pulse format and the shapes of the optical and electrical filters. The detailed derivation of κ and μ are discussed in [44]. In the special case of an integrate-and-dump receiver, where the noise is unpolarized or co-polarized with the signal, (3.29) agrees with the formula for the *Q*-factor given in [23]. For the receiver used in the experiments, $\kappa = 1.7$ and $\mu = 38.6$.

3.5 *Q*-factor distribution with a fixed SNR

From (3.27), (3.28), and (3.29), one observes that, for a fixed SNR, the *Q*-factor is a function of the DOP of the noise and the angle of the Stokes vectors of the signal and the noise, which is represented by the inner product of the unit vectors $\mathbf{s}\cdot\mathbf{p}$. If the polarization state of the signal is fixed and the polarization states of the polarized part of the noise uniformly cover the Poincaré sphere, $\mathbf{s}\cdot\mathbf{p}$ is uniformly distributed between –1 and +1 [45]. If a random variable *Y* is a monotonic function of a random variable *X*, written as

$Y = g(X)$, where g is a monotonic function and is invertible, then the random variable X can be calculated from the random variable Y using $X = g^{-1}(Y)$, where $x = g^{-1}(y)$ is the value of x for which $g(x) = y$ [46]. If the function g is also differentiable and the probability density function (pdf) of X is known, which is represented by $f_X(x)$, the pdf of Y can be calculated by the pdf of X . If the function g is a monotonically increasing function, the pdf of Y is

$$f_Y(y) = f_X\left[g^{-1}(y)\right]\frac{\mathrm{d}\, g^{-1}(y)}{\mathrm{d}y}. \tag{3.30}$$

Similarly, if the function g is a monotonic decreasing function, the pdf of Y is

$$f_Y(y) = -f_X\left[g^{-1}(y)\right]\frac{\mathrm{d}\, g^{-1}(y)}{\mathrm{d}y}. \tag{3.31}$$

The Q-factor is monotonically decreasing as $\mathbf{s}\cdot\mathbf{p}$ increases from –1 to +1 and I find after substituting (3.27) and (3.28) into (3.29), that (3.29) is differentiable with respect to $\mathbf{s}\cdot\mathbf{p}$. Therefore, the pdf of the Q-factor is given by

$$f_Q(q) = \frac{1}{\kappa \mathrm{DOP_n}}\sqrt{\frac{\mu}{\Gamma_{\text{ASE-ASE}}}}\left(\frac{\mathrm{SNR}\sqrt{\Gamma_{\text{ASE-ASE}}\,\mu}}{q^3} - \frac{1}{q^2}\right),\ q \in \left[Q_{\min}, Q_{\max}\right], \tag{3.32}$$

where $Q_{\max}$ and $Q_{\min}$ are given by substituting $\mathbf{s}\cdot\mathbf{p} = -1$ and $\mathbf{s}\cdot\mathbf{p} = +1$ respectively in (3.28) and calculating the Q-factor using (3.29).

3.6 Experimental setup

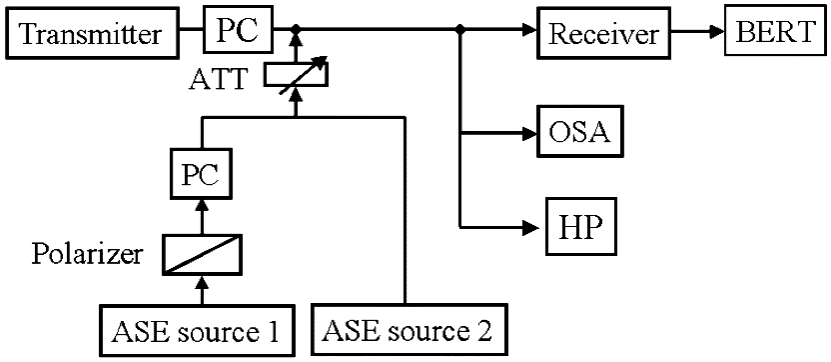

Fig. 3.2. Schematic diagram of the experimental setup.

In Fig. 3.2, I show a schematic diagram of the experimental setup. The transmitter included a CW light source centered at 1551.7 nm, an electro absorption modulator (EAM) and electro optical modulator (EOM). The EAM was driven by a 10 GHz sinusoidal signal to generate RZ pulses with the full-width-half-maximum (FWHM) of 23 ps. The EOM was modulated by a 2^{15} –1 pseudo random bit string (PRBS) pattern. Two EDFAs were placed after each modulator to compensate the loss. Each EDFA was followed by a 37.5 GHz optical filter to eliminate the optical noise from the EDFA, so that the optical noise from the transmitter was neglegible. The receiver included a 187.5 GHz optical filter, a PIN detector, and an electrical amplifier. In order to avoid the saturation of the receiver, I kept the total input optical power to the PIN detector at –2 dBm. The electrical bandwidth of the receiver was 10 GHz.

The optical noise in this setup was dominated by the amplified spontaneous emission (ASE) noise from the noise source, which combined outputs of two EDFAs without any input power. One EDFA generated unpolarized noise and the other one, followed by a polarizer and a polarization controller (PC), provided polarized noise. I used the PC after

the transmitter and the PC after the polarizer to vary the polarization state of the signal and the polarized noise, respectively. The SOP was monitored by a commercial polarization analyzer, HP8905B (HP). I varied the DOP of the noise by adjusting the relative power of the two noise sources. The signal-to-noise ratio (SNR) of the electrical current was held fixed at SNR = 10.9 dB by using a variable attenuator (ATT) to adjust the total noise power. I monitored the corresponding OSNR using an optical spectrum analyzer.

In order to concentrate on the system variations due to partially polarized optical noise, I subtracted the electrical noise background, which was measured when the noise source was off. The pdf of the electrical noise was assumed to be Gaussian distributed with zero mean and the variations due to the electrical noise at marks and spaces were represented by σ_{e1}^2 and σ_{e0}^2, respectively. Since the electrical noise was independent from the optical noise, the variation due to the optical noise at the marks and the spaces, σ_1^2 and σ_0^2 could be obtained by subtracting the variances due to electrical noise from the actual measured variances, σ_{m1}^2 and σ_{m0}^2, as $\sigma_1^2 = \sigma_{m1}^2 - \sigma_{e1}^2$ and $\sigma_0^2 = \sigma_{m0}^2 - \sigma_{e0}^2$.

3.7 Results and validation of the model

To validate the analytical formula of the *Q*-factor and the *Q*-factor distribution of the partially polarized noise, given by (3.29) and (3.32), respectively, I measured the *Q*-factor as a function of the angle between the Stokes vectors of the signal and the noise for the completely polarized noise and the partially polarized noise, as well as the *Q*-factor distribution of the partially polarized noise. In addition, I compared the experimental *Q*-factor distributions with Monte Carlo simulations. The comparisons yielded excellent

agreement. The results show that partially polarized noise causes performance variation even when the SNR is fixed.

3.7.1 Validation of *Q*-factor formula (3.29)

In the first experiment, I measured the *Q*-factor as a function of $\mathbf{s}\cdot\mathbf{p}$. The relative SOP of the signal and the noise was monitored using a commercial polarization controller, HP8509B (HP). Without turning on the noise source, the SOP of the signal was measured. In order to simplify the measurement, I adjusted the polarization controller after the transmitter to obtain a SOP of the signal as (1, 0, 0) on the Poincaré sphere, which was kept fixed and was checked regularly to avoid any drift during the measurement. Similarly, the SOP of the noise was measured when the signal was off. The SOP of the noise was adjusted by the setting of the polarization controller after the polarizer. Since the signal and the noise shared the same optical path after the coupler, which was fixed during the measurement, and the optical path only provided a global rotation of the SOPs, the inner product of the Stokes vector of the signal and the noise measured from HP was equivalent to that before the detector, which was denoted as $\mathbf{s}\cdot\mathbf{p}$ in (3.28).

By changing the setting of the PC after the polarizer I increased $\mathbf{s}\cdot\mathbf{p}$ from –1 to +1, thereby increasing the signal-noise beating and decreasing *Q*. In Fig. 3.3, I plot the *Q*-factor versus $\mathbf{s}\cdot\mathbf{p}$ when the noise was highly polarized and when it was partially polarized. When the DOP of the noise was set to 0.95, I show the experimental result and analytical result with filled circles and a solid curve respectively. I show the corresponding results when the DOP of the noise was 0.5 with filled diamond and a dashed curve. The agreement between analytical result and experiment is excellent. In both cases, the larg-

est Q value occurs when the signal is antipodal on the Poincaré sphere to the polarized part of the noise and the signal-noise beating is weakest. Similarly, the smallest Q value occurs when the signal is co-polarized with the polarized part of the noise and the signal-noise beating is strongest. Furthermore, as $\mathbf{s}\cdot\mathbf{p}$ varied from –1 to +1, the variation in Q is less when the noise is partially polarized than when it is highly polarized.

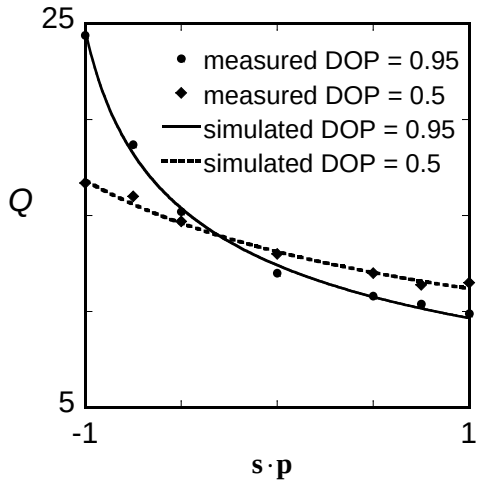

Fig. 3.3. Comparison of Q-factor as a function of $\mathbf{s}\cdot\mathbf{p}$. The experimental and analytical results when the DOP of the noise was set to 0.95 are shown with filled circles and a solid curve respectively. The corresponding results when the DOP of the noise was 0.5 are shown with diamonds and a dashed curve.

3.7.2 Validation of Q-factor distribution (3.32)

In the second experiment, I measured the distribution of the Q-factor when the DOP of the noise was $\mathrm{DOP_n}$ = 0.05, 0.25, 0.5, 0.75 and 0.95. The SNR was fixed at 10.9 dB. The SOP of the signal was kept fixed as described in the first experiment. The SOP of the

noise was varied randomly by adjusting the setting of the PC after the polarizer, so that the polarized noise covered the Poincaré sphere uniformly. The *Q*-factor was measured for each setting of the PC after the polarizer. For every DOP of the noise, I collected 200 samples of the *Q*-factors to obtain the distribution. In the simulation, I initiated the polarization states of the signal and of the polarized noise prior to the PC to be (1, 0, 0) in Stokes space and randomly rotated the polarized noise to uniformly cover the Poincaré sphere. The *Q*-factor was calculated by (3.27), (3.28), and (3.29).

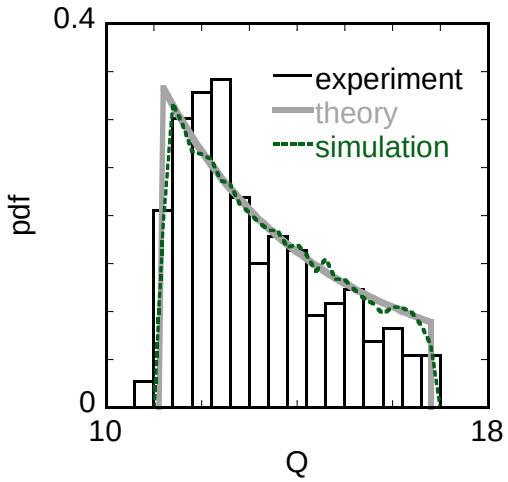

Fig. 3.4. Distribution of *Q*-factor when DOP_n = 0.5. I show the histogram of the measured *Q*-factor distribution with bars, the corresponding analytical result obtained using (3.32) with a solid curve, and the results that we obtained using a Monte Carlo simulation with 10,000 samples as a dotted curve.

In Fig. 3.4, I show the histogram of the measured *Q*-factor distribution with bars when DOP_n = 0.5. I also show the results that I obtained using a Monte Carlo simulation

with 10,000 samples as a dotted curve. The analytical result of the Q-factor distribution by using (3.32) is shown as a solid line in Fig. 3.4. The theoretical and simulation results both agree very well with the experimental result. The sharp cut-offs in the Q-distribution at Q = 11.4 and Q = 17 correspond to the cases in which the signal is respectively parallel and antipodal on the Poincaré sphere to the polarized part of the noise.

In Fig. 3.5, I show the $Q_{\max}$ and $Q_{\min}$ as a function of the DOP of the noise, obtained both from measurements, as filled circles and empty circles, respectively, and analytical calculation by substituting $\mathbf{s}\cdot\mathbf{p} = -1$ and $\mathbf{s}\cdot\mathbf{p} = +1$ respectively in (3.28) and calculating the Q-factor using (3.29) as a solid curve and a dotted curve, respectively. In order to investigate the mean system performance, I obtained the average Q-factor corresponding to different DOP of the noise by averaging the 200 Q-factor samples of each case. I show the result as triangles in Fig. 3.5. The analytical average Q-factor, shown as a dashed curve in Fig. 3.5, is obtained by using (3.32) to calculate the mean. Although the average Q is not sensitive to a change in the DOP of the noise, the maximum and minimum Q values change widely with the DOP of the noise, especially the maximum Q values. The result shows that highly polarized noise will cause a larger system variation than unpolarized noise.

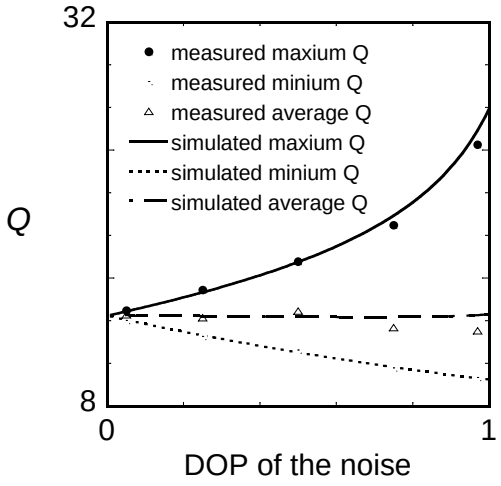

Fig. 3.5. The maximum Q-factor, Q_{max}, the minimum Q-factor, Q_{min}, and the average Q-factor as a function of the DOP of the noise. The filled circles, the empty circles and the triangles represent the measured data and the solid curve, the dotted curve and the dashed curve represent the corresponding analytical results.

3. 8 Conclusions

In this work, I systematically investigated effects of partially polarized noise in a receiver. I introduced an accurate Q-factor formula that accounts for partially polarized noise, derived an expression for the distribution of the Q-factor, and validated these results by comparison to back-to-back experiments as well as Monte Carlo simulations. The SNR alone would not give a complete picture of the system performance, since the relationship of the SNR and the Q-factor is not unique when the noise is partially polarized. The system variation caused by partially polarized noise not only depends on the angle between the Stokes vectors of the signal and polarized part of the noise but also depends on the DOP of the noise. Highly polarized noise will cause a larger variation in the

system performance compared to less polarized noise. My work suggests that in order to reduce the variation of the system performance, one should keep the noise unpolarized. One way to do so is to reduce the PDL in the system.

Chapter 4

Polarization evolution and *Q*-factor distribution in a recirculating loop

4.1 Introduction

Studies of polarization effects performed in recirculating loop systems have shown that as a matter of fact, the recirculating loop systems can not correctly emulate the polarization effects of straight-line systems [16], [17] and [37]. In my studies, I experimentally and theoretically investigated the DOP evolution, the polarization state evolution with different PDL levels in the system as well as corresponding statistics of the system performance, evaluated by the distribution of the *Q*-factor in a dispersion-managed recirculating system. As discussed previously, the effect of PMD in this system is to rotate the polarization state of the signal and the noise, so that it is reasonable to expect that the reduced Stokes model will provide an accurate simulation of the system performance associated with polarization effects. The excellent agreement between the experimental results and simulations validates the reduced Stokes model. The results show that the PDL

associated with the periodicity of the optical path can artificially improve the system performance by reducing the noise in the direction orthogonal to that of the signal. The system performance in a loop overestimates that of a straight-line system at the same distance.

4.2 Set up of the dispersion-managed recirculating loop

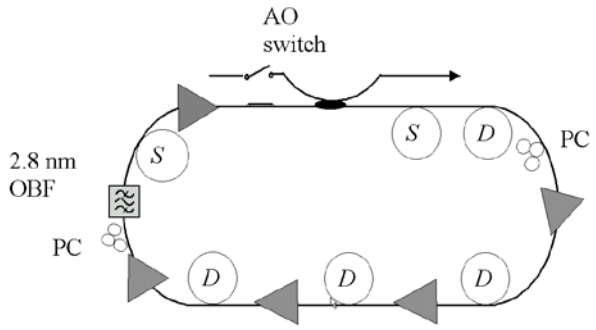

Fig. 4.1. Schematic diagram of the recirculation loop used in the study. *D*: dispersion-shifted fiber. *S*: single-mode fiber.

Fig. 4.1 shows a schematic diagram of the recirculating loop used in experiments. This configuration has been used to study the performance of dispersion-managed solitons at 10 and 20 Gbits/s over distances of 20,000 km [47] and [48]. Therefore, it is possible to study the accumulated polarization effects in the system even though these effects are small in one round trip. I placed two polarization controllers in the loop to adjust the polarizatin state of the signal and the noise.

The loop consists of a dispersion map with 100 km of dispersion shifted fiber with D = –1 ps/nm-km and two spans of 3.5 km of standard single mode fiber with D = 17 ps/nm-km. Four EDFAs are equally spaced to compensate for the fiber loss and a fifth EDFA is used to overcome the loss of the loop switch and coupler. Although the local

dispersion in the system is high, the average dispersion is low and balances the nonlinearity of the system, so the pulses maintain their shape after every round trip [20]. Thus, the increase of BER is mainly due to the build-up of the ASE noise generated by EDFAs.

In practice, the isolators and WDM couplers in the EDFAs are the primary source of the PDL in our loop. Due to the steady nature of the loop, the axis of every PDL component remains unchanged for a long time period, so it is reasonable to lump all the PDL effect together as an effective PDL element in the system.

4.3 DOP evolution of loop systems

4.3.1 DOP evolution of under different system performances

The DOP is defined as the ratio of the power of polarized light to the total optical power. In a single channel system, there are two mechanisms will cause the decreasing of the DOP of the entire channel. One mechanism is the effect of PMD, which cause the different polarization modes of the signal to propagate at different velocity in the fiber, thus depolarizing the signal. The other mechanism is the buildup of the ASE noise added by the EDFAs, which is depolarized. Since the PMD in the recirculating loop system used in my study is too low to distort the pulses, its effect on the DOP can be neglected. The decreasing of the DOP is primarily due to the build up of the ASE noise, and it is consistent with the decrease of the corresponding OSNR.

The performance of the recirculating loop, evaluated by the BER, varied greatly, depending on the setting of the polarization controllers. By optimizing the three polarization controllers, one at the transmitter and two in the loop, we were able to propagate 10 Gbit/s RZ pulses modulated by a $2^{15} - 1$ PRBS pattern over 20,000 km error free. In or-

der to investigate this correlation between polarization behaviors in the loop and the system performance, I measured the DOP evolution for several settings of the polarization controllers in the loop. The DOP of entire channel as a function of propagation distance was sampled using a commercial polarization analyzer, HP8509B.

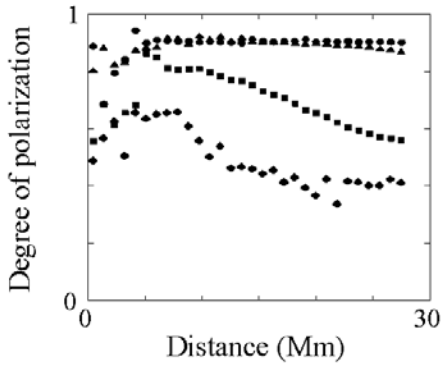

Fig. 4.2. Evolution of the degree of polarization as a function of the propagation distance for four different settings of the polarization controllers in the loop system. Circles, triangles, squares and diamonds represent the setting that yields a BER of 10^{-9}, 10^{-6}, 10^{-4} , 10^{-1} measured at 20,000 km, respectively.

In the experiment, I first optimized the setting of polarization controllers in the system to obtain a BER less than 10^{-9} at 20,000 km, which was considered error free, and then sampled the DOP of the signal plus the noise as a function of propagation distance. I show the result as circles in Fig. 4.2. When the settings of PCs in the system were changed, the BER at 20,000 km changed correspondingly. I show the DOP as a function of the propagation distance corresponding to a BER of 10^{-6}, 10^{-4}, 10^{-1} (measured at 20,000 km) as triangles, squares and diamonds, respectively. The results show that when the setting of PCs in the system is optimized to obtain the lowest BER, the signal together

with the noise are highly polarized. The larger the BER is, the faster the DOP of the signal and noise decreases.

4.3.2 DOP evolution with a high PDL

4.3.2.1 DOP evolution of the signal and the noise with a high PDL

Here, the goal is to determine the PDL in the loop, measure the DOP of the channel as a function of propagation distance and validate the reduced model. Due to the static nature of the loop, the relative orientations of PDL elements remain nearly unchanged during the measurement time, so that it is reasonable to lump all the PDL elements together and consider one round trip of the loop as one lumped PDL element. To estimate the PDL in the system, I first optimized the setting of the polarization controllers in the system to obtain error-free propagation at 20,000 km. I kept the same setting of the polarization controllers and opened the loop to a 107 km straight-line system by bypassing the AO switch and the coupler. The combined PDL of the AO switch and the coupler was about 0.1 dB. Since the fiber pigtails did not contribute to the PDL, this 107 km straight-line gave a reasonable approximation of the PDL level per round trip when the setting of polarization controllers was optimized. I monitored the output optical power of this 107 km straight-line while varying the input polarization state, until it covered the Poincaré sphere evenly. The difference between the maximum power and the minimum power in dB, 0.35 dB, was the estimated PDL level per round trip. I also used the Jones matrix method [49] to determine the PDL in the 107 km link, which yielded the same result. In both measurements, I kept the input power low enough to avoid EDFA saturation. By

measuring the gain compression [32], I estimated that the PDG per amplifier to be 0.05 dB using (2.15).

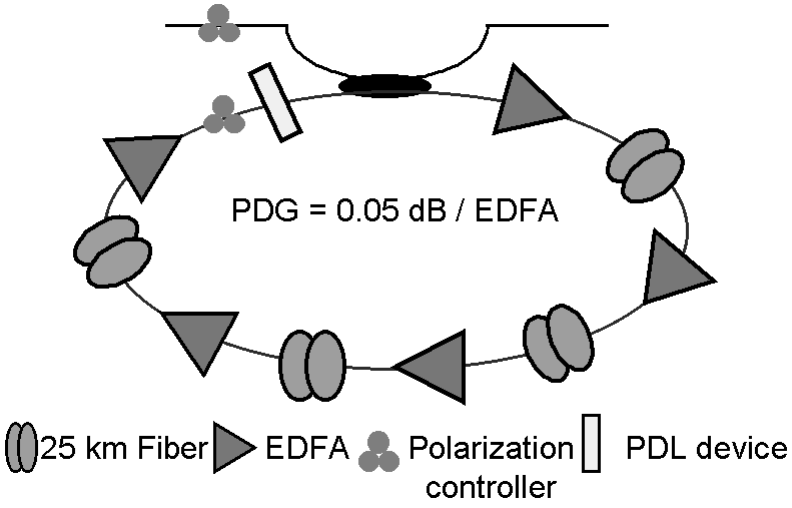

Fig. 4.3. Schematic diagram of the simulation setup.

I also simulated the DOP evolution of the system using the reduced Stokes model discussed in [22]. The loop configuration used in the simulation is shown in Fig. 4.3. The system consists of four 25 km fiber spans. The fiber loss is compensated by four EDFAs and the fifth EDFA is used to compensated the loss of coupler and AO switch. Each EDFA generates the ASE noise, provides PDG and keeps the output optical power as a constant. A lumped PDL element is placed at the end of this loop to simulate the accumulated PDL per round trip and the low loss axis of this PDL element is set to be (1, 0, 0) in Stokes space. In the simulation, I first generated a set of 100 random rotations required by the coarse step method with a step of 1 km for the first round trip. This set of rotations represented the fiber realization and was chosen in such a way that the SOPs after the rotations covered the Poincaré sphere evenly. To account for the periodic nature of the optical path, in the following round trips, the fiber realization was simulated by the same set

of rotations. One extra random rotation was placed in front of the PDL element to simulate the adjustment of the polarization controllers in the experimental loop. While in one Monte Carlo realization, this rotation was fixed for every round trip; for different Monte Carlo realizations this rotation varied randomly. I followed the Stokes parameters of the signal and the noise separately. The DOP was recorded after each round trip. The system performance was evaluated by the *Q*-factor using (3.29) at 20,000 km.

In the Monte Carlo simulation, by adjusting the extra rotation in front of the PDL element, I varied the alignment of the SOP of the signal and the low-loss axis of the PDL element. Therefore the OSNR, as well as the *Q*-factor, at 20,000 km varied accordingly. I used 10,000 random rotations in the Monte Carlo simulations. These rotations were chosen in such a way that for any input polarization states, the output of the rotations covered the Pincaré sphere evenly. The *Q*-factors corresponding to each rotation were recorded, as well as the related DOP evolution. The DOP evolution corresponding to the largest *Q*-factor represented the case where the polarization controllers were set to obtain the lowest BER experimentally. The comparison of the simulated and the experimental DOP evolution for the largest *Q* is shown in Fig. 4.4. as the solid line and the diamonds, respectively. With the PDL to be set as 0.45 dB, the simulated result and the experimental result yields excellent agreement. The 0.1 dB difference of the PDL level between the experiment and the simulation is reasonable, since the AO switch and the coupler were removed during the PDL measurement. The comparison provides the first experimental validation of the reduced Stokes model.

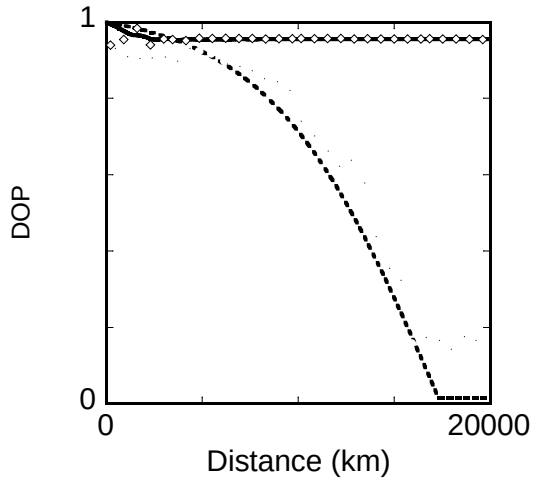

Fig. 4.4. Comparison of the DOP evolution of the signal together with the noise in a loop system as a function of the propagation distance with different PDL level per round trip, when setting of the polarization controller was optimized in the system to obtain the largest *Q* at 20,000 km. The diamonds and the unfilled circles are the measured results when PDL = 0.35 per round trip and PDL = 0.1 dB per round trip, respectively. The solid line and the dotted line are the corresponding simulation results.

The simulation showed that in this case, the signal was well aligned to the low loss axis of the PDL device every round trip and suffered less attenuation. While the noise orthogonal to the signal in Jones space was aligned with the high-loss axis, it suffered more attenuation. In addition, since the EDFAs in the system were operated in saturation regime, keeping the total output a constant, the loss suffered by noise orthogonal to the signal could not be balanced by the gain of the EDFA. Therefore, the noise power decreased, improving the OSNR. In a recirculating loop with significant PDL, when the PC's settings were optimized to obtain the largest *Q*-factor in a long distance, we observed both an increased DOP and OSNR relative to other PC settings.

This result is consistent with the result shown in Fig. 4.2.. However, this behavior is different from what happened in a straight-line system. In a straight-line system, since the rotations between PDL elements are random, it is rare that the SOP of the signal always aligns to the low-loss axis of the PDL elements and thus the noise orthogonal to the signal will not be highly attenuated at long distance. Therefore, the noise remains unpolarized and accumulates along the propagation. As a consequence, the DOP will decrease as a function of distance.

4.3.2.2 DOP evolution of the noise with a high PDL level

The DOP evolution of the noise as a function of propagation distance is more complicated than that of the signal, since the noise is added by each EDFA during the propagation and builds up gradually with the distance. Understanding the evolution of the noise is very important to completely understand the behavior of the loop system. In order to do so, I first optimized the setting of polarization controllers in the system to obtain the lowest BER, which was less than 10^{-9}, at 20,000 km. As discussed in the previous section, this particular setting corresponded to the case that the signal was aligned with the low-loss axes of the PDL elements in the system. Then I turned off the signal of transmitter while leaving the EDFA before the loading AO switch on to generate unpolarized ASE noise. By carefully adjusting the output power of the EDFA, I kept the input optical power loaded into the loop system the same. Therefore, the EDFAs in the loop system kept the same operation parameters as they had when the signal was present. In this way, I only allowed noise to propagate in the system. I sampled the DOP evolution as function of propagation time and show the measured results as diamonds in Fig. 4.5. The DOP in-

creases linearly during the first few of thousands kilometers and the build-up reaches the level of the DOP for the signal plus the noise measured before.

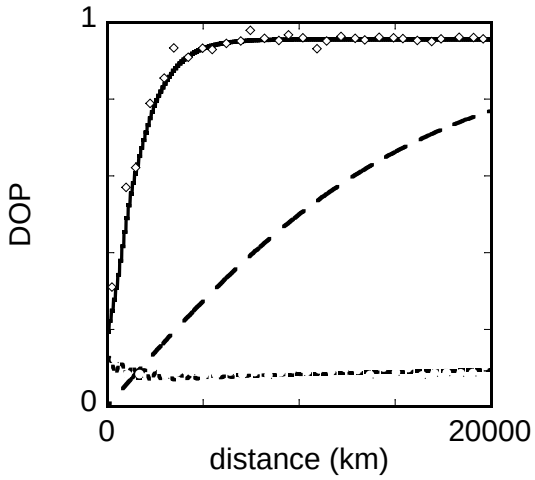

Fig. 4.5. Comparison of the DOP evolution of the noise in a loop system as a function of the propagation distance with different PDL level per round trip, when the setting of the polarization controller is the same as that of in Fig. 4.4. The diamonds and the unfilled circles are the measured results when PDL = 0.35 per round trip and PDL = 0.1 dB per round trip, respectively. The solid line and the dotted line are the corresponding simulation results. The dashed line is the simulated result when the PDG is set to be zero artificially.

In the Monte Carlo simulations, I first propagated both the signal and the noise in the system and randomly varied the extra rotation in front of the PDL element 10,000 times. The extra rotation in front of the PDL element and corresponding *Q*-factor at 20,000 km were recorded. Then I propagated the noise in the system using the extra rotation that yields the largest *Q*-factor and recorded the according DOP evolution of the noise. The simulated result, shown as the solid line in Fig. 4.5, agrees with the experimental result very well. The agreement provides further validation of the reduced Stokes model.

Since the noise aligned to the low-loss axis of the PDL elements suffers less attenuation than noise aligned with the high-loss axis does, the noise starts to repolarize in the direction of the low-loss axis of the PDL elements. At the beginning of the propagation, the DOP is so low that the effect of PDG is effectively eliminated. The linear build-up of DOP is due to the effect of PDL. The slope of the linear build-up is a function of the PDL per round trip. As the DOP increases, the effect of PDG becomes stronger. Since the effect of the PDG is to give excess amplification to the direction orthogonal to the total polarization state in the channel, the attenuation of the noise aligned with the high-loss axis of the PDL elements slows down. Consequently, the DOP evolution does not increase linearly any more and when the effects of the PDL and PDG balance each other, the DOP is a constant along the propagation.

4.3.3 DOP evolution with a smaller PDL

The main sources of PDL in our system are the couplers and isolators in the EDFAs. To reduce the PDL level in the system, I rebuilt the EDFAs by using isolators with PDL < 0.1 dB, enabling the reduction of the PDL level for each EDFA, which reduced the accumulated PDL in the system to be less than 0.1 dB per round trip. I achieved error free transmission at 17,000 km using the newly constructed system. I repeated the experiments and the simulations described before to obtain the DOP evolutions as a function of distance for the signal plus noise and the noise only. The simulated and measured DOP evolutions for the low PDL case are shown in Fig. 4.4 and Fig. 4.5 respectively.

Since the PDL in this system is low, the reduction of the noise orthogonal to the signal is not significant. In addition, the PDG effect provides excess gain to the direction

orthogonal to the polarization state of the entire channel. When the system has a high OSNR to give low BER values, this direction is close to the direction orthogonal to the signal. Since the PDL per round trip is comparable with the PDG, the PDG effect balances the reduction of the noise orthogonal to the signal due to PDL. Hence, the noise builds up in both directions, parallel and orthogonal to the signal and remains unpolarized. Therefore, the OSNR of this system is lower compared to that of the system with high PDL and the DOP evolution decreases as a function of distance. The measured and simulated results are shown as open circles and the dashed-line in Fig. 4.4.

The measured and simulated results of the DOP evolution of the noise only indicate that the noise remains unpolarized along the propagation. The open circles show the experimental results and the dashed-line shows the simulated result in Fig. 4.5. The residual DOP shown in Fig. 4.5 is due to the polarization dependence of the AOs at the loop input, which has 0.6 dB PDL and repolarized the initial unpolarized ASE noise from the transmitter. The measured result does not show any noticeable further repolarization of the noise along the propagation. In the simulation, I accounted for the DOP of the input ASE noise. The result does not show significant change of the DOP along the propagation distance.

In order to isolate the effect of PDL from the effect of PDG, in the simulation of the noise only case, I artificially turned off the PDG. I show the simulated result Fig. 4.5 as a long dashed line. Even with a low PDL per round trip, I found that without PDG, the noise started to repolarize as the propagation distance increaseed when the polarization controllers were optimized to obtain the highest OSNR in the system. If the PDG is not significant compared to the PDL effect, the slope of the DOP build-up of the noise of the

first few of thousand kilometers is a good estimator of the PDL level in the system with the polarization controllers optimized.

I investigated the DOP evolution of the signal with noise and of the noise alone as a function of propagation distance with different PDL levels per round trip when the setting of the polarization controllers in the system was optimized. I compared the measured results to the simulated results from the reduced Stokes model. The excellent agreement between the experimental results and the simulated results validate the reduced Stokes model. The results provide evidence that the DOP evolution, which reflects the evolution of the OSNR, in a recirculating loop is different from what is expected for a straight-line system. In addition the results suggest that in recirculating loop systems, the PDL effect may help to improve system performance when the setting of the polarization controllers in the loops aligns the signal to the PDL low-loss axis every round trip. In this special case, the signal suffers less attenuation, and the noise orthogonal to the signal is reduced by the combined effect of the accumulated PDL and EDFA saturation, yielding a high OSNR. When the PDL level per round trip increases, the reduction of the noise orthogonal to the signal is faster, resulting a higher OSNR at a long distance. This result is consistent with my achievements of error-free propagation up to 20,000 km when PDL = 0.35 dB per round trip, but only 17,000 km of error-free propagation when PDL = 0.1 dB per round trip.

4.4 *Q*-distribution of the recirculating loop

4.4.1 *Q*-factor distribution of a loop with a low PDL

To calculate the outage probability of a transmission system as well as the performance budget, one must know the *Q*-factor distribution. With a low PDL level in the recirculating loop, the DOP of the signal and the noise in a recirculating loop system decreases as a function of the propagation distance. Although the DOP evolution in such a system is similar to that of a straight-line system, whether the *Q*-factor distribution emulates that of a straight line system is still questionable. Since the loop remains static for a long period of time, the signal and noise experience the same polarization rotations for each round trip. When the settings of the PC in the loop system are optimized, the PDL increases linearly as a function of the distance. However, in a straight-line system, due to the randomly varying birefringence, the polarization states orientate randomly along the propagation distance, and the PDL will increase as a square-root of the distance. Therefore, the accumulated PDL will be exaggerated in a loop system. I investigated the system performance by measuring the *Q*-factor distribution with different PC settings and simulated the system performance using the reduced Stokes model. The comparison of the measured result and the simulated result yielded good agreement.

I measured the *Q*-factor, defined in (3.9) at a propagation distance of 5,000 km, when the net PDL in the system was less than 0.1 dB. The *Q*-factor at this propagation distance was obtained using a gated digital sampling scope. The method was described in section 3.2.2. I mechanically varied the first polarization controller in the loop (shown in Fig. 4.1) and then measured the corresponding *Q* value. To obtain a *Q* distribution, I repeated this process until the adjustment of the polarization controller gave an even coverage on

the Poncaré sphere. Except for the polarization controller, the rest of the loop remained in a quasi-static orientation. The measured pdf of the *Q*-factor distribution based on 200 *Q*-factor samples is shown in Fig. 4.6 as histogram bars. Instead of a Gaussian-like distribution that expected in a straight-line system, the *Q* distribution of the loop has double humps.

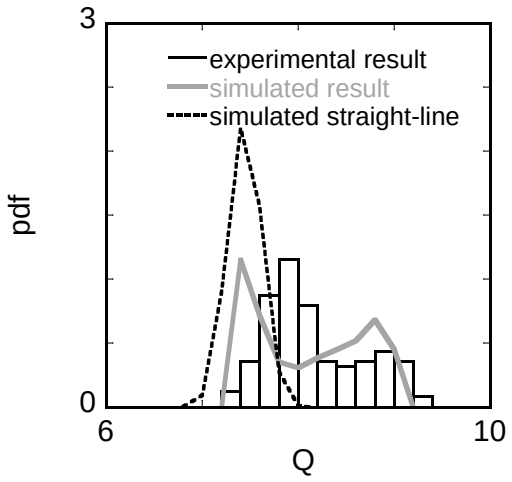

Fig. 4.6. Comparison of the *Q*-factor distribution at 5,000 km when PDL = 0.1 dB per round trip. The histogram is the measured result. The gray solid line is the simulated result using the reduced Stokes model. The dashed-line is the simulated result of a corresponding 5,000 km straight-line system.

To obtain physical insight into this behavior, I used the reduced Stokes model to obtain the numerical pdf of the *Q*-factor distribution using Monte Carlo technique. In the simulation, I placed an extra rotation in front of the PDL element to emulate the adjustment of the polarization controller in the experiment. The extra rotation was the same for every round trip in one Monte Carlo realization. In different Monte Carlo realization, I

chose this rotation randomly so that for any input polarization state, the polarization state would cover the Poncairé sphere evenly after rotations. In every Monte Carlo realization, I followed the Stokes parameters of the signal and the noise separately, and then calculated the OSNR at 5,000 km as $\mathrm{OSNR} = S_0 / S_{0,\mathrm{noise}}$, where S_0 and $S_{0,\mathrm{noise}}$ were the average power of the signal and the noise, respectively. I used Eq. (3.29) to calculate the *Q*-factor. To convert the OSNR to the electrical SNR used in the *Q*-factor calculation, I used an enhancement factor of 3.4 as discussed in Section 3.3. I collected 10,000 *Q*-factor samples at 5,000 km. The simulated result is shown in Fig. 4.6 as a solid gray line. Both the pdf of the simulated result and that of the measured result are double humped.

In order to compare the statistics of the loop performance to that of a straight-line system, I also simulated a 5,000 km straight-line system, using the reduced Stokes model. Four EDFAs with the same characteristics as those in the loop simulation were equally spaced at 25 km to compensate the loss of the fiber. PDL elements with PDL = 0.1 dB were placed every 100 km and the low-loss axis of each PDL element was set to be (1, 0, 0) in Stokes space. To simulate the random orientation of the fiber in the straight-line system, I chose a random rotation for every simulation step, 1 km, along the propagation distance. Each set of rotations corresponds to one fiber realization. I chose 10,000 independent fiber realizations to obtain the *Q*-factor distribution. The *Q*-factor for every fiber realization was calculated using the same formula as that in the loop simulation. I show the result in Fig. 4.6 as a dashed line. The pdf of the *Q*-distribution is Gaussian-like and it is aligned with the low-*Q* portion of the loop result.

In the recirculating loop, due to the periodicity of the optical path, when the polarization controllers in the system are optimized, the signal is well aligned with the low-loss

axis of the PDL element and the noise orthogonal to the signal aligns constantly with high-loss axis of the PDL element. Therefore, the OSNR is artificially improved, so is the *Q*-factor. However, in a straight-line system, due to the random birefringence, the polarization state of the signal orients randomly and rarely aligns with the low-loss axis and the noise orthogonal to the signal can not be attenuated more than the noise parallel to the signal, so that the OSNR is reduced. Consequently, the *Q*-factor is centered at the low-*Q* portion of the loop result. When the polarization controllers are optimized, the loop overestimates the system performance of an analogous straight-line system.

4.4.2 Dependence of the *Q*-factor distribution on fiber realization

My study of the DOP evolution and the *Q*-factor distribution have shown that the periodic nature of the recirculating loop, along with PDL may artificially attenuate the noise orthogonal to the signal, hence improving the OSNR and overestimating the system performance. If the *Q*-factor distribution is well defined, by carefully calibrating the system performance, it is still possible to predict the system performance of a corresponding straight-line system accurately. However, from my study, I observed that one of the difficulties of loop experiments was that the statistics of the *Q*-factor depended not only on the setting of PCs in the system but also on the fiber realizations.

Although, in the laboratory environment the loop system can be static for one or two hours, the fiber realizations still change gradually as a function of time. Changes of the fiber realizations not only change the orientations of the signal and noise, but also lead to variations in the accumulated PDL for each round trip. Therefore, in the experiment the

dependence on the fiber realization is complicated. These effects make it extremely difficult to repeat statistical results that are obtained from the loop experiments.

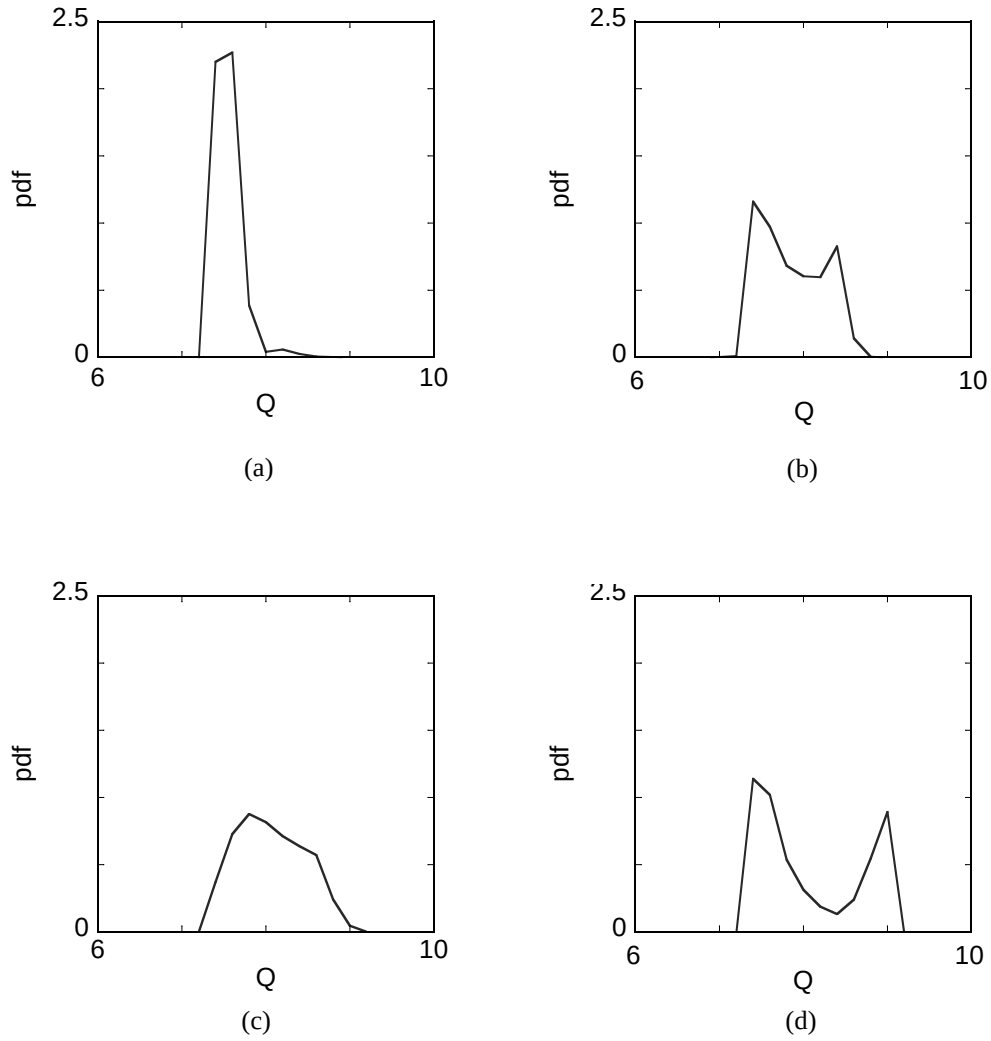

Fig. 4.7. Simulated *Q*-factor distribution at 5,000 km in the loop system with different fiber realizations.

I show a set of simulated results of the *Q*-factor distribution corresponding to the different fiber realizations in Fig. 4.7. In the simulations, in order to simulate the static na-

ture of the loop system, I generated a set of random rotations for the first round trip, and kept the same set of fiber rotations for subsequent round trips. This set of random rotations corresponds to one fiber realization. Once the fiber realization was determined, I employed one extra rotation before the lumped PDL element to simulate the polarization controller adjusted in the experiment and recorded the corresponding *Q*-factor. I chose 10,000 random rotations, so that for a fixed input SOP, the output SOP after the rotation covered the sphere evenly and obtained 10,000 *Q* samples. By choosing different seeds for the random generator, I was able to generate different fiber realizations. As I show in Fig. 4.7, the *Q*-factor distributions are different from one fiber realization to the other. Although the *Q*-factor distributions are not always double-humped, they always have a large *Q* tail.

4.5 Evolution of the polarization states

My study has shown that the periodicity of the optical path along with the PDL element in a loop system can artificially improve the system performance. When the setting of the polarization controllers in the system is optimized, the *Q*-factor distribution of such a system has a large *Q*. The dependence of the *Q*-factor on the setting of polarization controllers in the system indicates that the *Q*-factor is closely correlated with the polarization state evolution. In order to further explain what causes the observed double-humped distributions, I followed the polarization state evolution after each round trip of the loop up to 16,000 km experimentally for three cases— the evolution for the upper end of the *Q* distribution referred as the large *Q* case, the evolution for the lower end of the *Q* distribution referred as the small *Q* case and the evolution for the center of the *Q* distribution re-

ferred as the medium *Q* case. In addition, I simulated the polarization state evolution by following the SOP of the entire channel after each round trip for these three cases. Furthermore, my colleague Dr. Brian Marks and I theoretically explained the polarization state evolution in a loop system [50].

4.5.1 Experimental and simulated results

The measured and simulated results are shown in Fig. 4.8. In order to easily observe the trace of the polarization state evolution, I displayed the trajectories of SOPs on the Poncairé sphere. I used a grey scale to color-code the propagation distance. The variation from black to light gray indicates an increase in the propagation distance. In the large *Q* case shown in Fig. 4.8 (a) and (d), the polarization state on the Poincaré sphere spirals inward to a point and converges quickly. In the small *Q* case, the evolution exhibits outward spirals, as shown in Fig. 4.8(c) and (f). In this case, the measured result shows the SOP evolution up to 10,000 km, in order to maintain reasonable system performance and avoid the measurement error due to poor OSNR. In the simulation, the distance is extended to 10,000 km to make comparison. In the medium *Q* case, the polarization states evolve in a nearly circular trajectory on the sphere, as shown in Fig. 4.8(b) and (e), which converges slowly if at all.

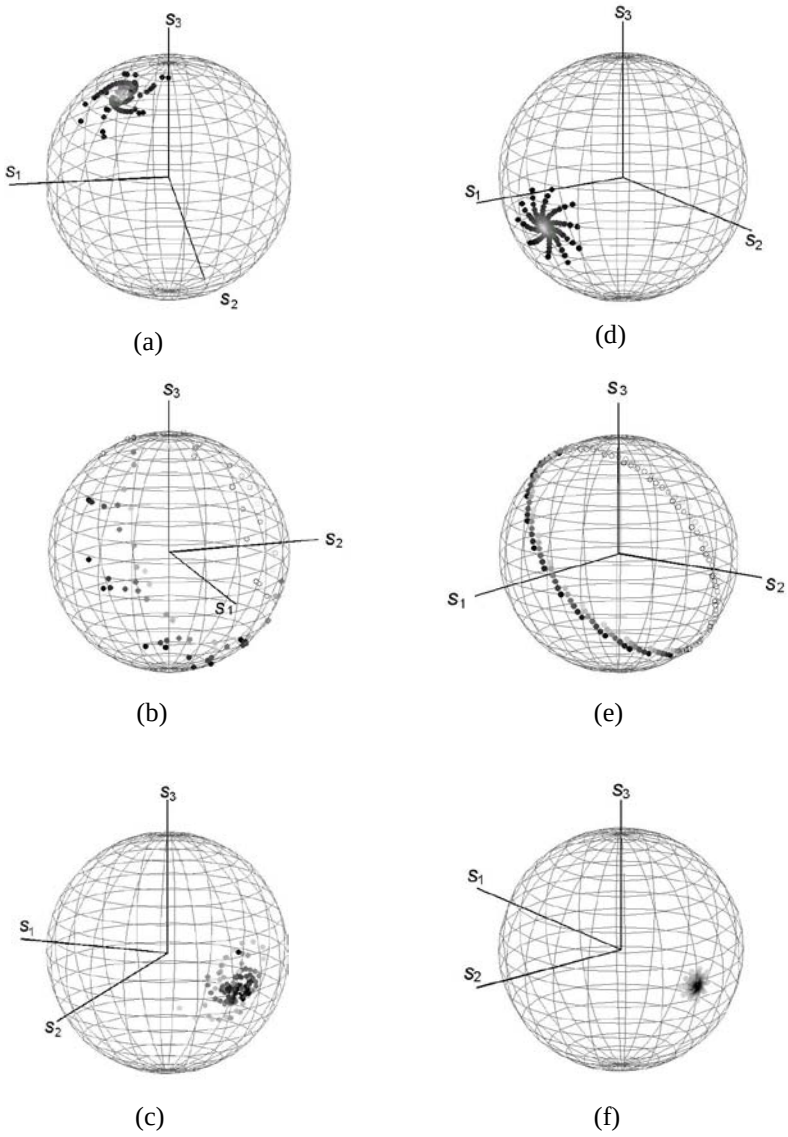

Fig. 4.8. Experimental data and simulated data showing the polarization state evolution in the loop system on the surface of the Poincaré sphere. Fig. 4.8 (a), (b) and (c) are experimental results and Fig. 4.8 (d), (e) and (f) are corresponding simulated results. The unfilled circles indicate points on the far side of the sphere. Figs. 4.8 (a) and (d) correspond to a high *Q* value and show an inward spiral. Figs. 4.8 (b) and (e) correspond to a medium *Q* value and show a circular trajectory around the sphere. Figs. 4.8 (c) and (f) correspond to a low *Q* value and shows an outward spiral. The gray scale from black to light gray indicates increasing propagation distance.

4.5.2 Mathematical analysis

My colleague Dr. Brian Marks and I explained the correlation of the polarization state evolution on the Poincaré sphere to the *Q* value through a simple mathematical analysis. Please see the detailed derivations in Appendix. The transfer matrix of one round trip can be written as

$$\mathbf{M}_{\text{loop}} = \mathbf{M}_{\text{PDL}}\mathbf{M}_{\text{rot}}, \tag{4.1}$$

where $\mathbf{M}_{\text{rot}}$ is a unitary matrix representing a fixed rotation on the Poincaré sphere giving the rotation due to the fiber and the loop's polarization controller, and $\mathbf{M}_{\text{PDL}}$ represents the effect of PDL in one round trip of the loop. Note that in this formulation, we neglected the effects of noise, PDG, and amplifier saturation. Our reduced Stokes model simulations did consider these effects and showed that the predominant effects that altered the polarization state of a signal were the random fiber rotation and the PDL. An arbitrary rotation on the Poincaré sphere could be expressed as a rotation through an angle γ about an axis, which is given by a unit vector $\mathbf{s}_{\text{rot}}$. In this notation, although I chose the low-loss axis of the PDL to be $\mathbf{s}_{\text{PDL}} = (1,0,0)^t$ in Stokes space, the results are general.

The PDL in the system has the effect of causing 100% transmission on one side of the Poincaré sphere while causing loss on the other side. Since the recirculating loop system has a static nature, inherently it is periodic. We may write its transfer matrix after *n* round trips as $\mathbf{T} = \mathbf{M}_{\text{loop}}^n$. Then the output Stokes vector after *n* round trip can be written as

$$\mathbf{s}_{\text{out}} = A_+^n \left|c_+\right|^2 \mathbf{s}_+ + A_-^n \left|c_-\right|^2 \mathbf{s}_- + 2B^n \left|c_+\right|\left|c_-\right|\left[\mathbf{t}_1 \sin(n\gamma + \Delta\psi) - \mathbf{t}_2 \cos(n\gamma + \Delta\psi)\right] + \ldots \tag{4.2}$$

where

$$\mathbf{s}_{\pm} = \pm\mathbf{s}_{\text{rot}} + \tfrac{1}{2}\varepsilon\left[\mathbf{s}_{\text{PDL}} \mp \mathbf{s}_{\text{rot}} + (\mathbf{s}_{\text{rot}} \times \mathbf{s}_{\text{PDL}})\cot\tfrac{\gamma}{2}\right] + O(\varepsilon^2), \tag{4.3}$$

$$\mathbf{t_1} = \left(\mathbf{s}_{\text{rot}} \times \mathbf{s}_{\text{PDL}}\right) \Big/ \left|\mathbf{s}_{\text{rot}} \times \mathbf{s}_{\text{PDL}}\right|, \tag{4.4}$$

and

$$\mathbf{t_2} = \mathbf{s}_{\text{rot}} \times \mathbf{t_1}. \tag{4.5}$$

In these expressions,

$$A_{\pm} = 1 - \varepsilon(1 \mp \mathbf{s}_{\text{rot}} \cdot \mathbf{s}_{\text{PDL}}) + O(\varepsilon^2), \tag{4.6}$$

and

$$B = 1 - \varepsilon + O(\varepsilon^2), \tag{4.7}$$

where ε is a small number less than 1. From (4.2), one can see that the third term contains sinusoidal pieces that corresponds to the spiral or circular motion on the Poincaré sphere and the first two terms provide the spiral center.

If $\mathbf{s}_{\text{rot}}$ is on the same hemisphere as $\mathbf{s}_{\text{PDL}}$ as in Fig. 4.9 (a), we have $0 \le \mathbf{s}_{\text{rot}} \cdot \mathbf{s}_{\text{PDL}} \le 1$, then $A_{+} > B > A_{-}$, and the first term in (4.2) dominates as *n* increases. Consequently the eigenvector $\mathbf{s}_{+}$ is the attracting point, or the center of an inward spiral on the sphere. As *n* increases, also, there is a rotation by the angle γ around the attractor each round trip, as seen in the third term in (4.2). If the input polarization state is close to the attracting eigenstate $\mathbf{s}_{+}$, one observes an inward spiral similar to the high *Q* case in Fig. 4.8 (a) and (d). In this case, the polarization state of the signal spends most of its time on the same hemisphere as the low-loss axis of the PDL, and the signal suffers less attenuation than the noise does, leading to a higher OSNR and the *Q*-factor.

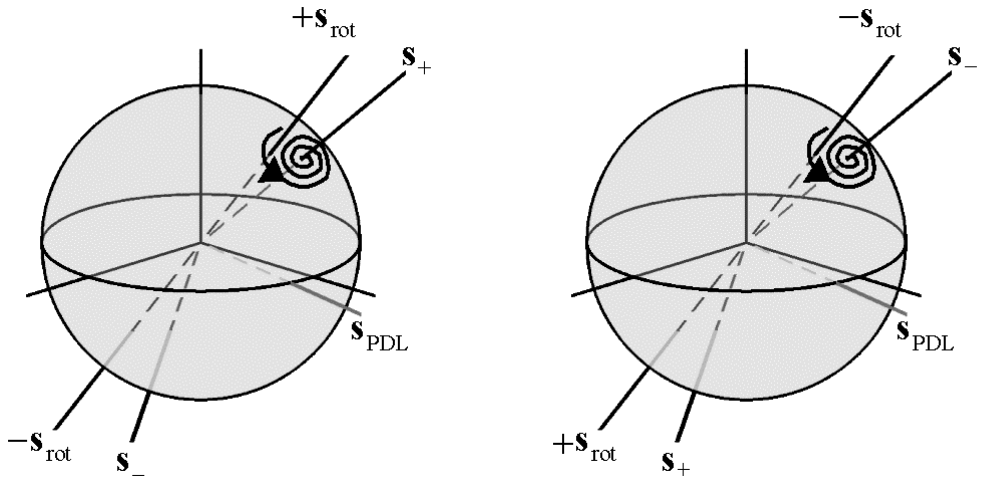

Fig. 4.9. Pictorial description of the spiral behavior on the Poincaré sphere. Without PDL, the eigenstates are $\pm\mathbf{s}_{rot}$, but PDL causes the eigenstates s_+ and s_- to be no longer antiparallel. s_{PDL} is the low-loss axis of the aggregate round-trip PDL, causing the polarization state to spiral toward s_+ or s_-. In Fig. 4.9 (a), $\mathbf{s}_{rot}$ is in the same hemisphere as s_{PDL}, so that s_+ is the attracting eigenstate. In Fig. 4.9 (b), $\mathbf{s}_{rot}$ is in the opposite hemisphere as s_{PDL}, so that s_- is the attracting eigenstate.

Similarly, if the input polarization state is on the opposite side of the sphere from the attracting eigenstate, one observes an outward spiral away from the other eigenstate $\mathbf{s}_-$, which is a repeller. I show the result in the low *Q* case in Figs. 4.8 (c) and (f). The experimental result and the simulated result were obtained for the distance up to 10,000 km in order to remain reasonable OSNR. At distance beyond 10,000 km, we could not obtain a BER less than 10^{-9}, and the DOP of the entire channel was much less than unitary. Therefore it was difficult to accurately measure the polarization state at longer distance. In the simulation, since we traced the polarization state of the signal and the noise separately, we were able to extend the distance up to 20,000 km. The simulated result is shown is

Fig. 4.10, in which the distance is color-coded by the gray scale. The darker color indicates shorter distance. As predicted in the theory, when the input polarization state is close to the high-loss axis of the PDL element, the polarization states are first repelled away from the eigen state of $\mathbf{s}_-$ along the propagation, and one observes an outward spiral. As the distance increases, the polarization states eventually converge to the opposite of the sphere, the same hemisphere as the low-loss axis of the PDL. In this case, the signal's polarization state spends most of its time on the hemisphere of the high-loss axis of the PDL, and the siganl therefore suffers degradation, reducing the OSNR and the *Q*-factor.

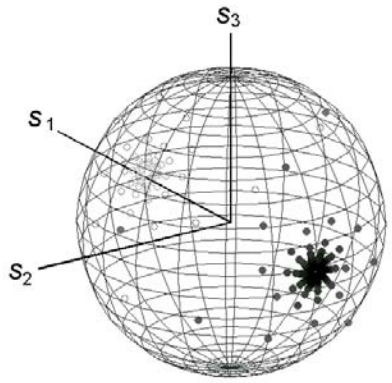

Fig. 4.10. Simulated result of the polarization state evolution up to 20,000 km in the low *Q* case. The loop has an aggregate PDL = 0.1 dB per round trip. The gray scale from black to light gray indicates the increasing propagation distance. The unfilled circles are the points on the far side of the sphere.

If $\mathbf{s}_{\text{rot}}$ is on the hemisphere opposite to $\mathbf{s}_{\text{PDL}}$, so does $\mathbf{s}_+$, as shown in Fig. 4.9 (b), then $A_+ < B < A_-$ and the second term in (4.2) dominates as *n* increases. The spiral is attracted to $\mathbf{s}_-$, which is at the same hemispheres as $\mathbf{s}_{\text{PDL}}$. Consequently, we have similar polarization evolution discussed in Fig 4.9 (a). In the case where $\mathbf{s}_{\text{rot}}$ is orthogonal to

$\mathbf{s}_{PDL}$, all three terms in (4.2) remain equally dominant regardless of the input polarization state. One then obtains a circular trajectory on the Poincaré sphere that does not converge to any particular point. In this case, the signal is aligned with the high-loss axes and the low-loss axes of the PDL elements alternatively, resulting a moderate *Q* factor. In addition, the probability of this case is much lower than those of the other two. Due to the random birefringence of the fiber, the alignment of the signal and the axes of the PDL elements in a straight-line system would be random, as well as the SOP of the signal, so that the spiral behavior is different from what is expected in a straight-line system.

4.5.3 Comparison to a straight-line system

The analysis, as well as the experimental and simulated results, show that the periodicity in the loop leads to interesting polarization evolutions in the system. The periodicity together with the PDL lead to spiral trajectories on the Poincaré sphere and the spirals are always attracted to the eigenstate on the same hemisphere of the low-loss axis of PDL element. Thus for a particular setting of the polarization controllers that aligns the SOP of the signal to the low-loss axis of the PDL element, the recirculating loop can artificially enhance performance even when the PDL level per round trip is low. To compare the polarization state evolution of a loop system to that of a straight-line system, I performed a simulation of a straight-line system in which I applied the same parameters as in the loop simulation including the characteristics of the EDFA, the EDFA spacing, the fiber loss, the input power and the receiver characteristics. In the straight-line simulation, I placed a PDL element every 100 km and I set the low-loss axis of PDL elements to be (1, 0, 0) in the Stokes space. Unlike the loop system, where the fiber realization is periodic, I

randomly chose rotations for every simulation step along the propagation. A set of these random rotations was considered as one fiber realization. For both loop simulation and the straight-line simulation, each PDL element had a level of 0.1 dB. The *Q*-factor was calculated at the end of transmission. Since the polarization state evolution depends on both the input polarization state of the signal and the fiber realization, I compared the loop system and the straight-line system by simulating two cases. In the first case, I fixed the input polarization state and varied the fiber rotations in the system. In the second case, I fixed the fiber realization and varied the input polarization state so that the input polarization states covered the Poincaré sphere evenly. This case was equivalent to a system with input scrambling.

In the first case, one set of fiber rotations was chosen for every round trip as one fiber realization and the fiber realizations for different Monte Carlo simulations were chosen randomly in the loop simulation. In contrast, in the straight-line simulation, the fiber rotations were chosen randomly along the propagation distance as one fiber realization. In the comparison, I chose 1,000 fiber realizations independently with the input polarization fixed at (1, 0, 0) and the low-loss axis of the PDL element was fixed at (1, 0, 0) for both simulations. I recorded the polarization states after each round trip for every fiber realization. The *Q*-factor was calculated for each fiber realization at 16,000 km. The polarization state for each fiber realization at 100 km, 8,000 km and 16,000 km are shown in Fig. 4.11. I used gray scale to code different fiber realizations based on the *Q*-factor at 16,000 km. The darker the color is, the smaller the *Q*-factor is at 16,000 km. In the loop system, although the polarization states for different fiber realizations at 100 km cover the Poincaré sphere uniformly, the uniformity is not maintained with propagation. After

16,000 km, the polarization states for the fiber realizations with lighter color, which generate larger *Q*-factors, are attracted to the low-loss axis of the PDL. This result is consistent with our analysis. Since the input SOP is the close to the low-loss axis of the PDL element, if the rotation axis of the fiber $\mathbf{s}_{\text{rot}}$ is close to the PDL low-loss axis as shown in Fig. 4.9 (a), the polariztion state evolution converges very quickly, yielding larger *Q*. On the other hand, the fiber rotations that make the polarization states converge slowly yield smaller *Q*. In contrast, in the straight-line system simulation, the polarization states for different fiber realizations cover the Poincaré sphere evenly regardless of the propagation distance. Furthermore, in the straight-line system, most polarization states are color-coded by darker gray, which indicates a smaller *Q*-factor at 16,000 km. This simulation shows that in the straight-line system, the variation of the *Q*-factor distribution is smaller than in the loop system and is aligned to the low *Q* portion of the *Q*-factor distribution of a loop system.

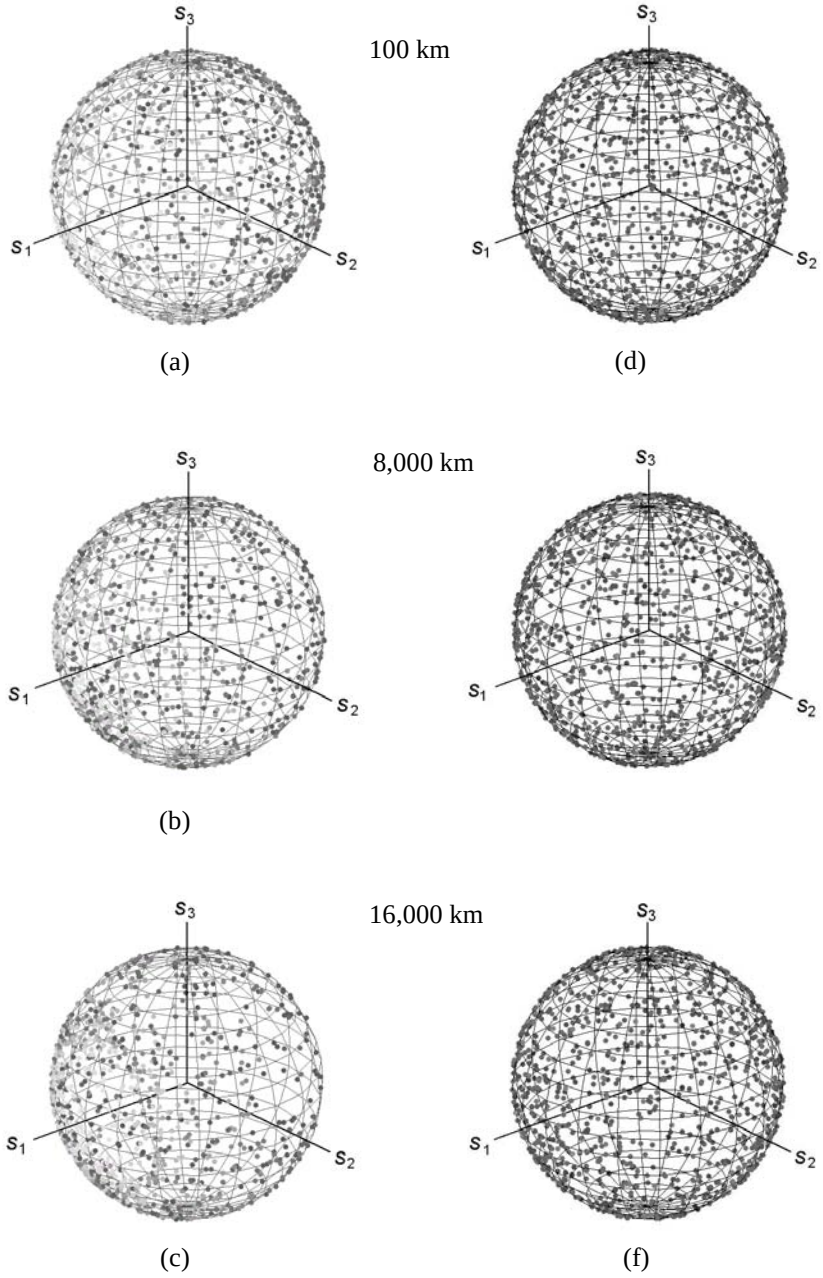

Fig. 4.11. Comparison of simulated polarization state distribution of a loop system to a corresponding straight-line system using the reduced Stokes model when the input polarization state is fixed but the fiber realization is varied. Sub-figures (a), (b) and (c) show the polarization state distribution of the loop system at 100 km, 8,000 km and 16,000 km, respectively. Sub-figures (d), (e) and (f) show the polarization state distribution of the straight-line system at 100 km, 8,000 km and 16,000 km, respectively. The gray scale from black to light gray indicates the increasing of the *Q*-factor calculated at 16, 000 km.

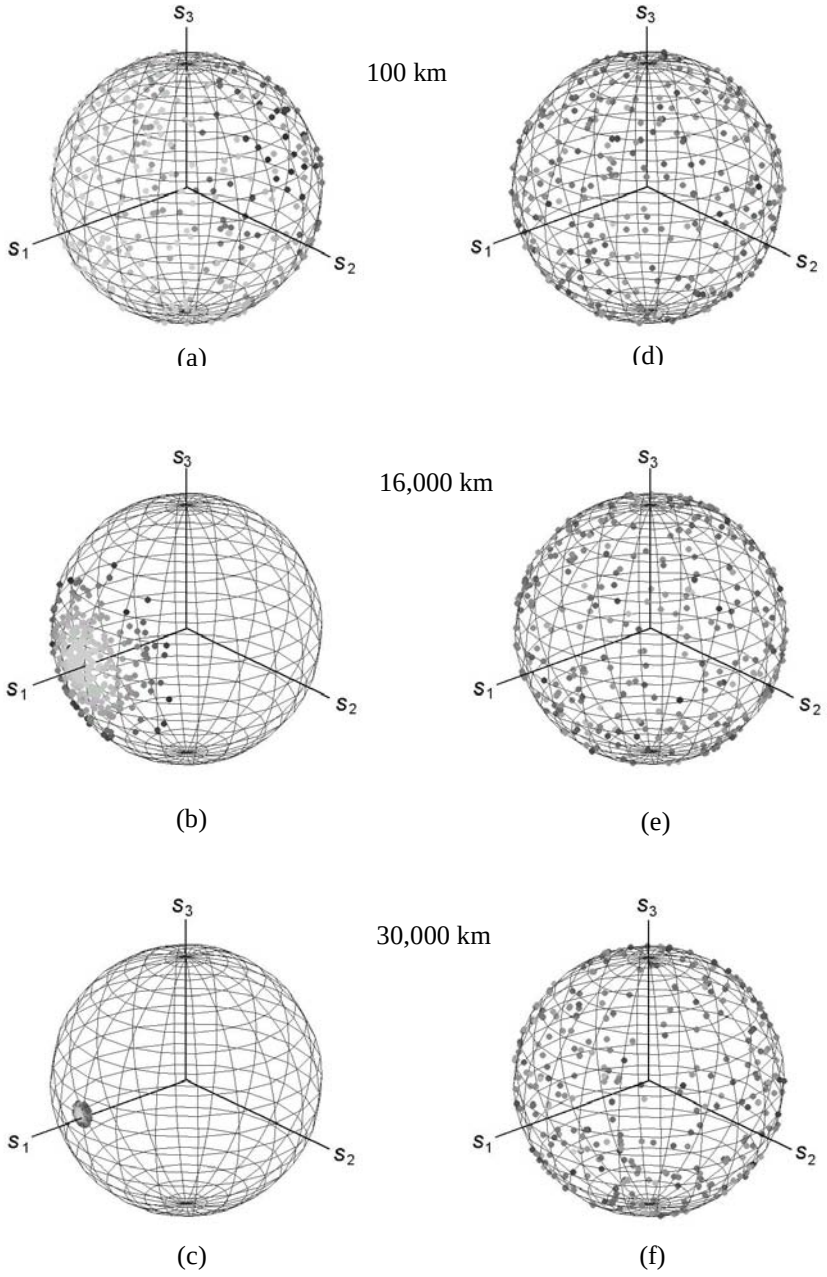

Figure 4.12. Comparison of simulated polarization state distribution of a loop system to a corresponding straight-line system using the reduced Stokes model when the fiber realization is fixed but the input polarization state is varied. Figure (a), (b) and (c) show the polarization state distribution of the loop system at 100 km, 16,000 km and 30,000 km, respectively. Figure (d), (e) and (f) show the polarization state distribution of the straight-line system at 100 km, 16,000 km and 30,000 km, respectively. The gray scale from black to light gray indicates the increasing of the *Q*-factor calculated at 30, 000 km.

In modern DWDM systems with a large channel-count, the PMD effect causes channels to walk-off from each other, reducing the PDG effect [33] and [53]. In a single channel system, input scrambling has proved to be an efficient way to reduce the effect of PDG. It is important to understand the behavior of a loop and a straight-line system with input scrambling. In the second case, I chose the fiber realization that yields the largest *Q*-factor in both systems when the input SOP is (1, 0, 0) and I randomly selected the input SOP to cover the Poincaré sphere evenly to mimic the polarization scrambling at the input. Furthermore, since the noise can be treated as depolarized signal, this investigation helps one to understand the noise behavior in the system. In both simulations, I set the PDG to be 0.

In both simulations, I chose 300 randomly selected input polarization states so that they covered the Poincaré sphere evenly. I followed the polarization evolution corresponding to each input polarization state separately up to 30,000 km. I color-coded each polarization state evolution using a gray scale to indicate the *Q*-factor after the propagation. The lighter the color is, the larger *Q*-factor is. I show the results in Fig. 4.12. In a loop system, the input polarization state at the same hemisphere as the low-loss axis of the PDL tend to obtain better system performance, indicated by a *Q*-factor with lighter color. After propagation, all output polarization states center at the low-loss axis of the PDL element. This behavior indicates that even with low PDL per round trip, the initially depolarized signal and the noise in the loop system may repolarize quickly. On the other hand, the polarization state evolves randomly for all the input polarization states in the straight-line system.

4.6 The *Q*-factor distribution of a scrambled loop

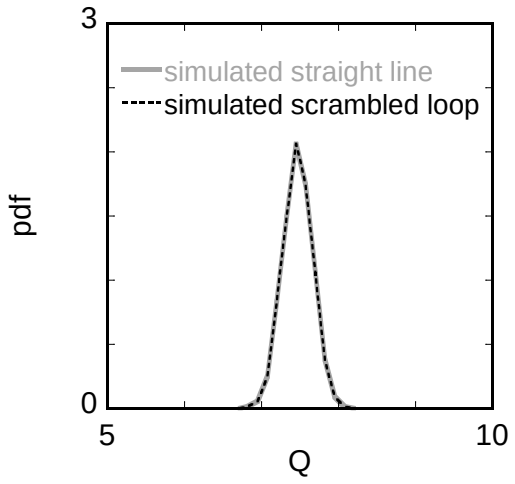

Fig. 4.13. Comparison of the simulated *Q*-factor distribution of the loop-synchronous scrambled loop system (the dashed line) to that of the corresponding straight-line system (the solid grey line) at 5,000 km.

My study shows that the periodicity of the optical path and the PDL elements in a loop system may artificially improve the system performance by attenuating the noise that is constantly aligned with the high-loss axis of the PDL element. Therefore, if one is interested in using a recirculating loop to emulate a straight-line system, one must break this periodicity. One way to do so is to use loop-synchronous scrambling to rotate the polarization state of the signal once each round trip. Simulations have shown that the polarization state remains really random along the propagation when this scrambling was employed. A simulated comparison of the *Q*-factor distribution at 5,000 km for a scrambled loop system with PDL = 0.1 dB per round trip and a corresponding straight-ling system is shown in Fig. 4.13. The solid gray line is the result of

the straight-line system and the dashed-line is the result of the scrambled loop system. The *Q*-factor distribution of the scrambled loop resembles that of a straight-line system.

4.7 Conclusions

I systematically investigated the DOP evolution of the signal and the noise, the *Q*-factor distribution and the polarization state evolution in recirculating loop systems by comparison of the experimental results and the numerical simulations, as well as theoretical analysis. I show that the behavior of a loop system with PDL is different from that of a straight-line system due to the periodicity of the optical path and the presence of the PDL. The loop systems often overestimate the system performance of straight-line systems and the polarization states form spiral evolutions, which are closely related to the system performance. The excellent agreement of the experimental results and the numerical simulations provides the first experimental validation of the reduced Stokes model. My work also suggests that in order to accurately emulate the behavior of the straight-line system, one must break the periodicity of the optical path in the loop system. One way to achieve this is to introduce one random rotation every round trip. This technique is called loop-synchronous scrambling.

Chapter 5

Emulation of straight-line systems using recirculating loops

5.1 Introduction

Recirculating loops have proved to be an efficient experimental model in studying of long-haul transmission systems. However, due to the periodic optical path, recirculating loops do not reproduce the polarization evolutions in straight-line systems [50] and [54] and can overestimate the system performance [37].

One straightforward way to overcome these limitations is to introduce random rotations in the loop system to break the periodicity of the system. The simulation result discussed in Section 4.6 shows that an extra random rotation in each round trip, which transforms any input SOP to cover the sphere evenly, will achieve this goal. However, to apply this concept experimentally is not easy. In general, both BER and *Q*-factor measurements are time consuming. If the fiber realization changes constantly during the measurement, one samples dif-

ferent fiber realizations in one *Q* or BER measurement. Therefore, we need an experimental approach to synchronize the change of fiber realizations to the BER/*Q*-factor measurements.

To break the loop periodicity and to ensure that a measured *Q*-factor or BER corresponds to one fiber realization, I used a loop-synchronous scrambler to emulate a straight-line system [38]. This loop-synchronous scrambler provides a set of random rotations for the loop system and randomly rotates once on each round trip. This set of random rotations is repeated during one sample of the BER or the *Q*-factor measurements. To build up the statistics of the system performance, multiple sets of rotations are chosen randomly. Therefore a recirculating loop system can reproduce the statistical characteristics of a straight-line system. Moreover, I am able to accurately measure the BER or the *Q*-factor for each fiber realization. Since the system that I studied is a single channel system, PDG significantly affects the performance of the system. Modern WDM systems have a large channel count and effectively eliminate PDG. Thus, I employed a second scrambler at the transmitter to eliminate the effect of PDG.

To assess the system performance and to develop system models require the accurate characterization of *Q*-factor distributions in transmission systems. Since lightwave systems with optical amplifiers are vulnerable to the degradation due to polarization-dependent loss (PDL), it is very important to study the statistical behavior of the system performance due to PDL. However, the relationship of the OSNR and the *Q*-factor is not straightforward. As I showed in Chapter 3, when the noise is partially polarized, the correlation of SNR and *Q*-factor is not unique and depends on the DOP of the noise and the SOP of both signal and noise. Therefore the statistics of OSNR does not give a complete picture of the statistics of the *Q*-factor. In my work, I investigated, both theoretically and

experimentally, the system performance of a recirculating loop system with the loop-synchronous scrambler and without the loop-synchronous scrambler corresponding to different PDL levels. I obtain excellent agreement between measured results and numerical simulations, which correctly takes into account the polarized noise in a system with PDL. Both the loop-synchronous scrambling technique and the receiver model discussed in Chapter 3 should prove valuable in assessing realistic system performance.

To obtain repeatable results in the loop system is very important when investigating the system performance and estimating the outage probability. Although the optical path of the loop system remains stable for hours, it changes gradually with time. The slow drift of the optical path not only changes the fiber realization but also varies the accumulated PDL level in the system. Controlling the PDL level in the loop experiment is very critical to achieve the repeatability of the experiments.

Furthermore, the residual PDL in the system converts the polarization modulation at the transmitter to the amplitude modulation. This undesired amplitude modulation coupled with the dynamic response of the EDFA may degrade the system performance, not only canceling out the improvement due to the reduction of PDG effect but also to introduce a larger variation of system performance.

In this chapter, I address these issues in the loop experiments. I describe in detail the PDL control and monitor techniques used in my study, as well as the correlation of the dynamic gain of the EDFA to the scrambling rate of the input scrambler, when the PDL in the system is not negligible. The content of this chapter is organized as following. I first describe a $LiNbO_3$ polarization controller and the experimental setup. I then discuss the approach that I used to monitor the PDL in the system and to obtain repeatable statis-

tical results, followed by the discussion of the input scrambling technique and the effect of EDFA transients. Finally, I compare the experimental results to the simulated results of a scrambled loop system with different PDL values. I also compare the *Q*-factor distribution with and without the input scrambling of a scrambled loop system.

5.2 Setup of loop system

Based on the loop system that I used to investigate the polarization behaviors and the system performance, discussed in Chapter 4, I added a $LiNbO_3$ polarization controller at the end of the loop. This controller was controlled by a programmable waveform generator to provide rotations for each round trip. In this dispersion-managed soliton (DMS) system I propagated 10 Gb/s return-to-zero (RZ) pulses modulated by a 2^{15} –1 PRBS pattern over distances of 18,000 km. Fig. 5.1 shows a schematic diagram of the recirculating loop used in experiments [38]. Three mechanically adjustable polarization controllers are placed in the loop system to adjust the PDL level per round trip. In order to eliminate the PDG effect in the system, a polarization scrambler is placed after the transmitter. I will discuss in detail how to choose the scrambling rate of the input scrambler in Section 5.5. The PMD of the fiber is negligible. The PDL varies from 0.13 to 0.6 dB per round trip.

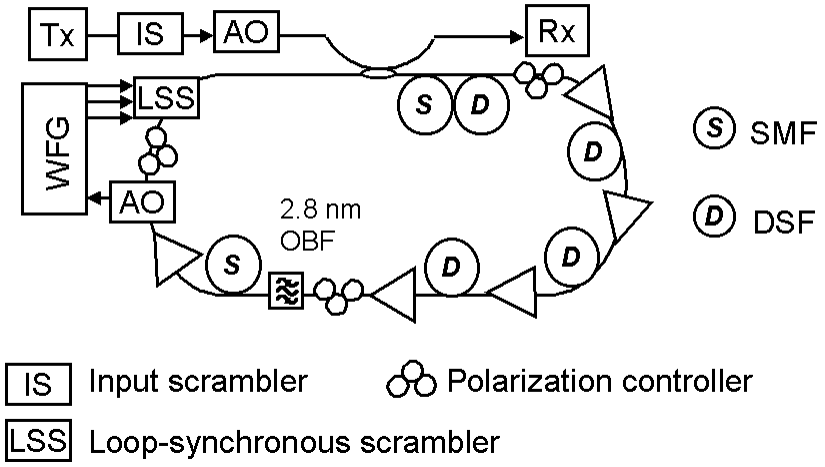

Fig. 5.1. Diagram of the recirculating loop with a loop-synchronous scrambler.

5.3 Loop-synchronous scrambling technique

5.3.1 Principle of loop-synchronous scrambler

Fig. 5. 2 shows a schematic diagram of a compact integrated-optic polarization controller [56]. A standard titanium-indiffused single-mode waveguide is fabricated on low birefringence *x*-cut, *z*-propagation $LiNbO_3$. It includes three cascaded electrode sections, which are equivalent to three waveplates that rotate. The particular construction shown in Fig. 5.2 is a combination of a quarter waveplate (QWP), a half waveplate (HWP) and another QWP. Three pairs of voltages are applied to each electrode section separately to control the phase retardation and the rotation.

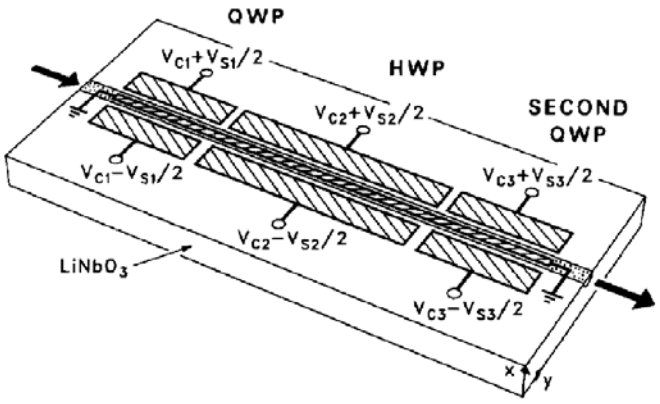

Fig. 5.2. Schematic diagram of a compact integrated-optic polarization controller configured as a combination of QWP-HWP-QWP

The electrical fields that are at the x direction and y direction, shown in Fig. 5.2 are TE and TM modes, respectively. The differential TE-TM phase shift is generated via the linear electro-optic effect by applying a voltage V_S to induce an electric field E_y in the waveguide parallel to the crystal surface. The linear electrooptical effect is the change in index that is caused by and is proportional to the applied electrical field [57]. This field generates an anisotropic optical index change in the waveguide via the linear electro-optic coefficients γ_{12} and γ_{22}, which have values of $\gamma_{12} = -\gamma_{22} \approx 3.4\times10^{-12}$ m/V. The optical phases of TE- and TM-mode shift symmetrically at the same rate in opposite directions. The total TE-TM phase retardation in an electrode section of length L is given by

$$\Phi_y(t) = \Gamma_y \frac{2\pi}{\lambda_0} n_0^3 \gamma_{12} L E_y, \tag{5.1}$$

$$E_y = \frac{V_s(t)}{G_y}, \tag{5.2}$$

where Γ_y is the spatial overlap of the induced electric field with the optical fields along y direction, G_y is the width across the two outer electrodes. The parameter n_0, which is

equal to 2.21, is the ordinary index of refraction and λ_0 is the wavelength in free space. When $\Phi_y(t) = \pi$, $V_S(t) = V$.

Similarly, the common voltage on both sides of the waveguide V_C, which induces an electric field E_x in the waveguide perpendicular to the surface, generates a relative phase shift between the linearly polarized modes at 45° and – 45° via the γ_{61} linear electro-optic coefficient. The total 45° linear phase retardation generated in an electrode section of length L is given by

$$\Phi_x(t) = \Gamma_x \frac{2\pi}{\lambda_0} n_0^3 \gamma_{61} L E_x \tag{5.3}$$

$$E_x = \frac{V_c(t)}{G}, \tag{5.4}$$

where Γ_x is the spatial overlap of the induced electric field with the optic fields, $\gamma_{61} = \gamma_{12} \approx 3.4 \times 10^{-12}$ m/V and G is the width of the gap between the center electrode and one outer electrodes. When the applied voltage $V_{C\pi}(t) = V'$, $\Phi(t) = \pi$.

Without an applied electrical field, the index ellipsoid of a crystal can be written as

$$\frac{x^2}{n_o} + \frac{y^2}{n_o} + \frac{z^2}{n_e} = 1, \tag{5.5}$$

where the directions x, y, z are the principal dielectric axes and the indices n_o and n_e are for ordinary and extraordinary rays, respectively. With the presence of an electric field, the index ellipsoid can be written as

$$\left(\frac{1}{n^2}\right)_1 x^2 + \left(\frac{1}{n^2}\right)_2 y^2 + \left(\frac{1}{n^2}\right)_3 z^2 + 2\left(\frac{1}{n^2}\right)_4 yz + 2\left(\frac{1}{n^2}\right)_5 xz + 2\left(\frac{1}{n^2}\right)_6 xy = 1. \tag{5.6}$$

The change in the coefficients due to an arbitrary electric field can be calculated from the electrooptic tensor r_{ij} as [57]

$$\Delta\left(\frac{1}{n^2}\right)_i = \sum_{j=1}^{3} r_{ij} E_j \,, \tag{5.7}$$

where E_j , j = 1, 2 and 3 are the electrical field in *x*, *y* and *z* directions, respectively. When electrical fields at x and y direction are applied to an *x*-cut and *z*-propagation $LiNbO_3$ as in Fig. 5.2, the index ellipse at x-y plane is written as

$$\left(\frac{1}{n_o^2} + r_{12}E_y\right)x^2 + \left(\frac{1}{n_o^2} - r_{12}E_y\right)y^2 + 2r_{61}E_x xy = 1. \tag{5.8}$$

By finding a new coordinate system — $x'$and y' , the mixed term in (5.8) is eliminated. The new coordinates — $x'$and y' satisfies

$$x' = \cos\theta\, x + \sin\theta\, y \tag{5.9}$$

and [57]

$$y' = -\sin\theta\, x + \cos\theta\, y \,, \tag{5.10}$$

where

$$\theta = \mathrm{ctg}^{-1}\left(\frac{r_{61}E_x}{r_{21}E_y - \sqrt{\left(r_{61}E_x\right)^2 + \left(r_{21}E_y\right)^2}}\right). \tag{5.11}$$

Hence the index ellipse can be written as

$$\left(\frac{1}{n_o^2} + \sqrt{\left(r_{61}E_x\right)^2 + \left(r_{12}E_y\right)^2}\right)x'^2 + \left(\frac{1}{n_o^2} - \sqrt{\left(r_{61}E_x\right)^2 + \left(r_{12}E_y\right)^2}\right)y'^2 = 1. \tag{5.12}$$

Since $\sqrt{\left(r_{61}E_x\right)^2 + \left(r_{12}E_y\right)^2} \ll n_o^{-2}$, I have

$$n_{x'} = n_o + \frac{n_o^3\sqrt{\left(r_{61}E_x\right)^2 + \left(r_{12}E_y\right)^2}}{2}; \tag{5.13}$$

$$n_{y'} = n_o - \frac{n_o^3 \sqrt{\left(r_{61}E_x\right)^2 + \left(r_{12}E_y\right)^2}}{2\sqrt{\quad}}, \tag{5.14}$$

$$\Delta n = n_{x'} - n_{y'} = n_o^3 \sqrt{\left(r_{61}E_x\right)^2 + \left(r_{12}E_y\right)^2}\,. \tag{5.15}$$

Thus, substituting (5.2) and (5.4) into (5.12) – (5.14), one finds that it is possible to keep a fixed relative phase between the electric fields in the direction of new coordinate — $x'$and y' — and to rotate the new coordinates continuously [56]. For example, one introduces a pair of voltage, $V_C \pm V_S/2$ and the voltages V_S and V_C are described as $V_S = V_\pi \sin\Omega t$ and $V_C = V_\pi^{'} \cos\Omega t$, where Ω is the angular frequency. Then the relative phase between the electric fields in the direction $x'$and y' is π and the coordinates $x'$and y' rotate continuously at a constant angular velocity $\Omega/2$ in Jones space. As a result, the device acts as a rotating HWP. Similarly, for voltage amplitudes $V_{\pi/2}$ and $V_{\pi/2}^{'}$, the device acts as a rotating QWP. One can achieve complete conversion between TE and TM mode if the propagation constants of the TE- and TM-modes are exactly equal. However, a small amount of static birefringence always exists in the material. An additional bias voltage V_T is needed to compensate the residual waveguide birefringence by introducing an exactly opposite amount of birefringence $-\Delta n = \Gamma_y n_0^3 \gamma_{12} V_T / G_y$, where Γ_y is the spatial overlap of the induced electric field with the optic fields along y direction and G_y is the width across the two outer electrodes [57].

A combination of QWP-HWP-QWP, in which each section rotates at different angular frequency, forms a triple-stage polarization scrambler that is independent from the

input polarization states [56], [58]. The first QWP, rotating at a constant angular frequency Ω_1, is driven by the voltages

$$V_{1,2\pi/2} = V'_{\pi/2} \sin(2\Omega t) \pm (V_{\pi/2}/2)\cos(2\Omega t) \pm V_{\pi/2}/2 \tag{5.16}$$

where $V'_{\pi/2}$ and $V_{\pi/2}$ is the voltage for inducing phase shift of $\pi/2$ at *x* direction and *y* direction, respectively. The HWP, rotating at a constant angular velocity Ω_2, is driven by the voltages

$$V_{3,4\pi} = V' \sin(2\Omega t) \pm (V_{\pi/2}/2)\cos(2\Omega t) \pm V_{\pi/2}/2 . \tag{5.17}$$

The second QWP, rotating at a constant angular velocity Ω_3, is driven by the voltages

$$V_{5,6\pi/2} = V'_{\pi/2} \sin(2\Omega t) \pm (V_{\pi/2}/2)\cos(2\Omega t) \pm V_{\pi/2}/2 . \tag{5.18}$$

I used an polarization controller, which is made from JDS Uniphase Corp. and has a rise time of 100 ns. This controller consists with eight 1/8 waveplates. Two of the concatenated 1/8 waveplates form a QWP and four of concatenated 1/8 waveplates form a HWP, so that the controller forms a triple-stage QWP-HWP-QWP polarization scrambler. Six voltages are applied to the device to control the rotation. For the particular device that I used in the experiments, as specified in the data sheet, the triple-stage construction is driven by six voltages as followings:

$$V_1 = 12.0\sin(\alpha) - 13.4\cos(\alpha) + 2.6 ; \tag{5.19}$$

$$V_2 = 12.0\sin(\alpha) + 13.4\cos(\alpha) - 2.6 ; \tag{5.20}$$

$$V_3 = 11.1\sin(\beta) - 13.1\cos(\beta) + 5.6 ; \tag{5.21}$$

$$V_4 = 11.1\sin(\beta) + 13.1\cos(\beta) - 5.6 ; \tag{5.22}$$

$$V_5 = 11.7\sin(\gamma) - 13.4\cos(\gamma) + 0.7 ; \tag{5.23}$$

$$V_6 = 11.7\sin(\gamma) + 13.4\cos(\gamma) - 0.7\,. \tag{5.24}$$

The angles $\alpha/2, \beta/2$ and $\gamma/2$ are the rotation angles of these three wave plates. By carefully generating a sequence of six voltages, I am able to generate a set of rotations to cover the Poincaré sphere evenly. This set of rotations is repeatable by applying the same sequence of voltages.

5.3.2 Loop-synchronous scrambling technique

In practical devices, due to the lateral misalignment of the electrode pattern with respect to the waveguide, the voltages V_C and the voltages V_S may introduce some undesired TE-TM mode conversion. The cross modulation can be compensated by adjusting V_C and V_S [58].

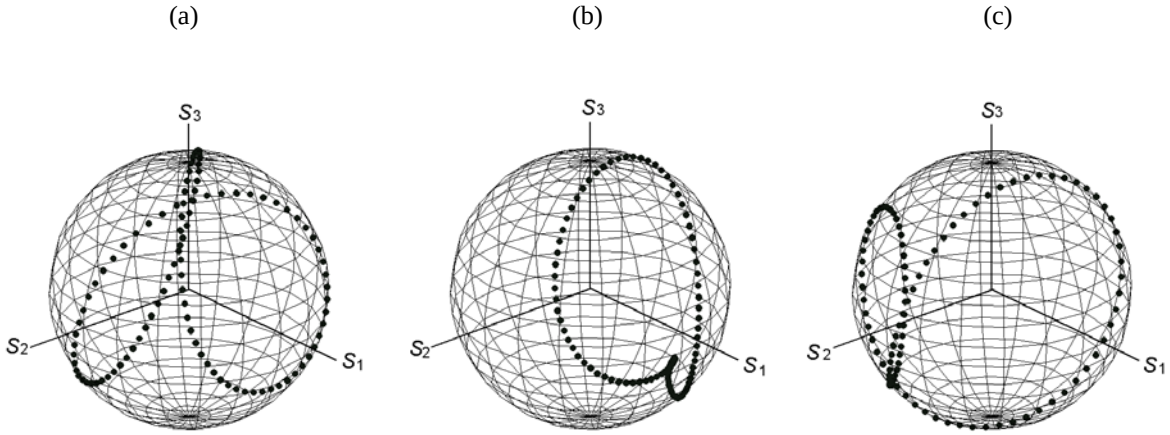

Fig. 5.3. Examples of output polarization states by rotating the HWP only with 100 equally spaced angles from 0 to 2π with three different input polarization states.

Fig. 5.3 shows the output of SOP of the device corresponding to three different input polarization states by rotating only the second waveplate, the HWP. The non-circular output is mainly due to the uncompensated static birefringence between the 1/8

waveplates. However, when the rotation angles of the three waveplate α, β and γ are uniformly distributed from 0 to 2π, for a fixed input polarization state, the output SOPs cover the Poincaré sphere reasonably well, as shown in Fig. 5.4, for which 1,000 output SOPs are sampled. The open circles indicate the output on the back side of the sphere. The corresponding normalized Stokes parameters — s_1, s_2 and s_3, which are shown in Fig. 5.4 (b), (c) and (d) as histograms, are uniformly distributed from –1 to 1, respectively.

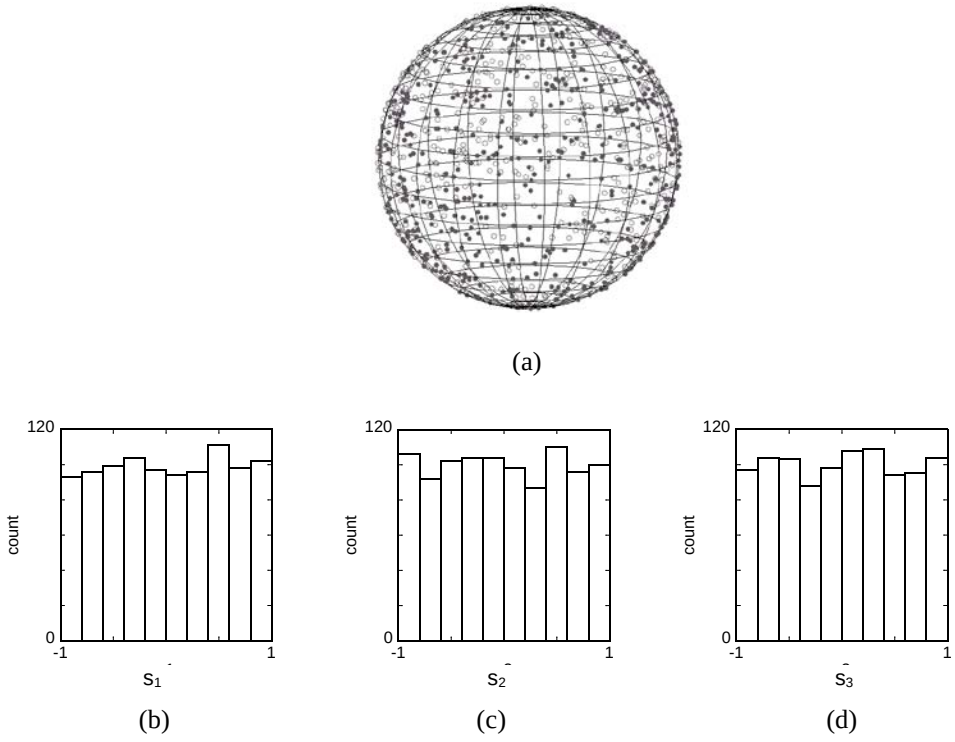

Fig. 5.4. Output polarization states when the waveplate angles are chosen randomly with 1,000 samples. The dots are the polarization state on the front hemisphere and the open circles are the polarization state on the back of the hemisphere. Sub-figures (b), (c) and (d) show histograms of the corresponding normalized Stokes parameters — s_1, s_2 and s_3, respectively.

To achieve the loop-synchronous scrambling, I first generate a set of random angles α, β and γ, which are uniformly distributed from 0 to 2π, and I then use (5.19) to (5.24) to generate a series of six voltages. This series of six voltages is triggered by the control signal of the AO switch. To guarantee that the polarization rotation is randomly changed for each round trip, the sampling period for these six voltages is set to be the round trip time of the loop system, which is 0.54 ms. As an example, in Fig. 5.5, I show a set of measured polarization states as a function of round trip number when the loop-synchronous scrambler is on. Fig. 5.5 (a), (b) and (c) are measured results of the normalized Stokes parameter — s_1, s_2 and s_3 — as a function of round trip numbers, respectively.

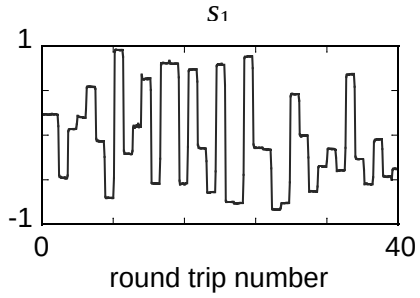

(a)

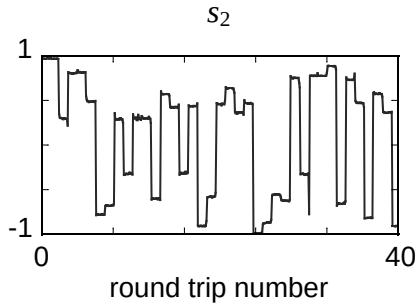

(b)

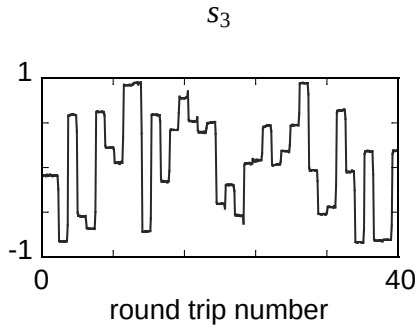

(c)

Fig. 5.5. Measured results of the normalized Stokes parameter — s_1, s_2 and s_3 — as a function of round trip numbers, respectively.

5.4 PDL level control and monitoring

5.4.1 PDL level control

One of the difficulties in the loop experiment is that the statistical behavior of the system performance is difficult to repeat. It depends on the fiber realization and the accumulated PDL. Practically, to maintain the fiber realization in the system is impossible. Moreover, after applying the loop-synchronous scrambling technique, the fiber realization will change randomly, so that all possible fiber realizations will be covered. Therefore, to control the PDL level in the system is very important to obtain a repeatable *Q*-factor distribution of a scrambled loop system.

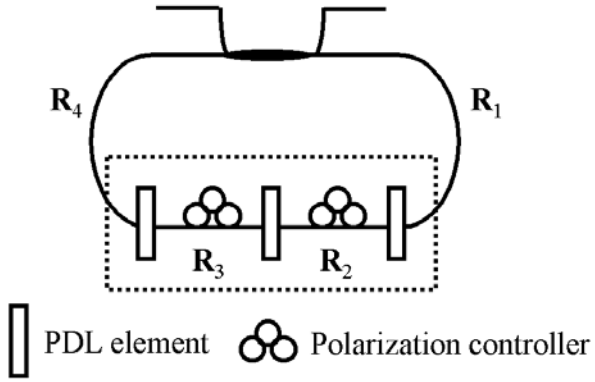

Fig. 5.6. Schematic diagram of how to define a “black box” in the loop system with multiple PDL elements

Because of the static nature of the recirculating loop system, it is possible to lump all the PDL elements together. Then each round trip can be treated as a black box to yield one PDL level. As shown in Fig. 5.6, in a system with multiple PDL elements, the rotation, including the contribution of fibers and the polarization controllers can be described as a rotation matrix $\mathbf{R}_i$, i = 1, 2, 3, 4. The accumulated PDL for one round trip is determined by the PDL elements and the rotations between the PDL elements, $\mathbf{R}_2$ and $\mathbf{R}_3$. The rotation matrices $\mathbf{R}_2$ and $\mathbf{R}_3$ adjust the relative orientation of the PDL elements, and hence control the accumulated PDL level in the system, so that the black box is defined as the dashed rectangular. The other rotations $\mathbf{R}_1$ and $\mathbf{R}_4$ change the alignment of the SOP of the signal to the axes of accumulated PDL rather than changing the accumulated PDL level. Therefore naturally, the random rotation provided by the loop-synchronous scrambler should be at location $\mathbf{R}_1$ or $\mathbf{R}_4$.

The loop-synchronous scrambler, which is treated as a combination of a PDL element and a rotation generator, is placed at the end of the loop as shown in Fig. 5.1. It is natural to break the loop from the loop coupler and consider one round trip of the loop from the

first EDFA to the loop-synchronous scrambler to be a black box that generates PDL. When the signal is transmitted in the system, it passes multiple black boxes with a rotation generated by the loop-synchronous scrambler in between, as shown in Fig. 5.7. By adjusting the polarization controllers between the PDL elements in the black box, which is equivalent to vary the alignment of the PDL elements, I was able to vary the PDL per round trip from 0.13 dB to 0.6 dB. Once the PDL level was chosen, I controlled the SOP of the light within the loop by adjusting the polarization controller outside the black box. I checked the black box regularly to avoid any drift in the round-trip PDL.

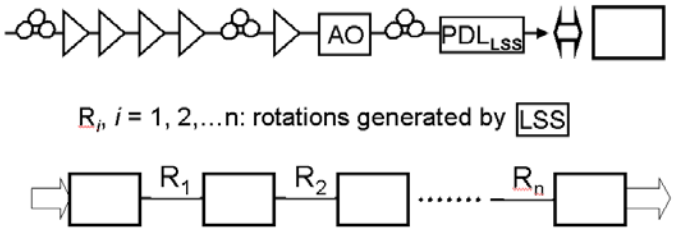

Fig. 5.7. How to control the PDL level in the loop system

For a traditional loop setup, in which the optical path is periodic, the rotations between the black boxes are identical for a given fiber realization. When one applies the loop-synchronous scrambling technique, the rotations are chosen randomly for one fiber realization and the system is called a scrambled loop system. In both cases, I collect the *Q*-factor distribution by randomly selecting multiple independent fiber realizations.

5.4.2 PDL level monitoring

As discussed in the previous section, the drift in the loop system may cause a change in the PDL level per round trip; hence the statistical behavior of the system is difficult to

repeat. In order to obtain a consistent result, one must constantly monitor the PDL level. The most commonly used methods to measure the PDL level are the Jones matrix eigen-analysis and the maximum-minimum power method. However, both methods are time consuming. The Jones matrix eigen-analysis requires one to measure the output polarization states corresponding to three different input polarization states, while the maximum-minimum power method requires one to scan all the possible input polarization state. Also, when applying these methods to a loop system, one must gate the instrument used in the measurement, or one must break up the loop system so that it operates as a straight-line system. Therefore, a more practical way to monitor the PDL in a loop system is necessary.

From our prior experiments discussed in Section 4.3.2.2 and 4.3.3, we observed that when the setting of PCs is optimized and the signal is off, the DOP evolution of the noise in the same polarization configuration is sensitive to the PDL level in the loop system. In practice, the DOP build-up of the noise is mainly due to the effect of PDL elements in the system during the first few round trips. So the DOP evolution of the noise may be a good candidate for monitoring the PDL level in the loop system without opening up the loop system. By using the reduced Stokes model, I can simulate the DOP evolution of the noise accurately, which then allows me to relate the DOP to the PDL in the loop system.

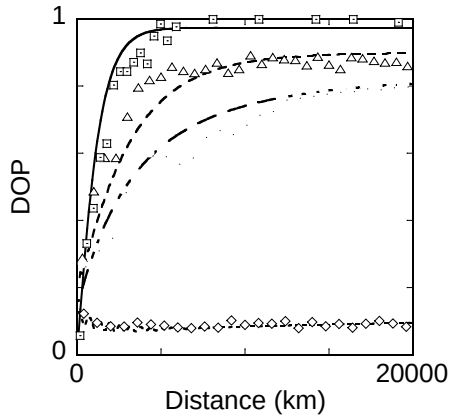

Fig. 5.8. Comparison of the measured and simulted DOP evolution of noise as a function of the propagation distance when the signal aligns with the low loss axis of the PDL element with different PDL levels. The solid line, the dashed line, the long dashed line and the dotted line are simulated results when the PDL per round trip is 0.6 dB, 0.35 dB, 0.25 dB and 0.1 dB. The squares, the triangles, the open circles and the diamonds are the corresponding measured result, respectively.

I show a comparison of the DOP evolution with different PDL level per round trip in Fig. 5.8. I first broke the loop to a 107 km straightline and used the maximum-minimum power method to measure the PDL level for one round trip. Then I connected the loop together and propagated 10 Gb/s RZ pulse modulated by $2^{15} - 1$ PRBS pattern. After adjusting the polarization controller in front of the first EDFA to obtain the lowest BER at 17,000 km, I turned off the signal and only allow noise to propagate in the system to obtain the DOP evolution of noise only. The solid line, the dashed line, the long dashed line and the dotted line are simulated results when the PDL per round trip is 0.6 dB, 0.35 dB, 0.25 dB and 0.1 dB. The squares, the triangles, the open circles and the diamonds are the corresponding measured result, respectively. In the simulation, I also took into account the effect of PDG. The PDG per EDFA was set to be 0.05 dB. The experimental results

agree with the simulated results very well. Note that when PDL is 0.1 dB, the noise is unpolarized during propagation. As discussed in Chapter 4, the PDG effect always adds noise to the direction orthogonal to the partially polarized noise. Hence, when PDL is not large enough, the noise keeps unpolarized as it propagates. The results show that if PDL is large enough, using the DOP build up of the noise, one is able to estimate the round trip PDL value without disconnecting the system.

5.5 Dynamic gain of EDFA and its effect on the input- scrambling rate

In a single channel system, people often employ an input scrambler, which modulates the input polarization states faster than the response time of the EDFA, to eliminate the effect of PDG [27], [32]. However, input polarization scrambling interacts with PDL and PMD in the system and can cause performance impairments that offset the improvements resulting from reducing PDG in the system. In general, PDL in the system converts the modulation of polarization states at the transmitter to undesired amplitude modulation. The potential impairment can be avoided by scrambling the polarization states of the signal above the data rate of the system so that the frequency of PDL induced amplitude modulation is beyond the bandwidth of the optical receiver [59]. However, this option is expensive at modern data rates. Furthermore, most of the commercially available high speed scrambler uses a *z*-cut $LiNbO_3$, which produces a chirp to the pulse.

Scrambling rates close to the response time of the EDFA have improved the system performance. This requires carefully choosing the scrambling rate range [59] so that the amplitude fluctuations are filtered out by the EDFA gain response. Otherwise, the transi-

ent of the EDFAs in the system will magnify the power fluctuation in return to introduce system impairment. In my study, I concentrate on the low scrambling technique to reduce the PDG effect.

5.5.1 Dynamic gain of EDFA

The dynamics of the gain response in an EDFA can be described by an ordinary differential equation (ODE) [60]. The amplifier dynamics are associated with the depletion and the refilling of the reservoir, the total number of excited ions in the amplifier. The refilling process is caused by the pump, where one pump photon can excite at most one ion. The depletion process is caused by the signal, where one signal input photon "burn" a very large number of ions in the reservoir through stimulated emission. Thus, the time scale connected to the depletion process is fast, while that connected to the refilling process are slow and depend on the pump power and the total number of dopant ions.

Under the assumptions of a two-level system, a homogeneously broadened gain spectrum, no excited state absorption, no background loss, and no self-saturation by ASE, the rate equation for the fraction of excited ions N_2, $0 \le N_2 \le 1$, as a function of distance *z* and time *t* can be described as [61]

$$\frac{\partial N_2(z,t)}{\partial t} = -\frac{N_2(z,t)}{\tau} - \frac{1}{\rho A}\sum_{j=0}^{N} u_j \frac{\partial Q_j(z,t)}{\partial z}. \tag{5.25}$$

In the equation, the parameter τ is the fluorescence time of the gain medium, ρ is the ion density in the doped fiber core of effective area *A*. The photon fluxes of channel $j, Q_j(z,t)$, j = 0, 1, …, N, along propagation distance *z* are described by

$$\frac{\partial Q_j(z,t)}{\partial z} = \rho u_j \Gamma_k \left[\sigma_j^T N_2(z,t) - \sigma_j^a\right] Q_j(z,t). \tag{5.26}$$

The parameters Γ_k, σ_j^e, and σ_j^a are the confinement factor and the emission and absorption cross sections of channel *j*, respectively and $\sigma_j^T \triangleq \sigma_j^e + \sigma_j^a$. The factor u_j gives the propagation direction of the photon fluxes. When $u_j = 1$, the light propagates from *z* = 0 to *z* = L, in which L is the length of the erbium-doped fiber. When $u_j = -1$, the light propagates in the opposite direction. The channel 0 is the pump of the EDFA. The logarithmic gain of channel *j* is defined as

$$G_j(t) \triangleq \int_0^L \frac{u_j \partial Q_j}{Q_j} = \ln\left[\frac{Q_j^{\text{out}}(t)}{Q_j^{\text{in}}(t)}\right] = B_j r(t) - A_j, \tag{5.27}$$

where $r(t) \triangleq \rho A \int_0^L N_2(z,t)\, dz$ is the reservoir. The two parameters A_j and B_j are defined as $A_j \triangleq \rho \Gamma_k \sigma_k^a L$ and $B_j \triangleq \Gamma_k \sigma_k^T / A$, respectively. One obtains the time dynamic of the reservoir by multiplying both sides of (5.25) by *dz* and integrating from 0 to L,

$$\frac{\partial r(t)}{\partial t} = -\frac{r(t)}{\tau} - \sum_{j=0}^{N}\left[Q_j^{\text{out}}(t) - Q_j^{\text{in}}(t)\right]. \tag{5.28}$$

Using (5.26) and (5.27), one obtains a first-order ODE describing the dynamic time behavior of the reservoir,

$$\frac{\partial r(t)}{\partial t} = -\frac{r(t)}{\tau} + \sum_{j=0}^{N} Q_j^{\text{in}}(t)\left[1 - e^{B_j r(t) - A_j}\right]. \tag{5.29}$$

By solving the ODE of (5.29), one is able to obtain the dB-gain of this EDFA, which is a linear function of *r*(*t*) for a given fiber. This dynamic behavior of gain makes the EDFA behaves like a high-pass filter as can be seen in Fig. 5. 11.

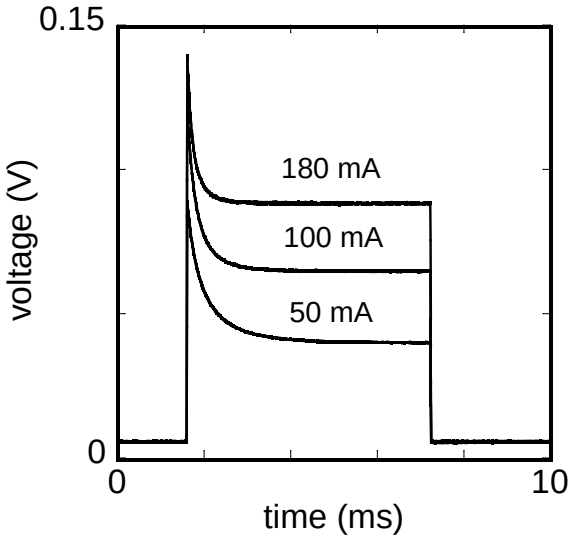

Fig. 5.9. Measured dynamic response of the fourth EDFA in the loop system shown in Fig. 5.1. The input power to the EDFA is – 6 dB and the pump currents of the 980 nm pump laser are 50 mA, 100 mA and 180 mA, respectively.

The dynamic gain of the EDFA depends on the pump power as well as the power of the input signal. In Fig. 5.9, I show the measured gain dynamic of the fourth EDFA in the system, whose position is shown in Fig. 5.1, with different pump powers. In the measurement, I use an acoustic-optic switch, which had a 100 ns increasing time to generate a square wave with a duty-cycle of 50% and pulse width of 5.5 ms. The pump power of the EDFA was adjusted by controlling of the pump current to the 980 nm pump laser and the input optical power was fixed at –6 dBm, which was a typical operation power. To avoid saturation of the detector, I placed a 5 dB attenuator in front of the receiver.

5.5.2 Selecting the input scrambling rate

In order to eliminate the effect of PDG and improve the signal to noise ratio of the system, one must scramble the polarization state faster than the EDFA response time. However, for a system having a single EDFA and a residual PDL, there is a dilemma. If the polarization state is scrambled faster than the EDFA response time, the PDL-induced amplitude modulation, which has the same frequency as the scrambling frequency, may be magnified by the EDFA transient. Fortunately, the transmission system involves a chain of EDFAs.

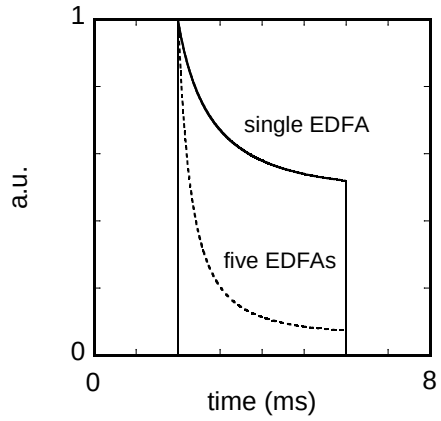

Fig. 5.10. Numerical comparison of the response time of a single EDFA and that of concatenated five identical EDFAs. The solid line is the simulated dynamic response of one EDFA and the dotted line is the simulated dynamic response of concatenated five EDFAs.

When multiple EDFAs are concatenated together, the total dynamic response is much faster than the dynamic response of a single EDFA. I demonstrated this effect by numerical comparison of the dynamic response of a single EDFA and that of five concatenated

EDFAs using a commercial simulation tool, VPI 4.0, Transmission maker^{TM} and Component maker^{TM}. In the simulation, each EDFA featured an 8 m Er-doped fiber with a dopant density of $10^{25}\ 1/\mathrm{m}^3$, which was close to that of a commercially available Er fiber — 402K5 manufactured by INO corp that we used in our EDFAs. A chain of five EDFAs is concatenated with 25 km fiber between every two of EDFAs. The fiber loss is 0.25 dB/km. Every EDFA was operated in the saturation regime and the gain compensated the fiber loss exactly. The input to the EDFA chain was a pulse train consisted of eight rectangular pulses with a 5 ms pulse width and a 50% duty circle. The peak power of the pulse is set to be –3 dBm. The output optical power was normalized by the output peak power. As shown in Fig. 5.10, the response time of a chain of five EDFAs is much faster than a single EDFA corresponding to a higher frequency response of the EDFA chain relative to the single amplifier.

With the presence of PDL in the system, the input scrambling converts the polarization modulation to the amplitude modulation, which can be described by $P_{\mathrm{in}} = P_0\left[1+\delta\sin\left(2\pi ft\right)\right]$, where P_0 is the average power and f is the modulation frequency. I experimentally compared the response of the first EDFA and that of five concatenated EDFAs, which is one round trip. All EDFAs were operated in saturation. In the experiment, I set P_0 to be –6 dBm and I varied f from 50 Hz to 300 kHz. I used the ratio of the maximum power to the minimum power, expressed in a logarithmic scale, to quantify the amplitude modulation. The input amplitude modulation was set to 0.6 dB to emulate the amplitude modulation induced by an element with 0.6 dB PDL and input scrambling. The amplitude modulation of the output of the first EDFA and the five concatenated EDFAs are shown in Fig. 5.11 as open diamonds and stars, respectively. In both cases,

the amplitude modulation decreases at low frequency due to the saturation of the EDFAs. However, the lowest frequency at which the amplitude modulation can pass without attenuation shifts from 5 kHz for a single EDFA to 30 kHz for five concatenated EDFAs. Therefore, one can scramble the input at a frequency in the window between 5 and 30 kHz to reduce both the PDG effect and the undesired amplitude modulation induced by PDL.

My colleague, Zhihang Hu, used the average inversion level model to simulate the time dependent gain in a single EDFA and five cascaded EDFAs, respectively [61]. The simulated results are shown in Fig. 5.11 as solid lines. In the simulation, the pump powers for the five EDFAs are between 19 dBm and 22 dBm, the erbium doped fiber lengths are between 4 and 8 m, the signal absorption and emission cross-section parameters are 2.43 dB/m and 2.88 dB/m, respectively, and the pump absorption cross-section parameter is 2.40 dB/m. The measured results and the simulated results agree very well with each other.

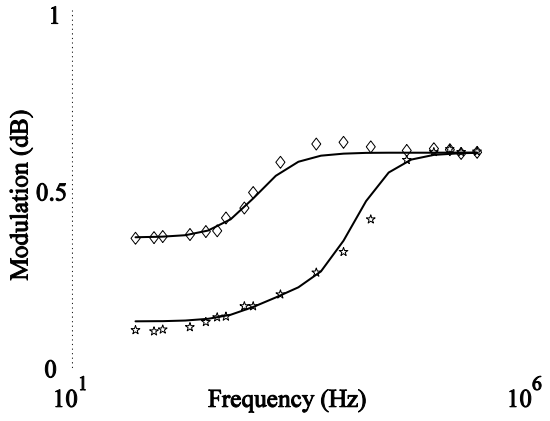

Fig. 5. 11. Amplitude modulation as a function of input modulation frequency. The star and diamond show the amplitude modulation after five EDFAs and one EDFA, respectively, for a sinusoidal input. Lines show the corresponding simulation results.

I showed this filtering effect by measuring the power fluctuation of a scrambled loop with different scrambling rate at the input. Fig. 5.12 shows the measured results when the scrambling frequency of the input scrambler is 300 kHz, 25 kHz and 12.6 kHz, respectively. In this experiment, I propagated 10 Gb/s RZ pulses modulated by $2^{15} – 1$ PRBS pattern in the scrambled loop system and set the PDL level of the system to be 0.6 dB per round trip. The average power of the loop was monitored by a photodetector with an 800 kHz bandwidth after the coupler. The output of the detector was display on a 300 MHz digital sampling scope triggered by the control signal of the AO switches.

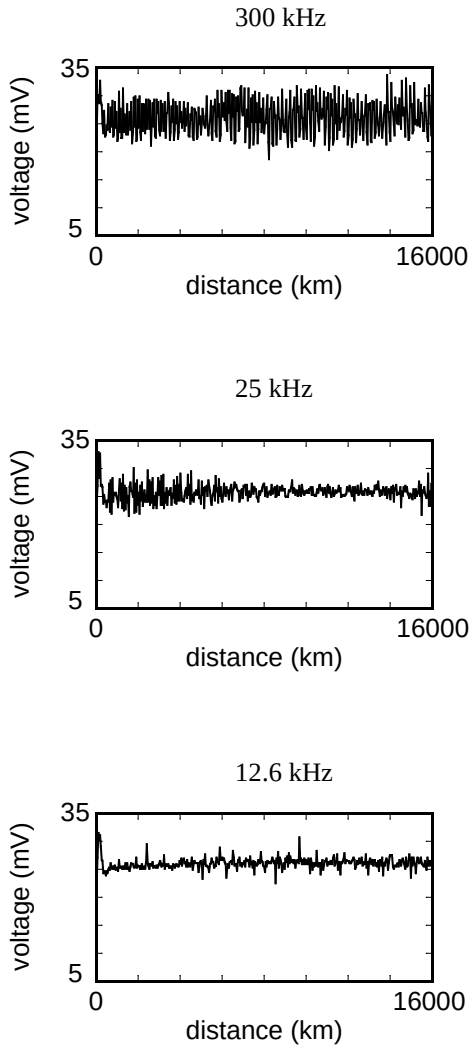

Fig. 5.12. Measured average power fluctuation when the scrambling frequency of the input scrambler is 300 kHz, 25 kHz and 12.6 kHz, respectively

As shown in Fig. 5.12, when the input-scrambling rate is 300 kHz, the average power of the loop system fluctuates significantly. As the input-scrambling rate is reduced, the fluctuation reduces greatly. When the scrambling rate is 12.6 kHz, the fluctuation due to the input scrambling is not noticeable. Since the response of single EDFA is about 5 kHz, choosing an input scrambling rate of 12.6 kHz is sufficent to reduce the PDG effect.

5.6 Results and discussions

I studied the system performance of a scrambled loop by measuring the *Q*-factor distributions. I extrapolated the *Q*-factor from the BER margin measurements. In order to concentrate on the behavior of the optical noise, I carefully measured the electrical noise floor by doing back-to-back measurement without transmission. I subtracted the effect of electrical noise from all the measured data, as discussed in Section 3.6.

I first investigated the *Q*-distribution of the loop system at 10,000 km for PDL = 0.2 dB, 0.4 dB and 0.6 dB per round trip, respectively. For each *Q*-factor samples, the loop-synchronous scrambler provided the same rotation for each round trip to emulate the periodic nature of the loop system. The *Q*-factor at 10,000 km was obtained from the BER margin measurement. Since this measurement took about 20 seconds, the rotation was repeated until the margin measurement was finished. Then I randomly chose another rotation to obtain a different *Q* sample. I show the histogram of the *Q*-factor distribution when the PDL was 0.2 dB per round trip in Fig. 5.13. The pdf of the *Q*-factor distribution was calculated from 400 independent *Q*-samples. The loop system has a much broader *Q*-factor distribution than one would expect for the corresponding straight-line system, and the high *Q* tail overestimates the system performance of a straight-line system. Because of the periodicity of the loop, the signal may align with the low loss axis of the PDL element in the system every round trip; therefore, the noise orthogonal to the signal in Jones space is effectively reduced due to the larger attenuation from the high loss axis of the PDL element. The *Q*-factor is artificially improved. For larger PDL values, the orthogonal noise is eliminated more rapidly, and the maximum *Q*-factor will be even larger.

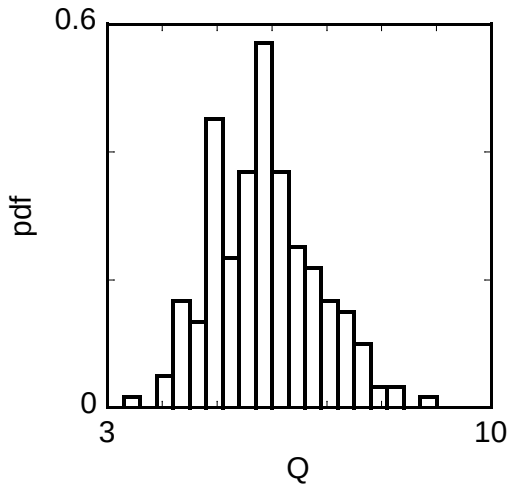

Fig. 5.13. Measured *Q*-factor distribution of a loop system at 10,000 km when the PDL per round trip is 0.2 dB.

To break the periodicity of the loop system and to more accurately emulate the PMD and PDL of a straight-line system, I generated a different random rotation for each round trip. This set of random rotations was repeated until the measurement was finished. Then I used another independent set of random rotations and repeated the same procedure to obtain another sample. I obtained 400 samples of the *Q*-factor for each of the three PDL values. In Fig. 5.14, I showed the measured *Q*-factor distribution when the PDL was 0.2 dB per round trip as a histogram with bars and the simulated result as a solid line.

In the simulation, I generated a random rotation for each round trip and the *Q*-factor is calculated using the *Q*-formula (3.29), which taked into account the polarization state of both the signal and the noise. Using the Monte Carlo simulation, I generated 10,000 sets of random rotations, which were independent of each other to build the statistics of the *Q*-distribution. As show in Fig. 5.14, the simulated result agrees with the experimental results very well.

With this loop-synchronous scrambling technique, the signal orientates randomly, so that it is rare that the signal aligns with the low loss axis constantly. As a consequence, the noise orthogonal to the signal cannot be reduced. Although the *Q*-distribution tends to be aligned with the low-*Q* portion of the *Q*-distribution, shown in Fig. 5.13, due to the reduction of OSNR, the *Q*-factor distribution is much narrower than that in the loop and closely resembles the *Q*-distribution for a straight-line system. Moreover, because the loop-synchronous scrambler changes the fiber orientation randomly, once the PDL level of the system is fixed, the results are repeatable.

I also employed a polarization scrambler at the transmitter to reduce the effect of PDG. In the experiment, I carefully chose a slow scrambling rate, 12.6 kHz, so that I was able to reduce the PDG effect and simultaneously to suppress the amplitude modulation induced by the combination of the dynamic gain response and PDL [59]. In Fig. 5.14, I show the measured and simulated results for the system with both transmitter and loop-synchronous scrambling. With the transmitter scrambler, in addition to improving the average performance of the system, the variation of the system performance is reduced.

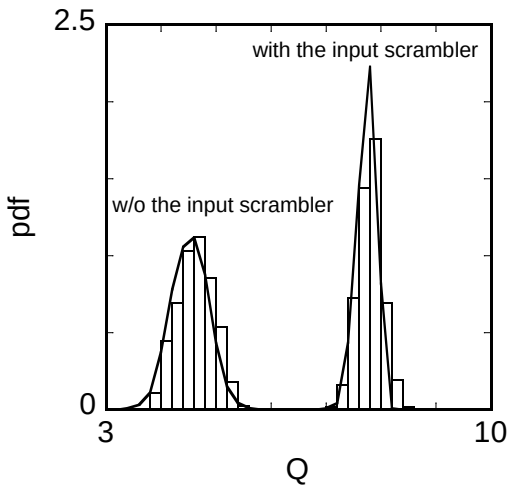

Fig. 5.14. Distribution of *Q*-factor of a scrambled loop system when the PDL per round trip is 0.2 dB with and without the input scrambling at 10,000 km. The histogram with bars shows the measured results and the solid curves show the simulated results.

Since the scrambling rate at the transmitter is low, compared to the frequency response of the receiver, the signal is always polarized for the receiver, and the signal-noise beating corresponding to each input polarization state contributes to the variation of the *Q*-factor. In order to simulate the input scrambling accurately, instead of turning off the PDG in the EDFA and calculating *Q*-factor for different fiber realizations, in the simulation, for one fiber realization, I generated 100 input polarization states, which formed a big circle on the Poincaré sphere to simulate the input polarization scrambler. Then I followed the polarization evolution of each input polarization state. Since the effective PDG effect is proportional to the total DOP before each EDFA, I combined all the polarization states corresponding to different input polarization to obtain the total DOP. The *Q*-factor was calculated separately corresponding to different input polarization. In the simulation, I randomly chose 100 fiber realizations; therefore in total 10,000 *Q*-factor samples were

collected. As shown in Fig. 5.14, the simulated result agrees with the experimental result very well.

In the scrambled loop system, when I adjusted the PDL per round trip in the loop to a larger value I observed behavior similar to the low PDL case except that the *Q*-factor distribution was broader. When the PDG effect was reduced by the input scrambling technique, the system performance was improved and the variance of the system performance was reduced. However, when the input scrambler is on, the *Q*-factor distribution is asymmetric. In Fig. 5.15, I show the measured and simulated *Q*-factor distributions with the loop-synchronous scrambler, with and without the transmitter scrambler, when PDL is 0.6 dB per round trip. The simulation shows that it is the repolarization of the noise that causes the asymmetry of the *Q*-distribution. Since the transmitter scrambler eliminates the effect of PDG, the noise tends to repolarize due to the PDL in the system.

For those samples that the OSNR is larger than the average, the signal is often closely aligned with the low-loss axis of PDL elements and suffers less attenuation than the noise mode that is aligned to the high loss axis of the PDL does. In this case, the noise tends to become copolarized with the signal because the noise orthogonal to the signal is reduced by the high loss axis of PDL elements, so that the signal-noise beating is enhanced. Therefore, the *Q*-factor is lower than that of a system with the same OSNR but in which the noise is unpolarized. Consequently, the large *Q* portion of the *Q*-distribution with unpolarized noise is missing for polarized noise and the *Q*-distribution is asymmetric. By contrast, if in the simulation I artificially assumed that the noise prior to the receiver was unpolarized by setting $\Gamma_{\text{ASE-ASE}} = 1$ and $\Gamma_{\text{S-ASE}} = 0.5$, in (3.29), and keeping all other parameters the same, then as I show with a dashed line in Fig. 5.15, the *Q*-distribution is

much more symmetric. The results show that to truly predict the system performance and to estimate the outage probability, one must include effects of partially polarized noise in the receiver model. Otherwise, the simulation result may overestimate the average system performance as well as the variation of the system performance.

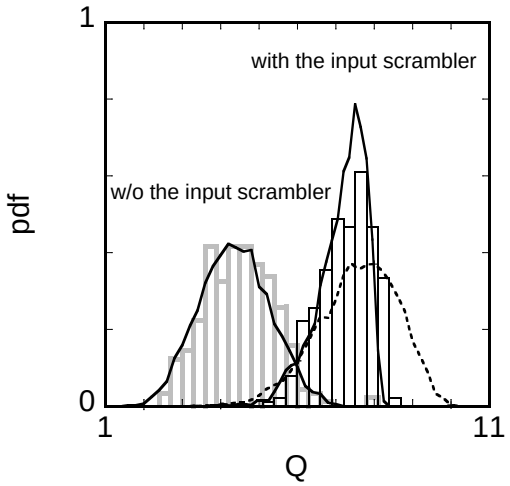

Fig. 5.15. Distribution of *Q*-factor of a scrambled loop with and without the input scrambling when the PDL per round trip is 0.6 dB at 10,000 km. The histograms with bars are the measured results. The solid curves are the corresponding simulated results. The dashed line is the simulated result when the noise entering the receiver is artificially assumed to be unpolarized.

In Fig. 5.16, I show the comparison of the simulated and measured means and the confidence interval of these *Q* distribution with different PDL levels, with and without the input scrambling. The simulated average *Q* and confidence interval without the input scrambling are shown as the solid line and the dashed lines, respectively. The confidence interval is the interval between the average *Q* plus one standard deviation and the average *Q* minus one standard deviation. The dots and the open circles are the corresponding ex-

perimental result. The simulated results of the average *Q*-factor and the confidence interval with the input scrambling are shown as the dotted line and the long dashed lines, respectively. The filled squares and the open squares are corresponding experimental results.

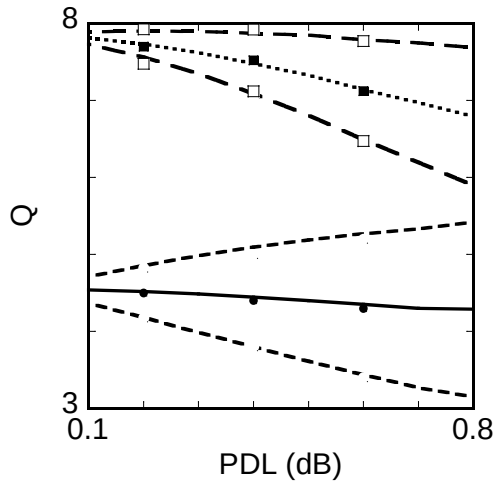

Fig. 5.16. Comparison of the average system performance and the variation as a function of PDL per round trip with and without the input scrambling. The simulated average *Q* and the confidence interval without the input scrambling are shown as the solid line and the dashed lines, respectively. The dots and the open circles are corresponding experimental results. The simulated results of the average *Q*-factor and the confidence interval with the input scrambling are shown as the dotted line and the long dashed lines, respectively. The filled squares and the open squares are corresponding experimental results.

Without the input scrambler, the mean *Q* is not sensitive with the increasing of the PDL in the system; however, the variation of the system performance increases greatly. With the input scrambler, the mean *Q* of the system performance improved significantly

and the variation of the system performance reduces. However, in this case, the mean *Q* decreases as the PDL level in the system increase. The reason lies on the fact that when the OSNR is above average, the noise repolarizes in the direction close to the signal, so that the signal-noise beating is enhanced, decreasing *Q*. Since the PDG effect is effectively reduced in my system with an appropriate input scrambling, my system can be used in the study of intra-channel effects of a WDM straight-line system with wide channel spacing where the inter channel effects are negligible.

5.7 Conclusions

I demonstrated that with the loop-synchronous scrambler, which breaks up the periodicity of the loop system, the performance of a loop system closely resembles that of a straight-line system. I compared the performance of the system with and without the loop-synchronous scrambler by measuring the *Q*-factor distributions. I also employed a second polarization scrambler in the transmitter with a scrambling rate of 12.6 kHz, which was faster than the response of single EDFA in the system, to eliminate the PDG effect and the system performance is proved. By carefully controlling the PDL level in the system, I was able to investigate the system performance with different PDL level and obtained repeatable results. I showed that repolarization of noise due to significant PDL in the system causes an asymmetric *Q*-factor distribution. I compared our experimental results with numerical simulations and obtain excellent agreement.

Chapter 6

Summary and future work

6.1 Summary

In my study, I systematically investigated the DOP evolution of the signal and the noise, the *Q*-factor distribution and the polarization state evolution in recirculating loop systems. The behavior of a loop system with PDL is very different from that of a straight-line system due to the periodicity of the optical path and the present of the PDL. The loop systems often overestimate the system performance of straight-line systems due to the reduction of the noise constantly aligned with the high loss axis of the PDL element and the polarization state forms a spiral like evolution.

The most important goal in my study is to seek an approach that one can emulate the *Q*-factor distribution of the straight-line system using the recirculating loop system. I fulfilled this goal and overcame the limitation of the recirculating loop system by develop-

ing a loop-synchronous scrambling technique to break up the periodicity of the loop system.

Besides the loop-synchronous scrambling technique, I addressed several other critical issues in loop experiments. I developed procedures to control the PDL level in the system, which was necessary to obtain repeatable results and to monitor the PDL level without physically taking apart the loop system. I also investigated the effect of EDFA transient on the input scrambling. By carefully selecting the input scrambling rate, I was able to effectively reduce the PDG effect and the undesired amplitude modulation.

I investigated the system performance of a scrambled loop system by measuring the *Q*-factor distribution with different PDL levels in the system, with and without the input scrambler. I demonstrated that with the loop-synchronous scrambling technique, the *Q*-factor distribution of a recirculating loop system closely resembled that of a straight-line system. By carefully controlling the PDL level in the system, I was able to obtain repeatable statistics results. By carefully choosing the scrambling rate, one can improve the system performance and reduce the performance variation and I show that the *Q*-factor distribution is asymmetric with a significant PDL in the system.

I also adapted the reduced Stokes model, which was used to study the penalty due to polarization effects in WDM system, to simulate the polarization evolution and the system performance of a single channel DMS system. The excellent agreement of the experimental results and the numerical simulations provided the first experimental validation of the reduced Stokes model.

In addition, the results show that polarization effects such as PDL, not only result in a variation of the OSNR, but also in repolarization of the noise. However, the widely used

Q-factor formula only considers two extreme cases in terms of the polarization: unpolarized noise and the noise that is copolarized with the signal. In real systems, the repolarized noise complicates the relationship between the SNR and the *Q*-factor. It is very important to develop an accurate receiver model, which takes into account the effect of the partially polarization noise. I introduced two factors — (3.27) and (3.28) — to account for the repolarized noise in the receiver, and then I derived the *Q*-factor formula in (3.29). I also derived an analytical probability density function of the *Q*-factor distribution. I validated the *Q*-factor formula and the pdf of the *Q*-factor distribution by the excellent agreement of the experimental results, the numerical simulations, and the analytical results. I show that even for a fixed SNR, the *Q*-factor may vary depending on the DOP of the noise and the angle between the Stokes vectors of the signal and highly polarized noise will cause a larger variation in the system performance compared to less polarized noise. Since the *Q*-factor formula does not require one to determine the pulse evolution during the propagation, it works well with the reduced Stokes model.

6.2 Future works

The reduced polarization model relies on the assumption that the system penalty due to polarization effects is separable from other penalties in the system, such as dispersion and nonlinearities. In the work reported in this dissertation, the excellent agreement between the experimental results and the simulated results suggest that in our system, the polarization effects are not coupled to the nonlinearity and dispersion. However, in WDM

systems, polarization mode dispersion can result in a random walk off of different channels. If there is PDL in the system, these two effects along with the saturation of the EDFAs will result in an energy transfer between channels. That may cause the coupling of other effects. For instance, if the power in a channel changes due to PDL, the effect of nonlinearity will also change. Therefore, in the future work, it is very important to study in what parameter range that the penalties due to polarization effects can be separated from those of others and the reduced model holds in a WDM system.

The dynamical behavior of the inter-channel, polarization-dependent process is complicated. It is not only related to the magnitude of polarization effects, such as PMD and PDL, but also related to the number of the channels and the channel spacing. The inter-channel polarization effects may affect the channel nonlinearity and the chromatic dispersion compensation. Future work will investigate the interaction between the polarization effects and the effects of fiber nonlinearity and chromatic dispersion, when all the channels are coploarized or orthogonally polarized at the input, respectively. It is also very important to examine the combined effect when the channel spacing becomes small.

Appendix

Because a recirculating loop system has a static nature, inherently it is periodic. We may write its Jones transfer matrix after *n* round trips as $\mathbf{T} = \mathbf{M}_{\text{loop}}^{n}$, where $\mathbf{M}_{\text{loop}}$ is the Jones matrix for one round trip of the loop an the mode of $\mathbf{M}_{\text{loop}}$. This 2×2 Jones matrix has a pair of complex eigenvectors $\mathbf{u}_{\pm}$ and corresponding eigenvalues $\lambda_{\pm}$ and $|\lambda_{\pm}| \le 1$. If λ is an eigenvalue of $\mathbf{M}_{\text{loop}}$, then λ^{n} is an eigenvalue of **T**. A vector of an arbitrary field can always be written as the combination of these two eigenvectors. It follows that the input field can be written as

$$\mathbf{u}_{\text{in}} = c_{+}\mathbf{u}_{+} + c_{-}\mathbf{u}_{-}, \tag{A.1}$$

then the output field vector is

$$\mathbf{u}_{\text{out}} = \mathbf{T}\mathbf{u}_{\text{in}} = c_{+}\lambda_{+}^{n}\mathbf{u}_{+} + c_{-}\lambda_{-}^{n}\mathbf{u}_{-}. \tag{A.2}$$

If we let $\lambda_{\pm} = |\lambda_{\pm}|\exp(i\phi_{\pm})$ and $c_{\pm} = |c_{\pm}|\exp(i\psi_{\pm})$, then the corresponding output Stokes vector is $\mathbf{s}_{\text{out}} = \left(\mathbf{u}_{\text{out}}^{\dagger}\sigma_3\mathbf{u}_{\text{out}}, \mathbf{u}_{\text{out}}^{\dagger}\sigma_1\mathbf{u}_{\text{out}}, -\mathbf{u}_{\text{out}}^{\dagger}\sigma_2\mathbf{u}_{\text{out}}\right)^{T}$, yielding

$$\mathbf{s}_{\text{out}} = |c_{+}|^2|\lambda_{+}|^{2n}\mathbf{s}_{+} + |c_{-}|^2|\lambda_{-}|^{2n}\mathbf{s}_{-} + 2|c_{+}||c_{-}|\left(|\lambda_{+}||\lambda_{-}|\right)^{n}\,\text{Re}\left[\mathbf{s}_{c}e^{-i(n\Delta\phi+\Delta\psi)}\right], \tag{A.3}$$

where $\mathbf{s}_{\pm}$ are the Stokes vectors associated with the Jones eigenvectors $\mathbf{u}_{\pm}$, $\mathbf{s}_{c} \equiv \left(\mathbf{u}_{+}^{\dagger}\sigma_3\mathbf{u}_{-}, \mathbf{u}_{+}^{\dagger}\sigma_1\mathbf{u}_{-}, -\mathbf{u}_{+}^{\dagger}\sigma_2\mathbf{u}_{-}\right)^{T}$, $\Delta\phi = \phi_{+} - \phi_{-}$, and $\Delta\psi = \psi_{+} - \psi_{-}$. In the above expressions, the σ_k are the standard Pauli spin matrices. In (A.3), the coefficients of $\mathbf{s}_{\pm}$ are de-

termined by the eigenvalues $\lambda_{\pm}$. If the eigenvalues have different magnitudes, then one obtains spiral motion. The smaller eigenvalue decays faster as the parameter *n*, the number of round trip increases. The spiral centers are given by one of the polarization eigenstates $\mathbf{s}_{\pm}$ that has larger coefficient due to the eigenvalue with larger magnitude. The rotation is described by the third term, where the rotation angle of the spiral due to one round trip of the recirculating loop is given by the phase difference of the eigenvalues, $\Delta\phi$. In addition, the ratio of the magnitudes of the eigenvalues gives the relative decay rates of the coefficients, thus yielding the rate of convergence to a spiral center.

In order to understand the spiral behavior in a loop with PDL, we describe the transformation of the PDL as a Jones matrix, which is written as

$$\mathbf{M}_{\mathrm{PDL}} = \begin{bmatrix} 1 & 0 \\ 0 & 1-\varepsilon \end{bmatrix}, \tag{A.4}$$

where the strength of the PDL is given by a small nonnegative parameter ε that is less than one and the direction of the second component is the high loss axis of the PDL. Due to the static nature of the loop, we are able to lump all the PDL elements in the system to on element at the end of each round trip. Hence the transfer matrix of one round trip can be written as

$$\mathbf{M}_{\mathrm{loop}} = \mathbf{M}_{\mathrm{PDL}}\mathbf{M}_{\mathrm{rot}}, \tag{A.5}$$

where $\mathbf{M}_{\mathrm{rot}}$ is a unitary matrix representing a fixed rotation on the Poincaré sphere giving the rotation due to the fiber and the loop's polarization controller, and $\mathbf{M}_{\mathrm{PDL}}$ represents the effect of PDL in one round trip of the loop. Note that in this formulation, we have neglected the effects of noise, PDG, and amplifier saturation. Our reduced model simulations do consider these effects and show that the predominant effects that alter the polari-

zation state of a signal are the random fiber rotation and the PDL. In Jones space, the matrix $\mathbf{M}_{\text{rot}}$ can be expressed in the form

$$\mathbf{M}_{\text{rot}} = \begin{bmatrix} \cos\frac{\gamma}{2} + ix\sin\frac{\gamma}{2} & -(z-iy)\sin\frac{\gamma}{2} \\ (z+iy)\sin\frac{\gamma}{2} & \cos\frac{\gamma}{2} - ix\sin\frac{\gamma}{2} \end{bmatrix}. \tag{A.6}$$

Since an arbitrary rotation on the Poincaré sphere can be expressed as a rotation through an angle γ about an axis, which is given by a unit vector $\mathbf{s}_{\text{rot}} = (x, y, z)^t$, this rotation matrix can be easily converted to Stokes space. In this notation, although the low-loss axis of the PDL is given by $\mathbf{s}_{\text{PDL}} = (1,0,0)^t$ in Stokes space, the results are general.

We exploit the fact that ε is small by using standard perturbation methods to expand our eigenvector in powers of ε [49]. We seek eigenvalues and eigenvectors that satisfy $(\mathbf{M}_{\text{loop}} - \lambda\mathbf{I})\mathbf{u} = \mathbf{0}$ and expand λ and $\mathbf{u}$ in power series in ε as $\lambda_{\pm} = \lambda_0 + \varepsilon\lambda_1 + O(\varepsilon^2)$ and $\mathbf{u}_{\pm} = \mathbf{u}_0 + \varepsilon\mathbf{u}_1 + O(\varepsilon^2)$. From these expressions, we can compute the Stokes eigenvector in powers of ε as well, obtaining $\mathbf{s}_{\pm} = \mathbf{s}_{\pm}^{(0)} + \varepsilon\mathbf{s}_{\pm}^{(1)} + O(\varepsilon^2)$. Doing this type of expansion yields, to $O(\varepsilon)$, the Stokes eigenvectors

$$\mathbf{s}_{\pm} = \pm\mathbf{s}_{\text{rot}} + \tfrac{1}{2}\varepsilon\left[\mathbf{s}_{\text{PDL}} \mp \mathbf{s}_{\text{rot}} + (\mathbf{s}_{\text{rot}} \times \mathbf{s}_{\text{PDL}})\cot\tfrac{\gamma}{2}\right] + O(\varepsilon^2). \tag{A.7}$$

Note that due to the $O(\varepsilon)$ corrections, the eigenstates in Stokes space are not antiparallel in the presence of PDL, unlike the principal states for PMD [51]. This is illustrated in Fig. 4.9 (a). We may use this expansion to compute the output Stokes vector for an arbitrary input state using (A.1), (A.2) and (A.3), as well, yielding

$$\mathbf{s}_{\text{out}} = A_+^n |c_+|^2 \mathbf{s}_+ + A_-^n |c_-|^2 \mathbf{s}_- + 2B^n |c_+||c_-|\left[\mathbf{t}_1 \sin(n\gamma + \Delta\psi) - \mathbf{t}_2 \cos(n\gamma + \Delta\psi)\right] + \ldots \tag{A.8}$$

where $\mathbf{t_1} = \left(\mathbf{s}_{\text{rot}} \times \mathbf{s}_{\text{PDL}}\right) \big/ \left|\mathbf{s}_{\text{rot}} \times \mathbf{s}_{\text{PDL}}\right|$ and $\mathbf{t_2} = \mathbf{s}_{\text{rot}} \times \mathbf{t_1}$, and where we are neglecting higher-order contributions. In this expression,

$$A_{\pm} = 1 - \varepsilon(1 \mp \mathbf{s}_{\text{rot}} \cdot \mathbf{s}_{\text{PDL}}) + O(\varepsilon^2), \tag{A.9}$$

and

$$B = 1 - \varepsilon + O(\varepsilon^2). \tag{A.10}$$

From (A.8), one can see that the *B* term contains sinusoidal pieces that correspond to the spiral or circular motion on the Poincaré sphere and the $A_{\pm}$ term provide the spiral center.

Bibliography

1. H. Taga, M. Suzuki, N. Edagawa, H. Tanaka, Y. Yoshida, S. Yamamoto, S. Akiba, and H. Wakabayashi, “Multi-thousand kilometer optical soliton data transmission experiments at 5 Gb/s using an electroabsorption modulator pulse generator,” *IEEE J. Lightwave Technol*., vol. 12, pp. 231–236, 1994.
2. N. Kikuchi, S. Sasaki, and K. Sekine, “10 Gbit/s dispersion-compensated transmission over 2245 km conventional fibres in a recirculating loop,” *IEE Electron. Lett*., vol. 31, pp. 375–377, 1995.
3. S. Ryu and S. Akiba, “Eight-wavelength, densely-spaced coherent WDM recirculating-loop experiments at 2.5 Gbit/s over 600 km,” *IEE Electron. Lett*., vol. 30, pp. 1613–615, 1994.
4. M. C. Wu, J. K. Wong, K. T. Tsai, Y. L. Chen, and W. I. Way, “740-km transmission of 78-channel 64-QAM signals (2.34 Gb/s) without dispersion compensation using a recirculating loop,” *IEEE Photon. Tecnhol. Lett*., vol. 12, pp. 1255–1257, 2000.
5. T. Sakamoto, M. Fukui, M. Jinno, J. Kani, S. Aisawa, H. Ono, M. Yamada, and K. Oguchi, “Recirculating loop experiment for 1580-nm-band large-scale WDM network using dispersion-shifted fiber,” *IEEE Photon. Technol. Lett*., vol. 10, pp. 618–620,1998.
6. T. Otani, T. Miyazaki, and S. Yamamoto, “Optical 3R regenerator using wavelength converters based on electroabsorption modulator for all-optical network applications,” *IEEE Photon. Technol. Lett*., vol. 12, pp. 431–433, 2000.

7. S. Bigo, P. Brindel, O. Leclerc, E. Brun_Maunand, and E. Desurvire, “Error-free 20-Gbit/s soliton transmission over 7150 km through all-optical synchronous phase modulation,” *Tech. Dig. Opt. Fiber Commun. Conf.*, OFC’97, paper WH1, 1997.
8. E. Lichtmann, “Performance degradation due to polarization dependent gain and loss in lightwave systems with optical amplifiers,” *IEE Electron. Lett.*, vol. 29, pp. 1969–1970, 1993.
9. L. J. Wang, J. T. Lin, and Peida Ye, “Analysis of polarization-dependent gian in fiber amplifiers,” *IEEE J. Quantum. Electron*., vol. 34, pp. 413–418, 1998.
10. I. Haxell, “Polarization effects in WDM long-haul optically amplified systems,” *IEE Electron. Lett*., vol. 32, pp. 374–376, 1996.
11. J. Zhou and M. J. O’Mahony, “Optical transmission system penalties due to fiber polarization mode dispersion,” *IEEE Photon. Technol. Lett*., vol. 6, pp. 1265–1267, 1994.
12. M. C. DeLignie, H. G. J. Nagel, and M. O. Deventer, “Large polarization mode dispersion in fiber optic cables,” *IEEE J. Lightwave Technol*., vol. 12, pp. 1325–1329, 1994.
13. P. S. Cho, P. Sinha, D. Mahgerefteh, and G. M. Carter, “All-optical regeneration at the receiver of 10-Gb/s RZ data transmitted over 30 000 km using an electroabsorption modulator,” *IEEE Photon. Technol. Lett*., vol. 12, pp. 205–207, 2000.
14. H. J. Thierle, R. I. Killey, and P. Bayvel, “Pump-probe investigation of cross-phase modulation in standard-fibre, dispersion compensated WDM recirculating

loop," *Tech. Dig. of Lasers and Electro-Optics Conf.*, CLEO'99, paper CWH1, 1999.

15. C. Peucheret, I. Munoz, F. Liu, A. Buxens, and S. N. Knudsen, "L-band transmission over 1000 km using standard and dispersion-compensating fibres in pre-compensation scheme optimised at 1550 nm," *IEE Electron. Lett.*, vol. 35, pp. 1759–1761, 1999.
16. Y. Sun, D. Wang, P. Sinha, G. M. Carter, and C. R. Menyuk, "Polarization evolution in a 107-km dispersion-managed recirculating loop," *Tech. Dig. of Lasers and Electro-Optics Conf.*, CLEO'00, paper CML3, 2000.
17. L. –S. Yan, Q. Yu, Y. Xie, and A. E. Willner, "Statistical measurement of the combined effect of PMD and PDL using a 10-Gb/s recirculating loop testbed," *Tech. Dig. Optic. Fiber Commun. Conf.*, OFC'01, paper WT5, 2001.
18. D. Marcuse, C. R. Menyuk, and P. K. A. Wai, "Application of the Manakov-PMD equation to studies of signal propagation in optical fibers with randomly varying birefringence," *IEEE J. Lightwave Technol.*, vol. 15, pp. 1735–1745, 1997.
19. C. R. Menyuk, "A new derivation of the nonlinear Schrodinger equation for physically realistic optical fibers," in *Tech. Dig. Conf. Laser and Electro-Optics* (CLEO'99), paper CMH3, 1999.
20. R.–M. Mu, V. S. Grigoryan, C. R. Menyuk, G. M. Carter, and J. M. Jacob, "Comparison of theory and experiment for dispersion-managed solitons in a recirculating fiber loop," *IEEE J. Select. Topics Quantum Electron.*, vol. 6, pp. 248–257, 2000.

21. D. Wang and C. R. Menyuk, “Reduce model of the evolution of the polarization states in wavelength-division-multimplexed channels,” *Opt. Lett*., vol. 23, pp. 1677–1679, 1998.

22. D. Wang and C. R. Menyuk, “ Calculation of penalties due to polarization effects in a long-haul WDM system using a Stokes parameter model,” *IEEE J. Lightwave Technol*., vol. 19, pp. 487 – 494, 2001.

23. D. Marcuse, “Derivation of analytical expressions for the bit-error probability in lightwave systems with optical amplifiers,” *IEEE J. Lightwave Technol*., vol. 8, pp. 1816–1823, 1990.

24. P. A. Humblet and M. Azizoğlu, “On the bit error rate of lightwave systems with optical amplifiers,” *IEEE J. Lightwave Technol*., vol. 9, pp. 1576–1582, 1991.

25. E. A. Golovchenko, A. N. Pilipetskii, N. S. Bergano, D. R. Davidson, F. I. Khatri, R. M. Kimball, and V. J. Mazurczyk, “Modeling of transoceanic fiber-optic WDM communication systems,” *IEEE J. Select. Topics. Quantum Electron*., vol. 6, pp. 337–347, 2000.

26. R. Noe, D. Sandel, M. Yoshid-Dierolf, S. Hinz, V. Mirvoda, A. Schopflin, C. Gungener, E. Gottwald, C. Scheerer, G. Fischer, T. Wevrauch, and W. Haase, “Polarization mode dispersion compensation at 10, 20, and 40 Gb/s with various optical equalizers,” *IEEE J. Lightwave Technol*., vol. 17, pp. 1602–1616, 1999**.**

27. F. Bruyère, O. Audouin, V. Letellier, G. Bassier, and P. Marmier, “Demonstration of an optimal polarization scrambler for long-haul optical amplifier systems,” *IEEE Photon. Technol. Lett*., vol. 6, pp. 1153–1155, 1994.

28. S. Hinz, D. Sandel, F. Wüst, and R. Noé, “Polarization multiplexed 2×20 Gbit/s RZ transmission using interference detection,” in *Tech. Dig. Optical Fiber Commun. Conf.* (OFC’2001), paper WM4, 2001.
29. C. D. Poole, R. W. Tkach, A. R. Chraplyvy, and D. A. Fishman, “Fading in lightwave system due to polarization-mode-dispersion,” *IEEE Photon. Technol. Lett*., vol. 3, pp. 68–70, 1991.
30. C. R. Menyuk, D. Wang, and A. N. Pilipetskii, “Repolarization of polarization-scrambled optical signals due to polarization dependent loss,” *IEEE Photon. Technol. Lett*., vol. 9, pp 1247 – 1249, 1997.
31. P. Wysocki and V. Mazurczyk, “Polarization dependent gain in Erbium-doped fiber amplifiers: computer model and approximate formulas,” *IEEE J. Lightwave Technol*., vol. 14, pp. 572–584, 1996.
32. V. J. Mazurczyk and J. L. Zyskind, “Polarization dependent gain in Erbium-doped fiber amplifiers,” *IEEE Photon. Technol. Lett*., vol. 6, pp. 616–618, 1994.
33. H. Taga, N. Edagawa and M. Suzuki, “ Impact of polarization hole burning effect in transoceanic wavelength division multiplexed systems,” in *Tech. Dig. Optical Fiber Commun. Conf*0. (OFC’1999), paper WE6, 1999.
34. Y. Fukada, “Probability density function of polarization dependent loss (PDL) in optical transmission system composed of passive devices and connecting fibers,” *IEEE J. Lightwave Technol*., vol. 20, pp. 953–964, 2002.
35. R. Holzlohner, C. R. Menyuk, W. L. Kath, and V. S. Grigoryan, “Efficient and accurate computation of eye diagrams and bit-error rates in a single-channel CRZ system,” *IEEE Photon. Technol. Lett.*, vol. 14, pp. 1079–1081, 2002.

36. N. Bergano, F. W. Kerfoot, and C. R. Davidson, “Margin measurements in optical amplifier systems,” *IEEE Photon. Technol. Lett*., vol. 5, pp. 304 – 306, 1993.

37. Yu Sun, I. T. Lima, H. Jiao, J. Wen, H. Xu, H. Ereifej, G. M. Carter, and C. R. Menyuk, “Study of system performance in a 107-km dispersion-managed recirculating loop due to polarization effects,” *IEEE Photon. Technol. Lett*., vol. 13, pp. 966–968, 2001.

38. Yu Sun, A. Lima, I. Lima, L. Yan, J. Zweck, C. R. Menyuk, and G. M. Carter, “Accurate *Q*-factor distributions in optical transmission systems with polarization effects,” in *Tech. Dig. Optical Commun. Conf.* (OFC’03), paper ThJ4, 2003.

39. N. Ramanujam, A. B. Puc, C. Lenner, H. D. Kidorf, C. R. Davidson, I. Hayee, J.-X. Cai, M. Nissov, A. Polipetskki, C. Rivers, and N. S. Bergano, “Forward error correction (FEC) techniques in long-haul optical transmission systems,” in *Proceeding LEOS 2000*, paper WB1, 2000.

40. J. –X, Cai, M. Nissov, A. N. Pilipetskii, A. J. Lucero, C. R. Davidson, D. Foursa, H. Kidorf, M. A. Mills, R. Menges, P. C. Corbett, D. Sutton, and N. S. Bergano, “2.4 Tb/s (120 × 20 Gb/s) transmission over transoceanic distance using optimum FEC overhead and 48% spectral efficiency,” in *Tech. Dig. Optical Commun. Conf.* (OFC’01), paper PD20, 2001.

41. M. Born and E. Wolf, *Principle of Optics*, Cambridge: Cambridge University Press., 7th edition, 1999.

42. G. C. Agrawal, Fiber-optic Communication Systems, New York: Jone Wiley & Sons, 3rd edition, 2002.

43. M. Yu, C. Kan, M. Lewis, and A. Sizmann, “Statistics of signal-to-noise ratio and path-accumulated power due to concatenation of polarization-dependent loss,” *IEEE Photon. Technol. Lett*., vol. 14, pp. 1418–1420, 2002.

44. T. Lima, Jr., A. O. Lima, J. Zweck, and C. R. Menyuk, “Performance characterization of chirped return-to-zero modulation format using an accurate receiver model,” *IEEE Photon. Technol. Lett.*, April, 2003.

45. C. D. Poole and D. L. Favin, “Polarization-mode dispersion measurements based on transmission spectra through a polarizer," *IEEE J. Lightwave Technol*., vol. 12, pp. 917–929, 1994.

46. J. W. Woods and H. Stark, *Probability and Random Processes with Applications to Signal Processing*, Prentice Hall, 3rd edition, 2001.

47. J. M. Jacob and G. M. Carter, “Analysis of bit-error-rate performance and pulse dynamics studies on error-free transmission of dispersion-managed solitons at 10 Gbit/s over 24500 km,” *Tech. Dig. of Optic. Fiber Commun. Conf*., OFC’98, paper ThC2, 1998.

48. G. M. Carter, R. -M. Mu, V. S. Grigoryan, C. R. Menyuk, P. Sinha, T. F. Crruthers, M. L. Dennis, and I. N. Duling, III., “Transmission of dispersion-managed solitons at 20 Gbit/s over 20000 km,” *IEE Electron. Lett*., vol. 35, pp. 233–234, 1999.

49. R. M. Craig, S. L. Gilbert, and P. D. Hale, “High-resolution, nonmechanical approach to polarization-dependent transmission measurements,” *IEEE J. Lightwave Technol*., vol. 16, pp. 1285–1294, 1998.

50. B. Marks, Yu Sun, C. R. Menyuk, and G. M. Carter, “Polarization-state evolution in recirculating loops with polarization-dependent loss,” *Opt. Lett.*, vol. 27, pp. 1881 – 1883, 2001.

51. A. H. Nayfeh, *Introduction of Perturbation Techniques*, Wiley-Interscience, 1st edition, 1993.

52. J. Cameron, L. Chen, S. Bao, and J. Stears, “Time evolution of polarization mode dispersion in optical fibers,” *IEEE Photon. Technol. Lett.*, vol. 10, pp. 1265–1267, 1998.

53. P. R. Morkel, I. A. Haxell, M. G. Taylor, and R. Keys, “Polarization effects in long-haul optically amplified lightwave systems”, in *Proc. of IEEE International Conf. On Commun.*, vol. 1, pp. 616–620, 1995.

54. Yu Sun, B. Marks, I. Lima, K. Allen, G. M. Carter, and C. R. Menyuk, “Polarization evolution in recirculating loop systems”, *Tech. Dig. Opt. Fiber Commun. Conf. (OFC 2002)*, paper ThI4, March 2002.

55. G. M. Carter and Yu Sun, “Making the *Q* distribution in a recirculating loop resemble a straight line distribution”, *Tech. Dig. Opt. Fiber Commun. Conf. (OFC 2002)*, paper ThQ5, 2002.

56. F. Heismann, “Analysis of a reset-free polarization controller for fast automatic polarization stabilization in fiber-optic transmission systems”, *IEEE J. Lightwave Technol.*, vol. 12, pp. 690–699, 1994.

57. A. Yariv, *Optical Electronics*, Holt, Rinehar and Winston, Inc., 3rd edition, 1985.

58. F. Heismann, “Compact electro-optic polarization scramblers for optically amplified lightwave systems”, *IEEE J. Lightwave Technol.*, vol. 14, pp. 1801–1814, 1996.

59. M. G. Taylor, “Improvement in Q with low frequency polarization modulation on transoceanic EDFA link,” *IEEE Photon. Technol. Lett.*, vol. 6, no. 7, pp. 860–862, 1994.

60. A. Bononi and L. A. Rusch, “Doped-fiber amplifier dynamics: a system perspective”, *IEEE J. Lightwave Technol.*, vol. 16, pp. 945–956.

61. Y. Sun, J. L. Zyskind, and A. K. Srivastava, “Average inversion level, modeling, and physics of erbium-doped fiber amplifiers,” *J. Lightwave technol.*, vol.3, pp. 991–1007 (1997).